UNIVERSTIY OF CALIFORNIA SAN DIEGO

Approaches to Phononic Wave Confinement and Guiding

A dissertation submitted in partial satisfaction of the requirements for the degree Doctor of Philosophy

in

Engineering Sciences (Mechanical Engineering)

by

Yun Zhou

Committee in charge:

Professor Prabhakar R. Bandaru, Chair
Professor Daniel F. Sievenpiper, Co-Chair
Professor Shengqiang Cai
Professor Michael Fogler
Professor James Friend

2022

The Dissertation of Yun Zhou is approved, and it is acceptable in quality and form for publication on microfilm and electronically.

University of California San Diego

2022

DEDICATION

To my parents Min Liu and Xinjian Zhou.

EPIGRAPH

Good times,

hard times,

but never bad times.

—Steve Jobs

TABLE OF CONTENTS

LIST OF FIGURES

ACKNOWLEDGEMENTS

The past four and half years in UCSD has been an incredible journey for me, throughout which I have received a great deal of support and assistance from many people.

I would first like to thank my advisors Prof. Sievenpiper and Prof. Bandaru. I feel very lucky to have had the opportunity to work with them, as they are both very supportive to me during my Ph.D. study. I appreciate Prof. Sievenpiper for always helping me focus on the big picture of my projects and sharing with me his creative ideas. He trusts his students with the projects and would always support us to work on research ideas that we love, barely setting limits to anything. I also enjoyed and am very thankful for tons of scientific and technical discussions with Prof. Bandaru. I still remember one day Prof. Bandaru came to my office with a piece of paper after reading the draft of my first paper, asking me to show him how I derived from equation A to equation B. His curiosity, patience, and persistence are huge inspirations to me. Without my advisors' guidance and kindness this dissertation would have never been possible.

I would like to thank each member of my dissertation committee: Prof. Friend, for collaboration and many helpful discussions on the SAW waveguide project, especially his suggestion on roughening the backside of the LN wafer which made a dramatic difference in the measurement; Prof. Fogler and Prof. Cai, for their valuable suggestions and their time.

I would also like to credit my collaborator Dr. Naiqing Zhang for making samples for the SAW project, Zichen Zhang for help with the SEM, and my lab mate Dr. Nirjhar Sarkar from Prof. Bandaru's group for suggestions on the electroplating. I want to express my appreciation to Prof. Sutanu Sarkar, whose lecture on finite difference methods was

very helpful to my research.

I would like to thank all my lab mates from the Applied Electromagnetics Group, who are probably the most supportive group of people I've ever been around to. I thank Dr. Aobo Li and Dr. Jiyeon Lee, for being the big brother and the big sister and providing me with career and life suggestions. I thank Dr. Dia'aaldin Bisharat, for all the research inspirations. Thank you to Kyle Thackston, for fun stories on microwaving starfish and making waveguides. To Dr. Shreya Singh, for being one of the most considerate people I know. To Matt Smith, for lending me the lifesaving 3D printer. To Sara Kandil, for always encouraging me to be more confident, and for all the late-night discussions on deep or shallow topics while we walked back home together from school every day. To Robert Davis, for his tremendous help on my projects, papers, and everything, for his enthusiasm, and for all the delightful conversations. To Xiaozhen and Erda, for being the smartest, most hardworking, and most inspiring scientific couple. And to Feng, for her company in the lab during this thesis writing. Also special thanks to past visiting students, Dr. Xianghong Kong, Dr. Zhixia Du, and Dr Zhixia Xu, for their help on my research.

I would like to thank all my friends, especially Dr. Peng Chen, Xinyue Wang, and Yangting Sun, for your support during tough times. Thank you, Jason Chen, for bringing color to my life. And the biggest thank you goes to my beloved parents, Min Liu and Xinjian Zhou, for your unconditional love and being there for me all the time. I love you too.

The material in this dissertation is based on the following papers which are either published or preparation for publication.

Chapter 2 is based on and is mostly a reprint of the following paper: Y. Zhou, P. R.

Bandaru, and D. F. Sievenpiper, *Quantum-Spin-Hall Topological Insulator in a Spring-Mass System*, New J. Phys. **20**, 123011 (2018). The dissertation author was the primary author of this material.

Chapter 3 is based on and is mostly a reprint of the following paper: Y. Zhou, P. R. Bandaru, and D. F. Sievenpiper, *Confining and channeling sound through coupled resonators*, J. Appl. Phys. **129**, 095103 (2021). The dissertation author was the primary author of this material.

Chapter 4 is based on and is mostly a reprint of the following paper: Y. Zhou, N. Zhang, D. J. Bisharat, R. J. Davis, Z. Zhang, J. Friend, P. R Bandaru and D. F Sievenpiper, *On-chip unidirectional waveguiding for surface acoustic waves along a defect line in a triangular lattice*, *Under Submission*. The dissertation author was the primary author of this material.

Chapter 5 is based on the following paper: Y. Zhou, R. Davis, L. Chen, E. Wen, P. R. Bandaru and D. F. Sievenpiper, *Helical phononic modes induced by a screw dislocation*, *In preparation*. The dissertation author was the primary author of this material.

All material is used with permission by the co-authors.

VITA

2013	B.S. in Acoustics, Nanjing University, Nanjing, China
2016	M.S. in Mechanical Engineering, University of California Irvine, Irvine, USA.
2022	Ph.D. in Engineering Science (Mechanical Engineering), University of California San Diego, La Jolla, USA

PUBLICATIONS

Y. Zhou, R. Davis, L. Chen, E. Wen, P. R. Bandaru and D. F. Sievenpiper, *Helical phononic modes induced by a screw dislocation*, *In preparation*.

Y. Zhou, N. Zhang, D. J. Bisharat, R. J. Davis, Z. Zhang, J. Friend, P. R Bandaru and D. F Sievenpiper, *On-chip unidirectional waveguiding for surface acoustic waves along a defect line in a triangular lattice*, arXiv:2111.12249 (2021).

Y. Zhou, P. R. Bandaru, and D. F. Sievenpiper, *Confining and channeling sound through coupled resonators*, J. Appl. Phys. **129**, 095103 (2021).

Y. Zhou, P. R. Bandaru, and D. F. Sievenpiper, *Quantum-spin-Hall topological insulator in a spring-mass system*, New J. Phys. **20**, 123011 (2018).

R. J. Davis, **Y. Zhou**, D. J. Bisharat, P. R. Bandaru, and D. F. Sievenpiper, *Topologically Protected Edge States in Triangular Lattices*, *In preparation*.

S. Singh, R. J Davis, D. J. Bisharat, J. Lee, S. M Kandil, E. Wen, X. Yang, **Y. Zhou**, P. R Bandaru and D. F. Sievenpiper, *Advances in Metasurfaces: Topology, Chirality, Patterning, and Time Modulation*, IEEE Antennas Propag. Mag., *Accepted*.

Y. Zhong, R. Kou, **Y. Zhou**, J. Kim, R. Chen, Y. Qiao, *Window+: Electrostatic levitation enabled Polymer-Air multilayer (EPAM) structures for highly transparent energy efficient windows*, Energy Convers. Manag. **248**, 114803 (2021).

D. J. Bisharat, R. J Davis, **Y. Zhou**, P. R. Bandaru and D. F. Sievenpiper, *Photonic Topological Insulators: A Beginner's Introduction [Electromagnetic Perspectives]*, IEEE Antennas Propag. Mag. **63**, 112 (2021).

Z. Xu, X. Kong, R. J. Davis, **Y. Zhou**, X. Yin and D. F. Sievenpiper, *Topological valley transport under long-range deformations*, Phys. Rev. Research **2**, 013209 (2020).

X. Kong, **Y. Zhou**, G. Xiao and D. F. Sievenpiper, *Spin-momentum locked modes on anti-phase boundaries in photonic crystals*, Opt. Express **28**, 2070-2078 (2020).

Yun Zhou, Ali Morshedifard, Jaeho Lee, and Mohammad Javad Abdolhosseini Qomi ,*The contribution of propagons and diffusons in heat transport through calcium-silicate-hydrates*, Appl. Phys. Lett. **110**, 043104 (2017).

ABSTRACT OF THE DISSERTATION

Approaches to Phononic Wave Confinement and Guiding

by

Yun Zhou

Doctor of Philosophy in Engineering Sciences (Mechanical Engineering)

University of California San Diego, 2022

Professor Prabhakar R. Bandaru, Chair

Professor Daniel F. Sievenpiper, Co-Chair

Guiding phononic waves with low loss is attractive from both scientific and technological points of view, where a well-confined, robust, and unidirectional phononic waveguide with little reflection is desired. However, phonons are magnetically inert, making it challenging to implement related unidirectional/chiral transport in phononic systems. Reciprocal topological waveguides are proven to be capable of guiding waves unidirectionally over defects and disorders in electronic and photonic systems. They can be constructed by tuning the lattice symmetry, which is a very intriguing approach to be extended to guide phonon propagations.

In this dissertation, unidirectional phononic waveguides from 2D to 3D systems,

that are mainly based on topological physics, are investigated theoretically and experimentally. Starting with a most fundamental 2D spring-mass theoretical model, we prove that pseudospins can be introduced to a phononic system by relative variations of the inter- and intra-unit cell spring constants. These pseudospins correspond to a pair of topologically protected counter-propagating edge states at the boundary of such a system, which are unidirectional and immune to backscattering. Next, a phononic waveguide constitutes of Helmholtz resonators is proposed to further improve the confinement and robustness of phonon propagations. We also propose a highly robust guiding principle, based on a line defect within a true triangular phononic lattice. Such waveguiding mechanism is experimentally demonstrated for surface acoustic waves (SAWs), that overcomes obstacles involving beam steering and lateral diffraction. Lastly, we extend the idea of creating a defect-line waveguide from 2D to 3D, and develop a helical waveguide with a screw dislocation in a hexagonal close packed (hcp) phononic crystal. Our simulations and measurements prove the directionality of the helical modes confined at the screw dislocation.

Chapter 1

Introduction

1.1 Topological Insulator

Topology is a mathematical concept that characterize the properties of a geometric object that are unaffected by any continuous deformations. Topological insulator found its origin in the 1980s, when physicists tried to use topology to explain the quantum Hall effect [1,2]. They showed that electrons in such systems acquire a special phase (called a geometric or Berry phase, described in subsection 1.2.1.) as their wavevector changes, and that the properties of the system do not change for a wide range of perturbations to the material, such as deformations or defects, if the topology of the system doesn't change. These physicists were awarded the Nobel Prize in Physics in 2016 due to their interesting discoveries. Their success has inspired the research with topological materials, which could be used in future quantum computers or in new generations of electronics and superconductors.

The "topological" properties of topological insulators come from the geometry of their energy band structures, which can usually be characterized by topological invariants (see subsection 1.2.2). As suggested by its name, topological insulators behave as an insulating material in its interior. What makes them different from conventional insulators is that when two materials with different topologies are placed next to each other, interesting effect happens at the boundary between these materials. Electron transport can

be seen at the boundary, commonly called edge states [3,4]. Since this transport is enabled by the change in the topology at the interface of two materials, and that topology does not alter for a wide class of changes to the material, the edge state is considered "protected". Even more remarkable is that electrons moving along these edge states must do so in one direction only, with no possibility of scattering back in the other direction. Therefore, unidirectional waveguides can be built based on topological insulators.

The existence of the topological edge states is a consequence of the wave nature of the electrons, not specifically their quantum interactions. As a result, it is possible to construct classical wave systems [5–9] with analogous properties to their electronic counterparts. This opened the door to a vast range of theoretical proposals and experimental demonstrations. Replacing the electron with a phonon, we arrive at phononic topological insulators [10], which demonstrate many of the same features of electronic topological insulator.

To emulate the quantum Hall effect, gyroscopic phononic crystals [11,12], where each lattice site is coupled with a spinning gyroscope, have been adopted to break the time reversal symmetry in the system. Another type of phononic topological insulators is based on breaking the lattice symmetry of phononic crystals, where the time reversal symmetry is preserved. For example, by shrinking or expanding the unit cell of a honeycomb lattice while retaining its C_6 symmetry [13,14], or by breaking the *z*-directional mirror symmetry in bianisotropic materials [15], pseudospins may be introduced to a phononic crystal, where opposite pseudospins propagate in opposite directions at an interface, an analogy to the quantum spin Hall effect. Valley-selective topological edge states can also be found in a honeycomb phononic crystal with broken inversion symmetry, an analogy to the quantum

valley Hall effect [16–20]. Recently, defect line based topological waveguides have been discovered [21,22], an example of which is discussed in Chapter 4. They cannot be categorized into spin or valley type of topological insulators as they are not with the same topology. Nevertheless, they still exhibit unidirectional waveguiding with backscattering immunity. Topological defects [23] have also been used in 3D phononic crystals to build unidirectional waveguide [24–26]. A unidirectional topological waveguide can be created by introducing a screw dislocation in a 3D phononic topological insulator, or in a stack of 2D phononic topological insulators.

1.2 Characterization of Topological Phases

1.2.1 Berry Phase, Berry Connection and Berry Curvature

As briefly mentioned in the previous section, topologies for material systems are defined by the geometry of their energy bands. The idea of geometric phase is adopted to characterize the geometry of energy bands. The geometric phase usually carries information about the topology of a material. The geometric phase was first proposed in 1956 by Pancharatnam [27] for the propagation of light through a sequence of polarizers and was later generalized by Berry for quantum mechanics [28,29]. The geometric phase is a universal concept that emerges in the adiabatic cyclic evolution of any state in a system. It can emerge due to the gradual variation (i.e. adiabatic process) of a state in other types of parameter spaces, including the momentum space of a periodic system, or known as the Brillouin zone. In such a system, the change in wavevector $\boldsymbol{k}$ (Bloch momentum) causes the change in the state. For any path that remains on the same band and does not intersect with any other band, k varies in closed loops due to the lattice periodicity, where

$-\pi = +\pi$, and a geometric phase is picked up. This geometric phase usually carries information about the topology of a material.

Let's consider a periodic lattice described by a general eigenvalue problem in the momentum space:

$$H(\boldsymbol{k})\psi_n(\boldsymbol{k}) = \lambda_n(\boldsymbol{k})\psi_n(\boldsymbol{k}). \tag{1.1}$$

where $\psi_n(\boldsymbol{k})$ is an eigenstate of $H(\boldsymbol{k})$ at each $\boldsymbol{k}$ for the nth band. We are interested in the evolution of the system as $\boldsymbol{k}$ is varied very slowly along the band in the BZ, as defined by a geometric phase, commonly referred to as Berry phase:

$$\phi_n = \oint_n \, d\boldsymbol{k} \cdot \boldsymbol{A}_n(\boldsymbol{k}), \tag{1.2}$$

Here, $\boldsymbol{A}_n(\boldsymbol{k})$ is the Berry connection, or Berry vector potential, which is defined as

$$\boldsymbol{A}_n(\boldsymbol{k}) = i\left\langle \psi_n(\boldsymbol{k}) \middle| \frac{\partial}{\partial \boldsymbol{R}} \middle| \psi_n(\boldsymbol{k}) \right\rangle. \tag{1.3}$$

For a given band, the eigenvector $\psi_n(\boldsymbol{k})$ under the transformation $\psi_n(\boldsymbol{k}) \rightarrow e^{i\zeta(\boldsymbol{k})}\psi_n(\boldsymbol{k})$, where $\zeta(\boldsymbol{k})$ is a smooth, single-valued function with $\zeta(\boldsymbol{k}_{\text{end}}) = \zeta\left(\boldsymbol{k}_{\text{begin}}\right) + 2m\pi$, is still an eigenvector to $H(\boldsymbol{k})$. The Berry connection is not invariant and it transforms as $\boldsymbol{A}_n(\boldsymbol{k}) \rightarrow \boldsymbol{A}_n(\boldsymbol{k}) - \frac{\partial}{\partial \boldsymbol{R}}\zeta(\boldsymbol{k})$. The Berry phase, on the other hand, is invariant modulo 2π:

$$\oint_n \, d\boldsymbol{k} \cdot \boldsymbol{A}_n(\boldsymbol{k}) \rightarrow \oint_n \, d\boldsymbol{k} \cdot \boldsymbol{A}_n(\boldsymbol{k}) - \oint_n \, \frac{\partial}{\partial \boldsymbol{R}}\zeta(\boldsymbol{k})\, d\boldsymbol{k} \rightarrow \oint_n \, d\boldsymbol{k} \cdot \boldsymbol{A}_n(\boldsymbol{k}) - 2m\pi.$$

Berry curvature, a term that is invariant under such transformation, can be constructed by taking the curl the Berry connection:

$$\Omega_n(\boldsymbol{R}) = \nabla_R \times \boldsymbol{A}_n(\boldsymbol{R}). \tag{1.4}$$

We can think of the Berry curvature as a magnetic field in momentum space (the curl of the Berry vector potential).

The Berry phase can be rewritten as the integral of the Berry curvature over the BZ using Stokes' theorem:

$$\phi_n = \int_{BZ} d^2\boldsymbol{k} \cdot \boldsymbol{\Omega}_n(\boldsymbol{k}). \tag{1.5}$$

1.2.2 Chern Number

Topological invariants are defined to characterize the topology of a material [30]. For a topological insulator with broken time reversal symmetry, usually a non-zero Chern number can be obtained for the system. The Chern number of the nth band of a 2D lattice is simply the Berry phase over the full Brillouin zone,

$$C_n = \frac{1}{2\pi}\int_{BZ} d^2\boldsymbol{k} \cdot \Omega_n(k_x, k_y), \tag{1.6}$$

where in 2D the Berry curvature only has two terms.

$$\Omega_n(k_x, k_y) = \frac{\partial A^n_{k_y}}{\partial k_x} - \frac{\partial A^n_{k_x}}{\partial k_y}, \tag{1.7}$$

where A^n is the Berry connection for the nth mode.

$$A^n_{k_x} = i\int d^2\boldsymbol{r} \sum_{i,j} E^*_{n,\boldsymbol{k},i}(\boldsymbol{r})\epsilon_{i,j}(\boldsymbol{r}) \cdot \frac{\partial E_{n,\boldsymbol{k},j}(r)}{\partial k_x}, \tag{1.8}$$

$$A^n_{k_y} = i\int d^2\boldsymbol{r} \sum_{i,j} E^*_{n,\boldsymbol{k},i}(\boldsymbol{r})\epsilon_{i,j}(\boldsymbol{r}) \cdot \frac{\partial E_{n,\boldsymbol{k},j}(r)}{\partial k_y}. \tag{1.9}$$

Here, the eigen wavefunction $E_{n,\boldsymbol{k},j}$ is normalized so that

$$\int d^2\boldsymbol{r} \sum_{i,j} E^*_{n,\boldsymbol{k},i}(\boldsymbol{r})\epsilon_{i,j}(\boldsymbol{r})E_{n,\boldsymbol{k},j}(r) = 1.$$

Chern number always takes an integer value. When the Chern number is not zero, the 2D system is said to topologically nontrivial. The definition of the Chern number can be extended to 3D in a similar manner.

For spin or valley type of topological insulators, on the other hand, the Chern number defined here is always zero, as there is no time-reversal symmetry breaking in such systems. In these cases, spin or valley Chern number is defined. The spin Chern number is defined by replacing the eigen wavefunctions in Eq. 1.6. with those associated with a given spin. The valley Chern number is defined by doing the integral in Eq. 1.6 only in half of the Brilloin zone corresponding to K or K′. These will be discussed in detail in Chapter 2 and Chapter 4.

1.2.3 Symmetry Indicator

There are some topological phenomena, such as topological Kagome lattices [31–33] and topological defect-line waveguide in a triangular lattice, that cannot be categorized properly by the Chern number, or spin or valley Chern numbers. Such behavior can be further understood by the application of symmetry indicators [34]. Symmetry indicators provide a means of analyzing the topological behavior of periodic systems given the relevant rotational symmetry of the base unit cell. For a system with unit cell possessing C_n rotational symmetry the symmetry indicator is defined by the set of numbers $\chi^{(n)}$ that count the number of rotation eigenvalues the system has at high symmetry points, minus those at the Γ point. The details are discussed in Chapter 4.

1.3 Scope of this Thesis

In this work we will attempt to apply the topological physics we discussed in this chapter to construct unidirectional and confined phononic waveguides. Our goal is to

understand the fundamental physics behind the phononic topological insulator, as well as to look for easy implementations and usage for phononic topological waveguides.

Chapter 2 presents a theoretical study on introducing spin degree of freedom to a most fundamental 2D phononic system – a spring-mass system. We start from a honeycomb lattice with a Dirac degeneracy and apply zone folding technique to form a double Dirac cone, which introduce extra degree of freedoms so that phonons at the same energy level can be hybridized to form pseudospins. Contrasting the inter- and intra- cell coupling breaks the lattice symmetry while still maintains the C_6 symmetry of the unit cells, and lifts a bandgap within which topological edges modes may appear. Band inversion could happen in such a system when gradually variating the couplings, and the topology of the system is demonstrated by the spin Chern number and the Z_2 invariant. Unidirectional phononic modes correspond to the pseudospin-up and pseudospin-down are found at the interface topological trivial and non-trivial spring-mass domains. Our time-domain simulations reveal that these modes are robust over a range of disorders and sharp turns.

Chapter 3 proposes the usage of Helmholtz resonators to improve the robustness of phononic waveguides. Since the robustness of reciprocal phononic topological insulators, like the one discussed in Chapter 2, are protected by their lattice symmetry, some lattice disorders may damage the topological edge modes. We demonstrate that modes supported by the Helmholtz resonator waveguide are well-confined to the waveguide, and are robust over frequency and location disorders. The result from simulations suggests the possibility of using such mechanism to confine phononic energy to a closed phononic circuit, or even to a small point.

Chapter 4 investigates a defect-line waveguide in a true triangular phononic lattice for surface acoustic waves. Contrast to spin or valley type of topological insulators mentioned above in this chapter, this defect-line waveguide has varnishing Berry curvature while still support unidirectional modes, as evidenced by simulations. The topology of such waveguide is characterized by the symmetry indicator. A on-chip surface acoustic waveguide is built and measured, which proves the waveguide can guide surface acoustic wave over sharp turns with little lateral diffraction and reflection.

Chapter 5 is an extension of Chapter 4 to a 3D structure. Similar to the idea of creating a defect line, we introduce a defect line to a 3D phononic crystal – a screw dislocation. Simulations show that a pair of counter-propagating modes at the dislocation position appear in the band gap of the 3D crystal. These modes are unidirectional, as their propagation direction is locked to the helicity of the screw dislocation. Samples with and without the screw dislocation are measured, and experimental data agrees with simulation results.

Finally, chapter five concludes with a summary of the thesis along with a brief note on possible future applications and interesting developments in the field of phononic topological insulators.

Chapter 2

Pseudospins in a Spring-mass System

2.1 Introduction

Inspired by the discovery of topological phases and edge states in electronic materials [35,36], the possibility of building related devices for the control of the propagation of light [5,37–42] and sound [12,15,43–49] is being extensively studied. The related device building blocks may harness three major types of topological phases analogous to those in condensed matter systems: quantum Hall effect (QHE) [1,2], quantum spin Hall effect (QSHE) [50–52], and quantum valley Hall effect (QVHE) [18,53–55]. The QHE has chiral edge modes, and requires an external magnetic field to break time reversal symmetry (TRS), which may be accomplished in acoustic and photonic systems by adding gyroscopic material or external circulators [11,12,37,43,44]. The QSHE is amenable to TRS, associated with a pair of spin-locked helical modes, and is obtained by introducing strong spin-orbit coupling [15,39,41,45,49]. The QVHE generates valley-locked chiral edge states, and exploits the valley degrees of freedom [16,40].

It would of much advantage and yield insight, to consider a harmonic oscillator point of view, quite common in physics, for invoking topological phases. In this respect, a discrete spring-mass based mechanical system, may constitute a model system for topological structure as related to phononic materials. For instance, QHE based topological insulators in spring-mass lattices may be created by adding circulating gyroscopes [11,12],

Coriolis force [56] or varying spring tension [57]. QVHE has been realized in such systems by alternating the mass at A and B sites of the unit cell of a mechanical graphene-like lattice [16]: **Fig. 2.2(a)**. QSHE-like phenomena has also been explored in spring-mass lattices, through coupled pendula [58], and a mechanical granular graphene system [59]. However, many of these systems are difficult to implement in practical applications.

In this chapter, we propose a two-dimensional (2-D) spring-mass system, exemplifying a QSHE topological insulator, in the acoustic domain. Various trivial and non-trivial band structures may be originated by varying the masses (m) and the relative spring constants (k) in the associated lattice. In addition to exhibiting the topological features that have now become familiar to practitioners in the field, we indicate a novel spin degree of freedom. The related pseudospins are observed, in frequency domain analysis as the polarization of modal displacement field of masses in one unit cell: **Fig. 2.2(a)**. TRS protected edge modes, incorporating the propagation of such pseudospins, are shown to exist. This structure may be representative of different phases of matter, as the the spring constant can be view as coupling strength between unit cells in various systems. It can be applied as one of the possible practical designs of photonic/phononic topological insulators.

A basis for creating a topological material, based on a spring-mass system, to mimic the QSH effect, is to create intrinsic TRS. We consider a hexagonal lattice of masses and springs arranged in C_6 symmetry. The E and E′ representations are each two-fold degenerate with the individuals being complex conjugates [34]. Consequently, a four-fold degeneracy is required to satisfy TRS and may be enabled through manifesting a double

Dirac cone in the band structure. We achieve a four-fold degeneracy, in the band structure of a spring-mass constituted lattice by the zone-folding method [8].

2.2 The Spring-mass Model and Computational Methods

We consider a hexagonal lattice with equal masses m connected by linear springs k, as shown in **Fig. 2.1**. The unit cell of this hexagonal lattice consists of 2 masses $m^1 = m^2 = m$, with lattice constants $\overrightarrow{a_1}$ and $\overrightarrow{a_2}$ ($|\overrightarrow{a_1}| = |\overrightarrow{a_2}| = a$). From Newton's law, the governing equation Mü = F(u), where M is a diagonal matrix with the values of the two masses on its diagonal: $M = \text{diag}\{m^1, m^1, m^2, m^2\}$. u is a vector constituted from the two degrees of freedom for each mass – the x and y direction displacements for m^1 and m^2: $u = \{u_x^1, u_y^1, u_x^2, u_y^2\}$ and F is the force. We consider a Bloch wave solution of the type $u = Ue^{i(qa_1\gamma_1 + la_2\gamma_2 - \omega t)}$ to the governing equation of the $(q,l)^{\text{th}}$ unit cell, where $U = \{U_x^1, U_y^1, U_x^2, U_y^2\}$ is the modal displacement, and $\gamma_1$and γ_2 are wave vectors. A dispersion relation is obtained by solving the eigenvalue problem $D(\gamma_1, \gamma_2)U = \omega^2 MU$, with D as a dynamical matrix.

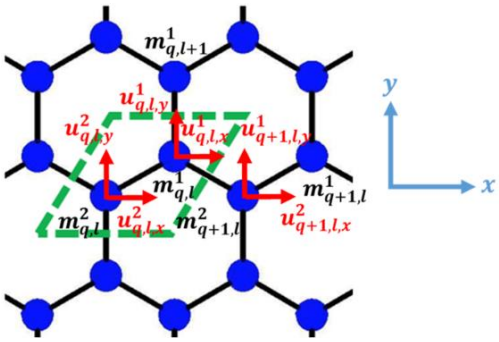

Figure 2.1 Hexagonal spring-mass lattice. The spring constant $\boldsymbol{k}$ and mass m here are uniform throughout the lattice. Unit cell $(\boldsymbol{q}, \boldsymbol{l})$ consist of two masses $\boldsymbol{m^1_{q,l}}$ and $\boldsymbol{m^2_{q,l}}$.

To get the dispersion relations, we evaluate

$$Du = \omega^2 u, \tag{2.1}$$

where *D* is the dynamical matrix, and u is the displacements of the masses.

For a two-mass unit cell shown in **Fig. 2.1** D is derived to be of form

$$D(\gamma_1, \gamma_2) = -\begin{bmatrix} -\frac{3}{2}k & 0 & \frac{3}{4}\left(1+e^{i\gamma_1}\right)k & \frac{\sqrt{3}}{4}\left(1-e^{i\gamma_1}\right)k \\ 0 & -\frac{3}{2}k & \frac{\sqrt{3}}{4}\left(1-e^{i\gamma_1}\right)k & \left(\frac{1}{4}+\frac{1}{4}e^{i\gamma_1}+e^{i\gamma_2}\right)k \\ \frac{3}{4}\left(1+e^{-i\gamma_1}\right)k & \frac{\sqrt{3}}{4}\left(1-e^{-i\gamma_1}\right)k & -\frac{3}{2}k & 0 \\ \frac{\sqrt{3}}{4}\left(1-e^{-i\gamma_1}\right)k & \left(\frac{1}{4}+\frac{1}{4}e^{-i\gamma_1}+e^{-i\gamma_2}\right)k & 0 & -\frac{3}{2}k \end{bmatrix}. \tag{2.2}$$

The elements of *D* were obtained through assuming a Bloch wave solution of form $u_{q,l} = Ue^{i(qa_1\gamma_1 + la_2\gamma_2 - \omega t)}$. Here $U = \left\{U_x^1, U_y^1, U_x^2, U_y^2\right\}$ is the modal displacement vector, and $\gamma_1$and γ_2 are Bloch wave vectors. Take the mass $m_{q,l}^1$ in unit cell (q, l) for example. The force balance for $m_{q,l}^1$ in x direction can be written as,

$$m_{q,l}^1 \ddot{u}_{q,l,x}^1 = k\left[\left(u_{q+1,l,x}^2 - u_{q,l,x}^1\right) cos\frac{\pi}{6} cos\frac{\pi}{6} + \left(u_{q,l,y}^1 - u_{q,l+1,y}^2\right) sin\frac{\pi}{6} cos\frac{\pi}{6} + \left(u_{q,l,x}^2 - u_{q,l,x}^1\right) cos\frac{\pi}{6} cos\frac{\pi}{6} + \left(u_{q,l,y}^2 - u_{q,l,y}^1\right) sin\frac{\pi}{6} cos\frac{\pi}{6}\right]. \tag{2.3}$$

Substitute the Bloch solution into Eq. (2.3) we get,

$$-\omega^2 m_{q,l}^1 U_x^1 = -\frac{3}{2}kU_x^1 + 0U_y^1 + \frac{3}{4}\left(1+e^{i\gamma_1}\right)kU_x^2 + \frac{\sqrt{3}}{4}\left(1-e^{i\gamma_1}\right)kU_y^2, \tag{2.4}$$

which are elements of the first raw of Eq. (2.2). Other entries of D can be obtained in a similar manner.

The band structure of the hexagonal lattice in **Fig. 2.2(c)** exhibits a single Dirac cone at the K (K′) point. The frequencies are non-dimensionalized as $\Omega = \frac{\omega}{\sqrt{\frac{k}{m}}}$. Subsequently, we fold the first Brillouin zone (BZ) of the hexagonal lattice, twice, to form

a new BZ with 1/3 of its original area, as shown in **Fig. 2.2(b)**. Consequently, the K (K′) point is mapped to the Γ point at the center of the BZ, creating a double Dirac cone. The smaller BZ corresponds to an expanded unit cell in real space of 3 times of the original unit cell area, with $3\times 2 = 6$ masses, and lattice constant $\overrightarrow{b_1}$ and $\overrightarrow{b_2}$ ($|\overrightarrow{b_1}| = |\overrightarrow{b_2}| = \sqrt{3}a = b$), as indicated in **Fig. 2.2(a)**. The band structure based on the expanded unit cell is plotted in **Fig. 2.2(d)**, and indicates a double Dirac cone at Γ.

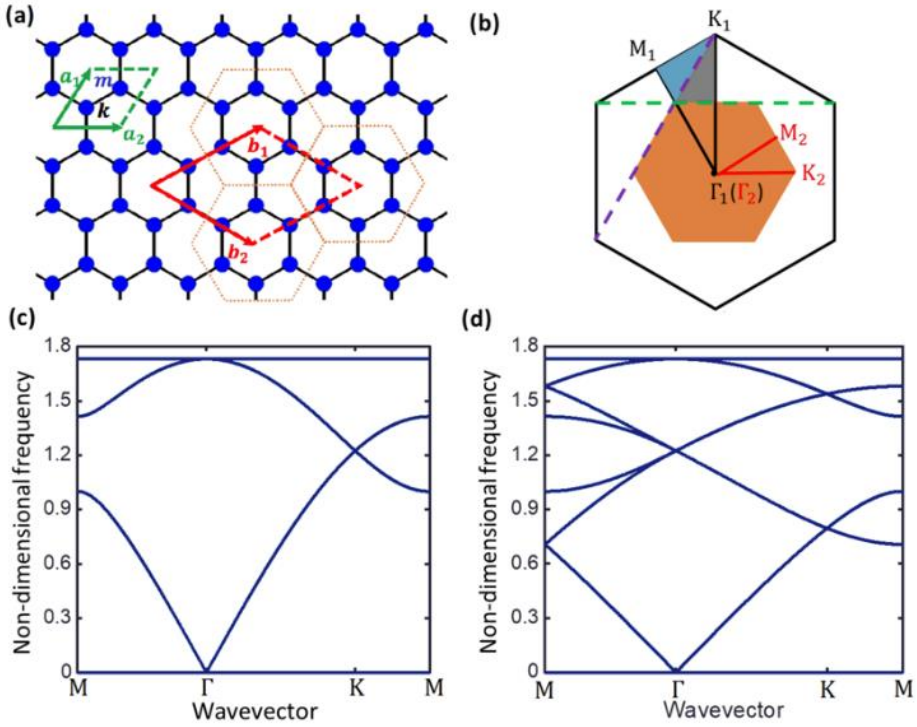

Figure 2.2 Zone folding and double Dirac degeneracy. (a) Hexagonal spring-mass lattice with uniform spring constant k and mass m. a_1 and a_2 are lattice constants of the unit cell before zone folding, and b_1 and b_2 are lattice constants of the unit cell after zone folding. **(b)** First Brillouin zone (BZ) before (big hexagon) and after (small hexagon in orange) zone folding. When looking at 1/12 BZ, the triangle $\Gamma_1 M_1 K_1$ is first folded along the purple dashed line, then folded along the green dashed line. **(c)** Band diagram of the lattice in (a) for unit cell of 2 masses, and **(d)** band diagram of the lattice in (a) for the expanded unit cell of 6 masses.

To induce a phase transition, in the topological sense, we break the spatial symmetry of the hexagonal lattice, through changing the spring constants of the connecting masses in the lattice, i.e., distinguishing the intra unit cell spring constant k_1 from the inter

unit-cell spring constant: k_2. Such distinction still preserves the C_6 symmetry of the unit cell. It was found that when $k_1 \neq k_2$, the band degeneracy at the Γ point is lifted and yields a band gap, as indicated in **Fig. 2.3(b)** and **(c)**. With k_2 and m constant, we continuously change the value of k_1 from $k_1 > k_2$ to $k_1 < k_2$, through which the band gap at Γ point first closes and then reopens. When $k_1 = k_2$, there is no band gap [**Fig. 2.3(a)(b)** and **(c)**]. We study the modes related to this transition for (i) $k_1 > k_2$ and (ii) $k_1 < k_2$.

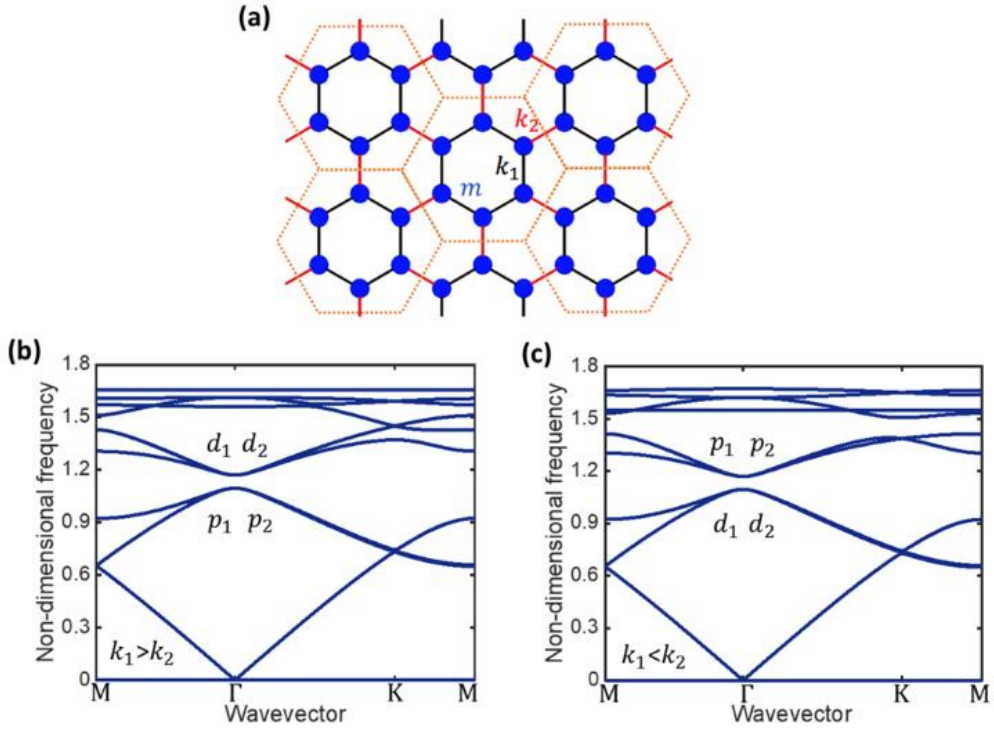

Figure 2.3 Band gap induced by symmetry breaking. (a) Hexagonal spring-mass lattice with intra-cell spring k_1 (black straight rods) different from inter-cell spring k_2 (red straight rods). **(b)** Band diagram of hexagonal lattice with $k_1 > k_2$. Modal displacements at Γ are of p symmetry for the lower degeneracy, and of d symmetry for the higher degeneracy. **(c)** Band diagram of hexagonal lattice with $k_1 < k_2$. Modal displacements at Γ are of d symmetry for the lower degeneracy, and of p symmetry for the higher degeneracy.

2.3 Results and Discussions

2.3.1 Modal Displacement Fields in Hexagonal Spring-mass Lattices: The Case for Pseudospins

The modal displacement and its x and y components, of the masses in the unit cell, at the Γ point of the $k_1 > k_2$ lattice are shown in **Fig. 2.4(a) – (d)**. The labeling of the modes in **Fig. 2.4(a) – (d)** follows the nomenclature for the lower to higher band degeneracy corresponding to **Fig. 2.3(b)**. The modal displacements for a given mass in $p_1 (/d_1)$ are orthogonal to $p_2 (/d_2)$, respectively. The constituent x and y direction displacements are plotted successively below. Since each mass has two degrees of freedom – the displacements in the *x*- and the *y*-directions, in considering the parities of modal displacements in Fig. 3, we consider the x- and the y-direction modal displacement fields separately. We find that the *x/y* direction displacements fields at Γ are of odd and even spatial parities – of the p_x $(/p_y)$ and $d_{x^2-y^2}$ $(/d_{xy})$ variety, as inferred both from the sense of the symmetry of the displacements and stated relationships in the C_6 character table [60]. For instance, the p_x $(/p_y)$ character is antisymmetric with respect to the center, even symmetric to the x- $(/y$-$)$ axis, and odd symmetric to the y- $(/x$-$)$ axis, while the $d_{x^2-y^2}$ $(/d_{xy})$ parity is symmetric with repsect to the center, and even(/odd) symmetric to both the x and y axes.

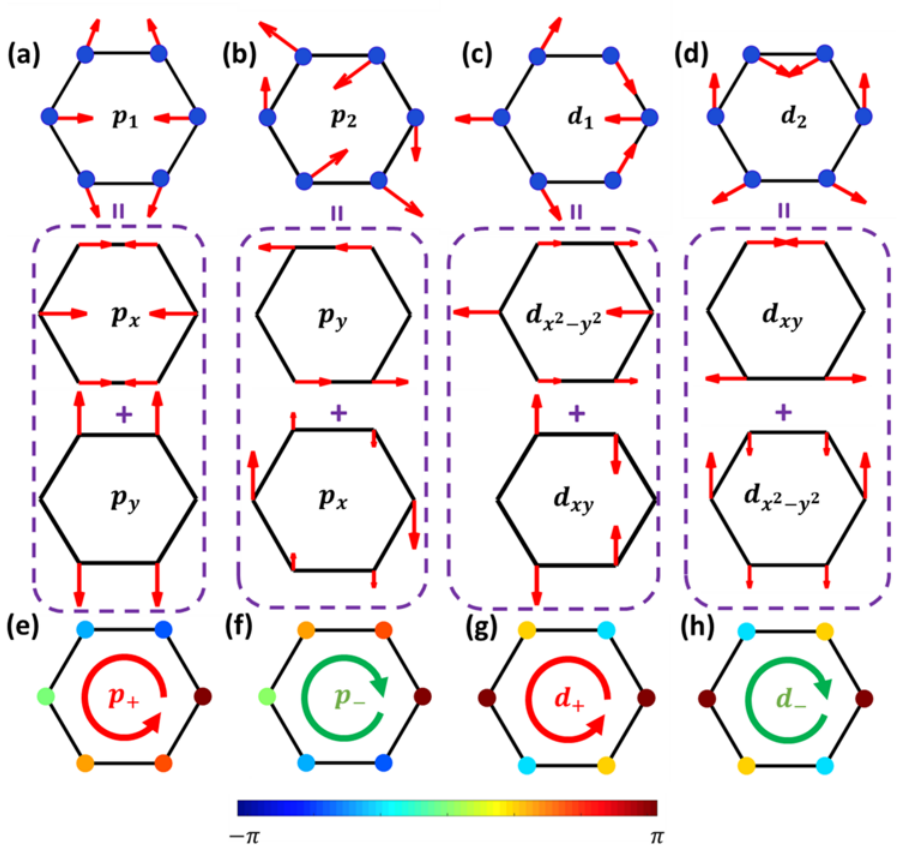

Figure 2.4 Pseudospins. (a) p_1, **(b)** p_2 and **(c)** d_1, **(d)** d_2 are total modal displacements for the two two-fold degeneracies at Γ point when $k_1 \neq k_2$. p_1 and p_2 have odd parities, while d_1 and d_2 have even parities. x and y direction components to **(a)** and **(b)** clearly show p_x/p_y symmetry, while those to **(c)** and **(d)** that have $d_{x^2-y^2}/d_{xy}$ symmetry. **(e)**, **(f)**, **(g)** and **(h)** are plots of phase relationships between the 6 masses in one unit cell for p_+, p_-, d_+ and d_- in color map, indicating the polarization of wave propagation associated with pseudospin up and pseudospin down.

Hybridizing the p_1/d_1 and p_2/d_2 modes in a symmetric and antisymmetric manner yields pseudospins [8],

$$p_\pm = (p_1 \pm ip_2)/\sqrt{2}\text{ , and } d_\pm = (d_1 \pm id_2)/\sqrt{2}. \tag{2.5}$$

Fig. 2.4(e) – (h) illustrates the related phase distribution of p_+, p_-, d_+ and d_- in the range of $-\pi$ to π. Clearly seen from the phase relationship that harmonic wave propagation in p_+/d_+ and p_-/d_- have opposite polarizations. Taking the time harmonic component $e^{i\omega t}$ into consideration, due to the orthogonality of displacements in p_1/d_1 and p_2/d_2, each mass

corresponding to the hybridized mode p_+/d_+ rotates in the one direction, while each mass in p_-/d_- rotates in the opposite direction. The incorporation of the relative motions of the six masses in the unit cell leads to rotation of the whole displacement field. Such rotation may be considered as one manifestation of a pseudo-spin. One can follow the motion in d_+ during one time period T: **Fig. 2.5**, indicating such clockwise orientability of the displacement field.

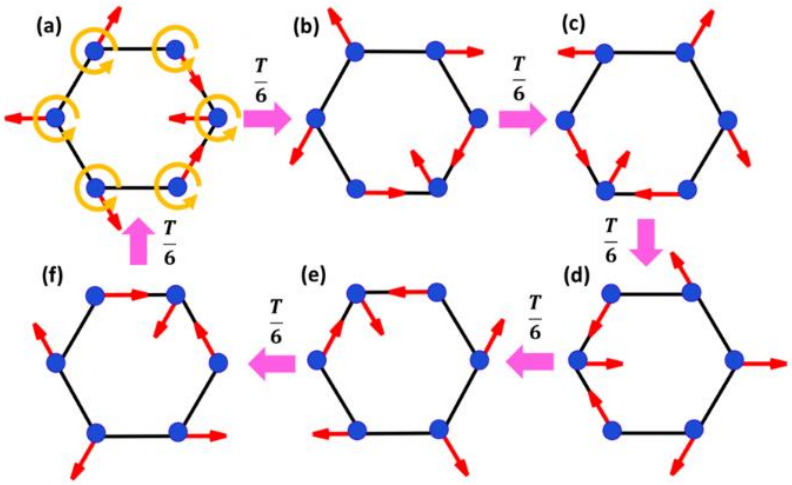

Figure 2.5 Rotation of the displacement field. The spinning of modal displacement field for $d_+ = (d_1 + id_2)/\sqrt{2}$ as a result of time domain motion of the masses during one period T.

We find that for the case of $k_1 < k_2$, the modal displacement fields have exactly the same odd and even spatial parities, but d_1 and d_2 are now associated with the higher two degenerate bands, while p_1 and p_2 corresponds to the lower two bands (**Fig. 2.3 (c)**). This demonstrates that band inversion happens at the Γ point during the process of closing and reopening the band gap, and a change in topology of the band structure. Such a change has

been previously quantified through the spin Chern number [35], which will be studied in detail in the following section.

2.3.2 Effective Hamiltonian, Berry Curvature, Spin Chern Number, and Z_2 Invariant

The dynamical matrix D for 6 masses with 12 constituent modal displacements (i.e., $U = \left[U_x^1, U_y^1, U_x^2, U_y^2, U_x^3, U_y^3, U_x^4, U_y^4, U_x^5, U_y^5, U_x^6, U_y^6\right]^T$) is of the form:

$D=$

$$\begin{bmatrix}
\frac{3}{2}\frac{k_2}{m} & 0 & -\frac{3}{4}\frac{k_1}{m} & \frac{\sqrt{3}}{4}\frac{k_1}{m} & 0 & 0 & 0 & 0 & 0 & 0 & -\frac{3}{4}\frac{k_1}{m} & -\frac{\sqrt{3}}{4}\frac{k_1}{m} \\
0 & \frac{k_2}{m}+\frac{1}{2}\frac{k_1}{m} & \frac{\sqrt{3}}{4}\frac{k_1}{m} & -\frac{1}{4}\frac{k_1}{m} & 0 & 0 & 0 & -\frac{k_2}{m}e^{iy_2} & 0 & 0 & -\frac{\sqrt{3}}{4}\frac{k_1}{m} & -\frac{1}{4}\frac{k_1}{m} \\
-\frac{3}{4}\frac{k_1}{m} & \frac{\sqrt{3}}{4}\frac{k_1}{m} & \frac{3}{4}\frac{k_1}{m}+\frac{3}{4}\frac{k_2}{m} & -\frac{\sqrt{3}}{4}\left(\frac{k_1}{m}-\frac{k_2}{m}\right) & 0 & 0 & 0 & 0 & -\frac{3}{4}\frac{k_2}{m}e^{iy_1} & -\frac{\sqrt{3}}{4}\frac{k_2}{m}e^{iy_1} & 0 & 0 \\
\frac{\sqrt{3}}{4}\frac{k_1}{m} & -\frac{1}{4}\frac{k_1}{m} & -\frac{\sqrt{3}}{4}\left(\frac{k_1}{m}-\frac{k_2}{m}\right) & \frac{1}{4}\frac{k_2}{m}+\frac{5}{4}\frac{k_1}{m} & 0 & -\frac{k_1}{m} & 0 & 0 & -\frac{\sqrt{3}}{4}\frac{k_2}{m}e^{iy_1} & -\frac{1}{4}\frac{k_2}{m}e^{iy_1} & 0 & 0 \\
0 & 0 & 0 & 0 & \frac{3}{4}\frac{k_1}{m}+\frac{3}{4}\frac{k_2}{m} & \frac{\sqrt{3}}{4}\left(\frac{k_1}{m}-\frac{k_2}{m}\right) & -\frac{3}{4}\frac{k_1}{m} & -\frac{\sqrt{3}}{4}\frac{k_1}{m} & 0 & 0 & -\frac{3}{4}\frac{k_2}{m}e^{iy_1-iy_2} & \frac{\sqrt{3}}{4}\frac{k_2}{m}e^{iy_1-iy_2} \\
0 & 0 & 0 & -\frac{k_1}{m} & \frac{\sqrt{3}}{4}\left(\frac{k_1}{m}-\frac{k_2}{m}\right) & \frac{1}{4}\frac{k_2}{m}+\frac{5}{4}\frac{k_1}{m} & -\frac{\sqrt{3}}{4}\frac{k_1}{m} & -\frac{1}{4}\frac{k_1}{m} & 0 & 0 & \frac{\sqrt{3}}{4}\frac{k_2}{m}e^{iy_1-iy_2} & -\frac{1}{4}\frac{k_2}{m}e^{iy_1-iy_2} \\
0 & 0 & 0 & 0 & -\frac{3}{4}\frac{k_1}{m} & -\frac{\sqrt{3}}{4}\frac{k_1}{m} & \frac{3}{2}\frac{k_2}{m} & 0 & -\frac{3}{4}\frac{k_1}{m} & \frac{\sqrt{3}}{4}\frac{k_1}{m} & 0 & 0 \\
0 & -\frac{k_2}{m}e^{-iy_2} & 0 & 0 & -\frac{\sqrt{3}}{4}\frac{k_1}{m} & -\frac{1}{4}\frac{k_1}{m} & 0 & \frac{k_2}{m}+\frac{1}{2}\frac{k_1}{m} & \frac{\sqrt{3}}{4}\frac{k_1}{m} & -\frac{1}{4}\frac{k_1}{m} & 0 & 0 \\
0 & 0 & -\frac{3}{4}\frac{k_2}{m}e^{-iy_1} & -\frac{\sqrt{3}}{4}\frac{k_2}{m}e^{-iy_1} & 0 & 0 & -\frac{3}{4}\frac{k_1}{m} & \frac{\sqrt{3}}{4}\frac{k_1}{m} & \frac{3}{4}\frac{k_1}{m}+\frac{3}{4}\frac{k_2}{m} & -\frac{\sqrt{3}}{4}\left(\frac{k_1}{m}-\frac{k_2}{m}\right) & 0 & 0 \\
0 & 0 & -\frac{\sqrt{3}}{4}\frac{k_2}{m}e^{-iy_1} & -\frac{1}{4}\frac{k_2}{m}e^{-iy_1} & 0 & 0 & \frac{\sqrt{3}}{4}\frac{k_1}{m} & -\frac{1}{4}\frac{k_1}{m} & -\frac{\sqrt{3}}{4}\left(\frac{k_1}{m}-\frac{k_2}{m}\right) & \frac{1}{4}\frac{k_2}{m}+\frac{5}{4}\frac{k_1}{m} & 0 & -\frac{k_1}{m} \\
-\frac{3}{4}\frac{k_1}{m} & -\frac{\sqrt{3}}{4}\frac{k_1}{m} & 0 & 0 & -\frac{3}{4}\frac{k_2}{m}e^{-iy_1+iy_2} & \frac{\sqrt{3}}{4}\frac{k_2}{m}e^{-iy_1+iy_2} & 0 & 0 & 0 & 0 & \frac{3}{4}\frac{k_1}{m}+\frac{3}{4}\frac{k_2}{m} & \frac{\sqrt{3}}{4}\left(\frac{k_1}{m}-\frac{k_2}{m}\right) \\
-\frac{\sqrt{3}}{4}\frac{k_1}{m} & -\frac{1}{4}\frac{k_1}{m} & 0 & 0 & \frac{\sqrt{3}}{4}\frac{k_2}{m}e^{-iy_1+iy_2} & -\frac{1}{4}\frac{k_2}{m}e^{-iy_1+iy_2} & 0 & 0 & 0 & -\frac{k_1}{m} & \frac{\sqrt{3}}{4}\left(\frac{k_1}{m}-\frac{k_2}{m}\right) & \frac{1}{4}\frac{k_2}{m}+\frac{5}{4}\frac{k_1}{m}
\end{bmatrix}. \tag{2.6}$$

There are 12 bands corresponding to the 12 by 12 matrix D. To investigate the spin-Chern number, we derive the effective Hamiltonian [36] assuming that the other 8 bands have negligible influence. Modal displacement vector U can be rewritten as the superposition of p_1, p_2, d_1, and d_2: $U' = c_1p_1 + c_2p_2 + c_3d_1 + c_4d_2$, where c_1, c_2, c_3, and c_4 are coefficients. Based on these assumptions, Eq. (2.1) gives,

$$DU' = \begin{bmatrix} \omega_p^2 & 0 & 0 & 0 \\ 0 & \omega_p^2 & 0 & 0 \\ 0 & 0 & \omega_d^2 & 0 \\ 0 & 0 & 0 & \omega_d^2 \end{bmatrix} U'. \tag{2.7}$$

From this we get the 4 by 4 effective Hamiltonian on the basis of $[p_1\ p_1\ d_1\ d_2]$ as

$$H = [p_1\ p_2\ d_1\ d_2]^{\dagger} D [p_1\ p_2\ d_1\ d_2]. \tag{2.8}$$

And the eigenvalue problem can be written as,

$$H \begin{bmatrix} c_1 \\ c_2 \\ c_3 \\ c_4 \end{bmatrix} = \begin{bmatrix} \omega_p^2 & 0 & 0 & 0 \\ 0 & \omega_p^2 & 0 & 0 \\ 0 & 0 & \omega_d^2 & 0 \\ 0 & 0 & 0 & \omega_d^2 \end{bmatrix} \begin{bmatrix} c_1 \\ c_2 \\ c_3 \\ c_4 \end{bmatrix}. \tag{2.9}$$

(Since p_1 , p_2 , d_1 , and d_2 are normalized and orthogonal vectors, $[p_1\ p_2\ d_1\ d_2]^{\dagger}[p_1\ p_2\ d_1\ d_2] = I$.) Each element in H can be approximated to the second order using Taylor expansion.

For lattice with $k_1 < k_2$, take $k_1 = 0.8$, $k_2 = 1$ and $m = 1$. Neglect second-order off-diagonal terms, the effective Hamiltonian is (here $\gamma_x = \gamma_1 - \frac{1}{2}\gamma_2$ and $\gamma_y = \frac{\sqrt{3}}{2}\gamma_2$),

$$\begin{bmatrix} \omega_p^2 - 0.168k_2(\gamma_x^2 + \frac{1}{3}\gamma_y^2) & 0 & 0.2387ik_2\gamma_y & 0.2387ik_2\gamma_x \\ 0 & \omega_p^2 - 0.168k_2(\frac{1}{3}\gamma_x^2 + \gamma_y^2) & -0.2387ik_2\gamma_x & 0.2387ik_2\gamma_y \\ -0.2387ik_2\gamma_y & 0.2387ik_2\gamma_x & \omega_d^2 + 0.25k_2(\gamma_x^2 + \frac{1}{3}\gamma_y^2) & 0 \\ -0.2387ik_2\gamma_x & -0.2387ik_2\gamma_y & 0 & \omega_d^2 + 0.25k_2(\frac{1}{3}\gamma_x^2 + \gamma_y^2) \end{bmatrix}. \tag{2.10}$$

Since $[p_+\ d_+\ p_-\ d_-] = [p_1\ p_2\ d_1\ d_2]Q$, where $Q = \begin{bmatrix} \frac{1}{\sqrt{2}} & 0 & \frac{1}{\sqrt{2}} & 0 \\ \frac{i}{\sqrt{2}} & 0 & -\frac{i}{\sqrt{2}} & 0 \\ 0 & \frac{1}{\sqrt{2}} & 0 & \frac{1}{\sqrt{2}} \\ 0 & \frac{i}{\sqrt{2}} & 0 & -\frac{i}{\sqrt{2}} \end{bmatrix}$, H_{NT} can be rewritten on the basis of $[p_+\ d_+\ p_-\ d_-]$,

$$H_{\mathrm{NT}}^{S} = Q^{\dagger} H_{\mathrm{NT}} Q. \tag{2.11}$$

Analogous to Eq. (2.9), on the $[p_+ \; d_+ \; p_- \; d_-]$ basis,

$$H_{\mathrm{NT}}^{S} \begin{bmatrix} c_p^+ \\ c_d^+ \\ c_p^- \\ c_d^- \end{bmatrix} = \begin{bmatrix} \omega_+^2 & 0 & 0 & 0 \\ 0 & \omega_+^2 & 0 & 0 \\ 0 & 0 & \omega_-^2 & 0 \\ 0 & 0 & 0 & \omega_-^2 \end{bmatrix} \begin{bmatrix} c_p^+ \\ c_d^+ \\ c_p^- \\ c_d^- \end{bmatrix}. \tag{2.12}$$

We obtain

$$H_{\mathrm{NT}}^{S} = \begin{bmatrix} \omega_p^2 + F\left(\gamma_x^2 + \gamma_y^2\right) & A\gamma_+ & 0 & 0 \\ A^*\gamma_- & \omega_d^2 + E\left(\gamma_x^2 + \gamma_y^2\right) & 0 & 0 \\ 0 & 0 & \omega_p^2 + \mathrm{F}\left(\gamma_x^2 + \gamma_y^2\right) & A\gamma_- \\ 0 & 0 & A^*\gamma_+ & \omega_d^2 + E\left(\gamma_x^2 + \gamma_y^2\right) \end{bmatrix}, \tag{2.13}$$

where $\gamma_\pm = \gamma_y \pm i\gamma_x$, A=$0.2387ik_2$, E=$\frac{k_2}{6}$, and F=$-0.1120k_2$.

If we set the reference energy level to be $\frac{1}{2}\left[\omega_p^2 + \omega_d^2 + (E+F)\left(\gamma_x^2 + \gamma_y^2\right)\right]$, Eq. (2.13) becomes,

$$H_{\mathrm{NT}}^{S} = \begin{bmatrix} H_+ & 0 \\ 0 & H_- \end{bmatrix}, \tag{2.14}$$

with $H_\pm = \begin{bmatrix} -M + B\gamma^2 & A\gamma_\pm \\ A^*\gamma_\mp & M - B\gamma^2 \end{bmatrix}$, where $M = \frac{\omega_d^2 - \omega_p^2}{2}$, which is negative when $k_1 < k_2$, and $B = \frac{F-E}{2}$, which is also negative. Since H_{NT}^{S} has a similar formula as the Bernevig-Hughes-Zhang (BHZ) model [35], the spin Chern number can be calculated from

$$C_S = \pm\frac{1}{2}\left(sgn(M) + sgn(B)\right). \tag{2.15}$$

Since M and B are both negative, the spin Chern number for lattice with $k_1 < k_2$ is ± 1, which indicates it is topologically non-trivial. Therefore, from the topological band theory

[1] it would be expected that there would exist pseudospin-dependent edge modes at the boundary between topologically trivial and topologically nontrivial lattices.

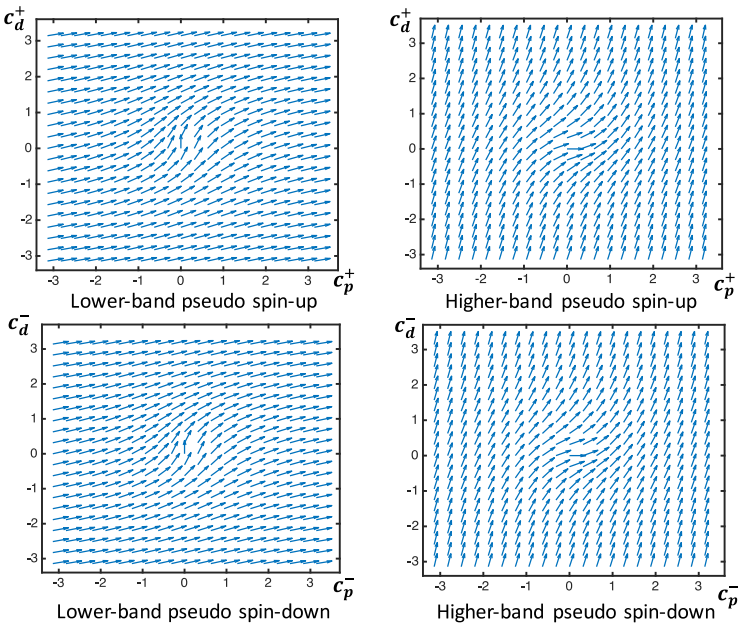

Figure 2.6 Band inversion at Γ. Projection of pseudo spin eigenvectors on $[p_+\ d_+\ p_-\ d_-]$ within the first Brillouin zone for lattice with $k_1 = 0.8$, $k_2 = 1$ and $m = 1$.

The projections of pseudo spin eigenvectors on $[p_+\ d_+\ p_-\ d_-]$ are plotted in **Fig. 2.6**. From **Fig. 2.6** we can see that for the degenerate bands below the band gap, eigenvectors on most of the Brillouin zone are *p*-like, except for near the Γ point, where the eigenvectors are *d*-like. On the other hand, eigenvectors for the higher bands are more d-like near the Γ point and p-like elsewhere. The Berry curvature $\mathcal{F}_{12}(\gamma_x, \gamma_y)$ [37] for each of the pseudo spin channels are plotted in **Fig. 2.7**. By integrating the Berry curvature over the Brillouin zone [11] , the spin Chern number can also be obtained,

$$C_s = \frac{1}{2\pi i}\sum_{\gamma_x}\sum_{\gamma_y}\ \mathcal{F}_{12}(\gamma_x, \gamma_y), \tag{2.16}$$

with values consistent with those previously obtained. The Z_2 invariant is defined as $Z_2 = n_s \pmod 2$, where $n_s = \frac{C_s^{\uparrow} - C_s^{\downarrow}}{2}$ is the quantum spin Hall conductivity [1]. The calculated spin Chern numbers $C_s^{\uparrow}$ and $C_s^{\downarrow}$ give $n_s = 1$, implying Z_2 is unity.

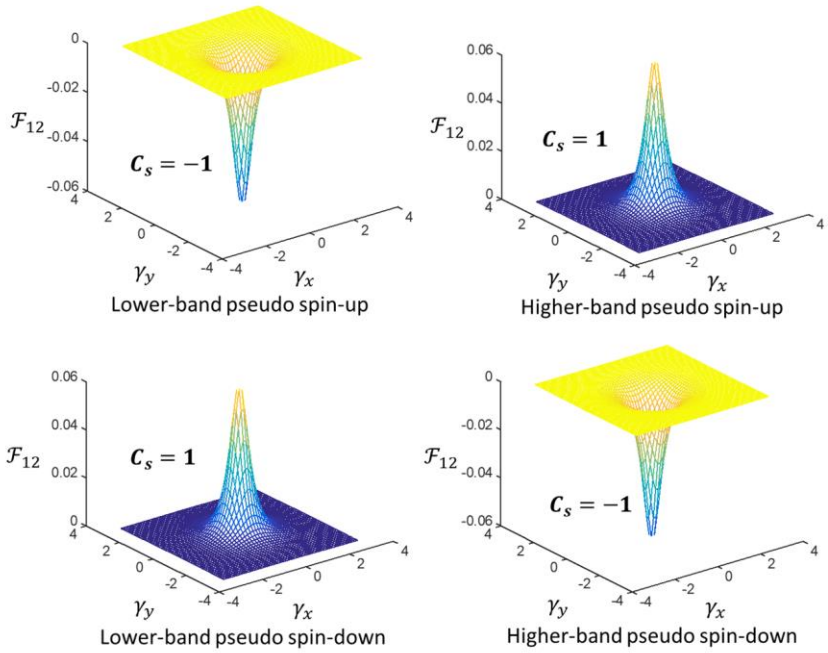

Figure 2.7 Non-trivial Berry Curvature and spin Chern number for pseudo spin channels for a lattice with $k_1 = 0.8$, $k_2 = 1$ and $m = 1$.

Similarly, for a lattice with $k_1 > k_2$, the effective spin Hamiltonian takes the same form as Eq. (16), but with $M > 0$, and $B < 0$. According to Eq. (2.15), C_s=0, which proves that the lattice with $k_1 > k_2$ is topologically trivial. The projections of pseudo spin eigenvectors with $k_1 = 1.2$, $k_2 = 1$ and $m = 1$ are plotted in **Fig. 2.8**, which shows eigenvectors of the lower bands are more p-like, while eigenvectors to the higher bands tend to be d-like, as expected for an ordinary/trivial insulator.

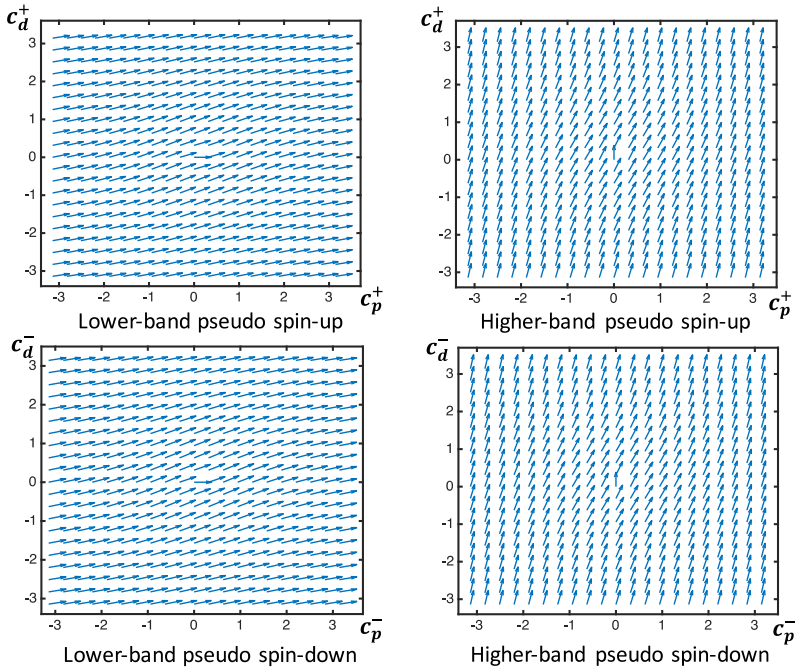

Figure 2.8 Trivial bands at Γ. Projection of pseudo spin eigenvectors on $[p_+\ d_+\ p_-\ d_-]$ within the first Broullouin zone for lattice with $k_1 = 1.2$, $k_2 = 1$ and $m = 1$.

2.3.3 Propagating Edge Modes

The pseudospin-dependent edge modes are vividly illustrated through simulations on a ribbon-shaped lattice that is periodic in one direction and of the width of one unit cell in the other direction: **Fig. 2.9(a)**. Such a supercell based lattice contains both topologically trivial (T) and nontrivial (NT) units. The NT lattice is constituted from one row of 20 unit cells and cladded by two T units of 15 unit cells (we chose the number of T and NT units so that the band diagram is relatively scale invariant). Here, the masses in the T and NT lattices are in the ratio $\frac{m^{\mathrm{T}}}{m^{\mathrm{NT}}} = \frac{1.315}{1}$, and spring constants are of the ratio $k_1^{\mathrm{T}}: k_2: k_1^{\mathrm{NT}} = 1.2: 1: 0.8$. The inter-cell spring constant k_2 is kept the same in both the T and NT units since it connects the two different lattices. The spring constants and masses were chosen such that the T and the NT units have overlapped band gap as related to the frequency ranges indicated in **Fig. 2.3(b)** and **(c)**. The band structure of the ribbon supper cell is

shown in **Fig. 2.9(b)** (The frequencies here are non-dimensionalized as $\Omega = \frac{\omega}{\sqrt{\frac{k_2}{m^{\mathrm{NT}}}}}$).

Compared to the band structures in **Fig. 2.3(b)** and **(c)**, we clearly see two additional states appear within the bulk band gap connecting the lower bands to the higher bands, as illustrated by red and green lines in **Fig. 2.9(b)**. It was noted that these two new modes propagate with a group velocity of the same magnitude but opposite signs, and correspond to the pseudospin up and pseudospin down topological edge modes. There is a mini band gap at the Γ point of the zoomed-in band structure in the inset of **Fig. 2.9(b)**, due to breaking of C_6 symmetry at the boundary of the T and the NT units. However, this mini band gap is much smaller compared to the bulk band gap (0.003:0.08), so the pseudospins are preserved, and backscattering of edge states is suppressed as shown in the time-domain simulations below. We plotted the modal displacement corresponding to the two additional states of the ribbon lattice near the Γ point ($\gamma_{\|} = 0.1\frac{\pi}{b}$, b is the lattice constant of the extended unit cell) in **Fig. 2.9(c)**. These modes are confined to the boundary between the T and the NT units, and decay into the bulk, indicative of edge mode-like character. The appearance of such modes, in the absence of any obvious spin-orbit coupling indicates attributes of a QSHE topological insulator.

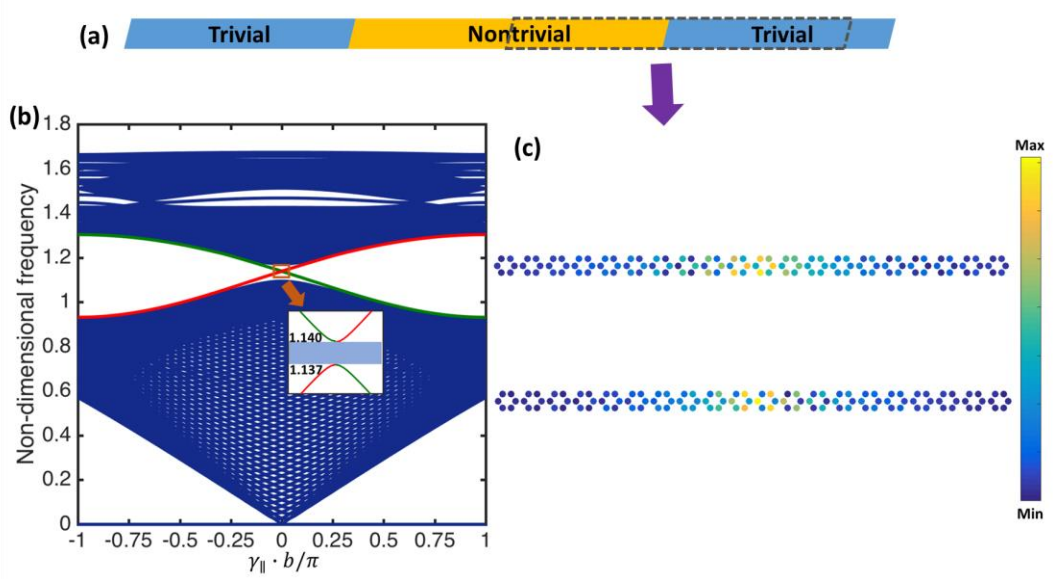

Figure 2.9 Counterpropagating topological edge states. (a) Ribbon super cell consists of 20 nontrivial unit cells cladded by 15 trivial unit cells on each end. The mases and springs are of the ratio $\frac{m^{\mathrm{T}}}{m^{\mathrm{NT}}} = \frac{1.315}{1}$ and $k_1^{\mathrm{T}} : k_2 : k_1^{\mathrm{NT}} = 1.2 : 1 : 0.8$, respectively. **(b)** The band diagram for the ribbon super cell. A pair of pseudospin up and pseudospin down edge modes are found within the bulk band gap (red and green curves). The inset shows a mini band gap at the crossing of the two helical modes. Magnitude of modal displacements of the pseudospin up and pseudospin down modes near the right boundary at $\gamma_{\|} = 0.1\frac{\pi}{b}$ are plotted in **(c)**, from which we can see that they are confined at the edge and decay into the bulk.

To verify the unidirectional propagation of the topological edge modes, we conducted time-domain numerical simulations on finite spring-mass lattices consists of both T and NT units. The governing equation for the spring-mass lattice takes the form $\ddot{u} = Au + F(t)$, where Au is the restoring/displacement-dependent force due to spring deformations, and $F(t)$ is a time-dependent excitation. We solve the equivalent ODE: $\begin{bmatrix} \ddot{u} \\ \dot{u} \end{bmatrix} = AA \begin{bmatrix} \dot{u} \\ u \end{bmatrix} + F(t)$, where $AA = \begin{bmatrix} 0 & A \\ I & 0 \end{bmatrix}$ (I is unitary matrix), using Runge – Kutta explicit time integration method (RK4) to determine the displacement u at time t. Fixed boundary conditions were applied in the simulations, *i.e.*, masses at the boundaries are connected to springs fixed to the wall.

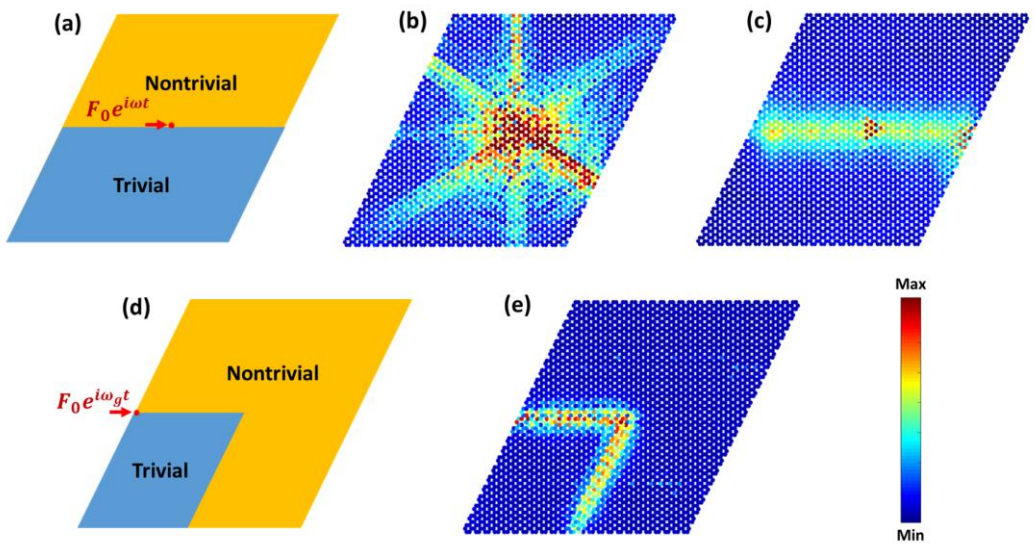

Figure 2.10 Time domain simulation of edge wave propagation. The domain is of 24 by 24 unit cells. The mases and springs are of the ratio $\frac{m^{\mathrm{T}}}{m^{\mathrm{NT}}}=\frac{1.315}{1}$ and $k_1^{\mathrm{T}}:k_2:k_1^{\mathrm{NT}}=1.2:1:0.8$ respectively. **(a)** Sinusoidal excitation force $F=F_0e^{i\omega t}$ applied on a line edge between topologically nontrivial and trivial spring-mass lattices. **(b)** and **(c)** are the simulation results with $\omega=\omega_b=0.8\sqrt{\frac{k_2}{m^{\mathrm{NT}}}}$ (frequency within the bulk bands), and $\omega=\omega_g=1.14\sqrt{\frac{k_2}{m^{\mathrm{NT}}}}$ (frequency within the bulk band gap). **(d)** is a spring-mass lattice that contains a topological edge with a sharp turning, and **(e)** simulation result on (d) with a force excitation of frequency ω_g.

Fig 2.10(a) shows the geometry of the modeled spring-mass lattice consisting of a NT and T unit, at the top and bottom, respectively. Initially all the masses are at rest. To avoid boundary reflection, we enforced an excitation force $F(t)=F_0e^{i\omega t}$ on one of the masses in the NT unit close to the middle of the NT-T boundary , with frequency $\omega=\omega_b$=$0.8\sqrt{\frac{k_2}{m^{\mathrm{NT}}}}$ corresponding to that of the bulk (from the T/NT band structure), and $\omega=\omega_g=1.14\sqrt{\frac{k_2}{m^{\mathrm{NT}}}}$ corresponding to within the band gap, respectively (for example, a lattice with $m^{\mathrm{NT}}=1$ kg, $k_2=10^6$ N/m, $\omega_b=800$ Hz, and $\omega_g=1140$ Hz). The simulation results in **Fig. 2.10(b)** and **(c)** indicate the amplitude of displacement of the masses, and illustrate that an external force (with $\omega=\omega_b$) will propagate into the bulk, while a force

(with $\omega = \omega_g$) will only excite states that propagate at the edge of the T and NT domains. A sharp discontinuity turning boundary between T and NT as indicated in **Fig. 2.10(d)** demonstrates that the edge states were immune to backscattering **Fig. 2.10(e).**

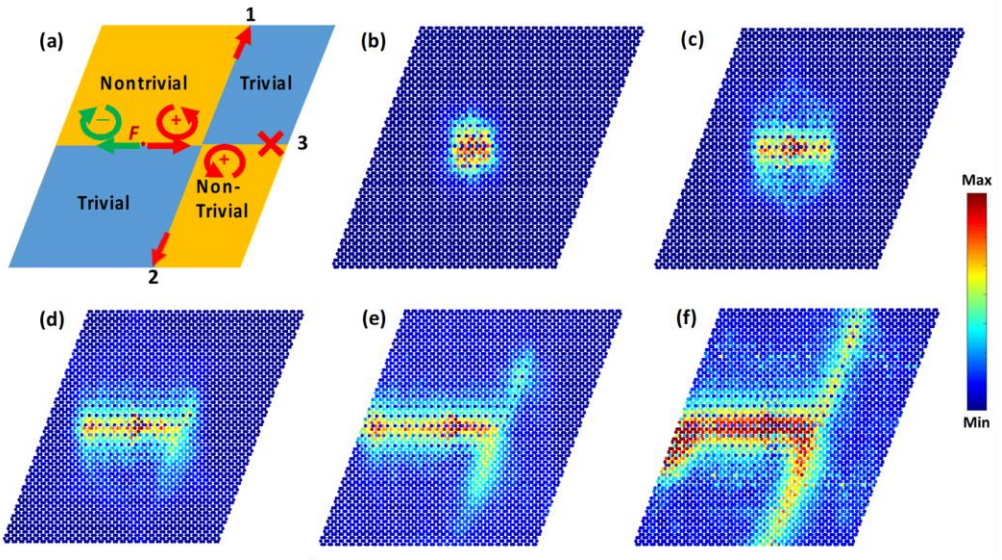

Figure 2.11 Pseudospin-dependent wave transport in a waveguide splitter. (a) Waveguide splitter divided into 4 parts, with top left and bottom right of nontrivial lattice, and top right and bottom left of trivial lattice. The cross has angle of 60° to keep the unit cells intact. An excitation force with frequency within the band gap can excite both pseudospin-up and pseudospin-down modes. Pseudospin-up modes are supported to propagate towards the right, but splits into 2 waves at the cross, that exit from port 1 and 2 respectively. But it is forbidden to exit from port 3, as right-propagate pseudospin-up modes are not supported by the domain to the right of the cross. **(b)**, **(c)**, **(d)**, **(e)** and **(f)** are snapshots of time domain simulation at t=2000t_0, 4000t_0, 6000t_0, 8000t_0 and 10000t_0, where t_0 is the time step of the simulation.

As the indicated pseudospins are symmetrized configurations of modal displacement fields, they are not prone to selective and individual excitation. However, in another application of the T-NT unit arrangement shown in **Fig. 2.11(a)**, it may be able to separate out the counter-propagating states, as broadly constructed in **Fig. 2.4(e) – (h)**. With $F = F_0 e^{i\omega t}$ it was seen that when a left-moving state (say, with positive group velocity) reaches the crossing, it will propagate up to port 1 and down to port 2 along the edges but will not propagate right to the port 3. Consequently, the trajectory of wave

propagation (**Fig. 2.11(b) – (f)**) forms a “T” shape. It was noted that the excited modes are sensitive to boundary conditions, that leads to high amplitude at the boundary.

2.4 Conclusions

In this chapter, we have shown that a mass-spring based lattice system may have attributes related to that of a topological insulator, in the presence of time reversal symmetry. Through varying the inter- and inter-unit cell spring constants of such a lattice, for a given mass, a clear and distinct variation of the band structure was seen. A concomitant change in the modal displacement fields, corresponding to a band inversion, may be generated. The deconvolution of the fields as well as their hybridization in a symmetric and antisymmetric manner yields a basis for the creation of pseudo-spins, corresponding to clockwise/counter-clockwise rotation of the modal displacement vector. Both pseudo spin-up and pseudo spin-down modalities, corresponding to the positive or negative group velocity are proposed. The existence of polarized edge states as well as corresponding modes was demonstrated through both frequency domain analysis and time domain simulations. These edge modes are topologically protected, as they are immune to backscattering when encountering sharp edges. Considering that harmonic oscillators (which are direct manifestations of spring-mass units) form the basis for many physical systems, ranging from acoustics to electromagnetics, this work yields a general foundational framework and related methodology, *i.e.*, modulating band structure and constituent modes through varying the respective spring constants of the physical system.

This chapter is based on *Quantum-spin-Hall topological insulator in a spring-mass system* by Y. Zhou, P. R. Bandaru, and D. F. Sievenpiper, New J. Phys. **20**, 123011 (2018). The dissertation author was the primary author of this material.

Chapter 3

Acoustic Wave Confining and Channeling through Coupled Resonators

3.1 Introduction

The propagation and modulation of sound has been traditionally considered in terms of an acoustic impedance: Z_{ac}, through the product of the density (ρ) and the velocity (v_s) of the medium in which sound propagates. However, it is not easy to understand the confinement of sound, through a traditional Zac formulation, as there does not seem to be a reference to which an acoustic impedance may be compared. Moreover, the absence of a magnetic field in acoustic systems does not allow for confinement and related unidirectional/chiral transport [65], without external rotational forces [11,12,44], implying pseudomagnetic fields are introduced to the system [66]. While acoustic pseudospins [13–15,47,49,58,59,67] and valley states [16,18–20,68] as related to topological surface states have been proposed to yield directionality, the surface dispersion and associated large velocity favor radiation and consequently a reduced confinement, with unclear robustness to disorder [69]. It may also be expected that wave-based interference phenomena with constructive or destructive interferences could potentially yield regions where sound is focused to be absent or present, respectively, and may be considered for sound confinement [70,71]. However, the intrinsic longitudinal/non-vectorial character of sound propagation is an issue.

An alternate strategy for sound confinement and propagation over a finite distance is to use resonators that are coupled. The flat band [72] related energy dispersions related to local resonators, would permit localization and enhance the possibility for sound confinement. We propose that such binding of sound at the subwavelength regime, may be accomplished through Helmholtz resonator (HR)-based arrangements. It has been previously discussed that bands and associated bandgaps could be generated through HRs [73–77], especially at lower energies, while the higher energy bandgaps would be mainly due to Bragg resonances. Patterning HRs onto acoustic topological lattices can render tunability of the Bragg scattering based topological band gaps in the subwavelength range [78–83]. However, band gaps arising from HR related local resonances would not support topological interface states, and the related edge modes or localized states would not generally be subject to a bulk-boundary correspondence. The objective is then to extend the confinement over a number of HR units, the cumulative length over which sound may be considered to be bound. The width of the bands and band gaps could be adjusted through a tuning of the geometrical parameters of the HR. While it has been indicated previously that the coupling of a number of HRs to a waveguide would result in a sound trapping device [84], or negative index acoustic metamaterials [85–87], the related propagation and extent of confinement was not discussed. Moreover, the ability of HR unit-based interfaces to confine sound was not considered, as would be indicated in this work.

3.2 Helmholtz Resonators Constituted Unit Cell and Confined Interfacial Modes

We consider a unit cell (of lattice constant a) comprised of four HRs with differing resonance frequencies (f), i.e., $f_4 > f_3 > f_2 > f_1$: **Fig. 3.1(a)**. The frequencies are normalized by $\frac{c_0}{a}$, where c_0 is the velocity of sound in air. As the neck and the cavity of a HR have inductor- and capacitor-like characteristics, respectively, the acoustic inductance for the neck can be written as $L = \rho l_{\text{eff}}/A,$ and the acoustic capacitance for the cavity can be expressed as $C = V/\rho c_0^2$, where ρ is density of the air, l_{eff} is effective length of the neck with end correction, A is the cross sectional area of the neck, and V is the cavity volume. The resonant frequency $f = \frac{1}{2\pi\sqrt{LC}}$ for each HR in the unit cell may be adjusted by tuning the geometry of the neck and the HR cavity [88,89]. Geometrical parameters of HRs are calibrated to yield variation in the f of the unit cell. The corresponding band structure for the unit cell is shown in **Fig. 3.1(b)**, indicating flat bands and bandgaps characteristic of the HRs. In addition to the length scales, the orientation of a HR would yield a variety of low and higher order couplings, predicated on the interaction of sound dipoles. Consequently, the assembly of the HR composed units would yield rich behavior involving both local and coupled resonances.

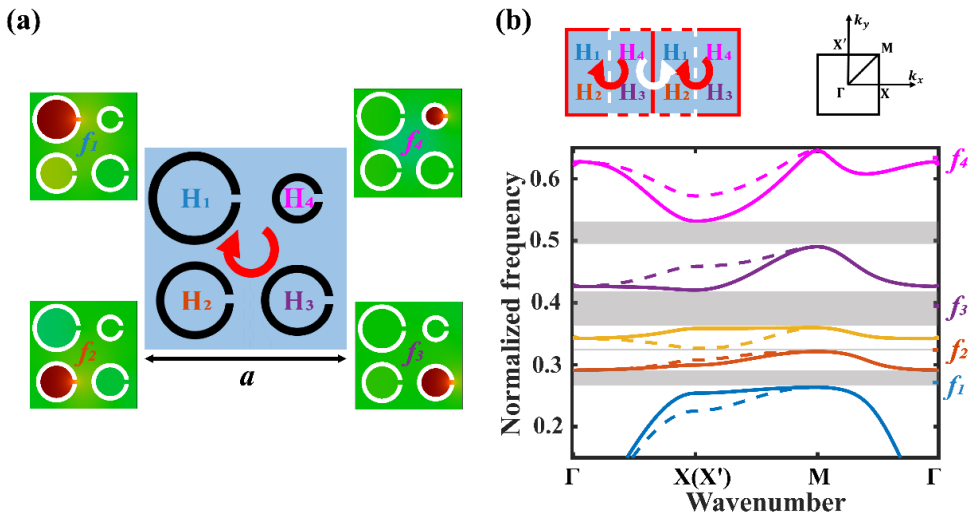

Figure 3.1 Unit cell made of Helmholtz resonators. (a) Unit cell with Helmholtz resonators arranged in a clockwise order (red arrow) from high resonant frequency to low resonant frequency. The radius of the cavities of H_1, H_2, H_3 and H_4 are $\frac{2.2}{12}a$, $\frac{1.8}{12}a$, $\frac{1.6}{12}a$, and $\frac{1}{12}a$, respectively. The length and the width of the necks are $\frac{0.5}{12}a$. H_1, H_2, H_3 and H_4 have resonant frequencies of $f_1 < f_2 < f_3 < f_4$. The circular arrow represents the direction of decreasing frequency. **(b)** Band structure of the HR unit cell in (a). Individual resonant frequencies of the resonators are marked in the figure. Solid lines are bands in the direction of $\Gamma X M \Gamma$, while dashed lines are bands in the direction of $\Gamma X' M \Gamma$.

In this chapter, we consider a manifestation of the HR unit assembly for possibilities related to robust sound confinement. We study confinement arising from the resonance coupling imbedded in the unit cell. In such an arrangement there is a relative localization of sound in the cell, *e.g.*, as illustrated in the *top inset* to **Fig. 3.1(b).** However, there is no net overall directionality, as at the interface of two identical and adjacent cells there are oppositely directed HRs, that also can be considered as the unit cell of the bulk. The unit cells are arranged so as to yield cooperative or non-cooperative resonances. The acoustic confinement in the former case is localized over a length scale of the resonator units in the cell. The subsequent channeling can be considered robust locally [90]. Herein, a particular direction is postulated through a specific arrangement of resonators where transport arises from the thermodynamically reasonable flow of energy. The spatial extent

of the region along which the sound is confined would also influence the extent of losses, where a larger (/smaller) number of cells would be involved in bounding the acoustic energy over a larger (/smaller) distance of propagation.

We indicate how HR constituted unit cell arrangements can be made, to yield specific bands or states that can be used for acoustic energy confinement. A ribbon supercell of a number of the proposed HR units yields an equivalent band structure in **Fig. 3.2(a)**, *cf.*, the energy dispersion for a single HR unit cell at the bottom of Fig. 1(b). When an interface is induced, as in *right inset* of **Fig. 3.2(b)**, through placing two HR constituted bulk structures with unit cells arranged in opposite directions, the hybridization of the energy levels across the interface is expected to yield a multiplicity of two-fold states in the band gap across a range of frequencies, akin to edge states. The related band structure is indicated in **Fig. 3.2(b),** with the interface (the *right inset*) now in the middle of the ribbon supercell. The clockwise reduction of the frequency (in *red* circular arrows – at the top) and counter-clockwise (in *white* arrows- at the bottom) enhancement, along a line in the ribbon supercell of HR units, together give rise to edge states, originating from the nominal bands [91] as depicted in **Fig. 3.2(b)**. Subsequently, the energy flow along either direction is enhanced through such edge state modes at the interface, based on resonance coupling and local confinement in the HR unit cells, as previously discussed. However, there is no directionality for the acoustic energy at the interface, over a distance larger than the considered unit cell. This may be seen through considering additionally a unit cell above the one depicted in **Fig. 3.1(b)**. Here HR units 1 and 4 have on the top as well as the bottom HR units 2 and 3, implying a frequency dependent directionality/gradation *both* at the top and bottom with equivalent energy flow and an overall non-directionality. We noted

that replacing half of the unit cells, at the interface, with a sound hard boundary (corresponding to the continuity of velocity along the boundary), yields equivalent effects. Such sound confinement phenomenon is also not unique to HRs in a square lattice, as similar arrangement of 3 or 6 HRs in a hexagonal lattice would also yield confined edge states.

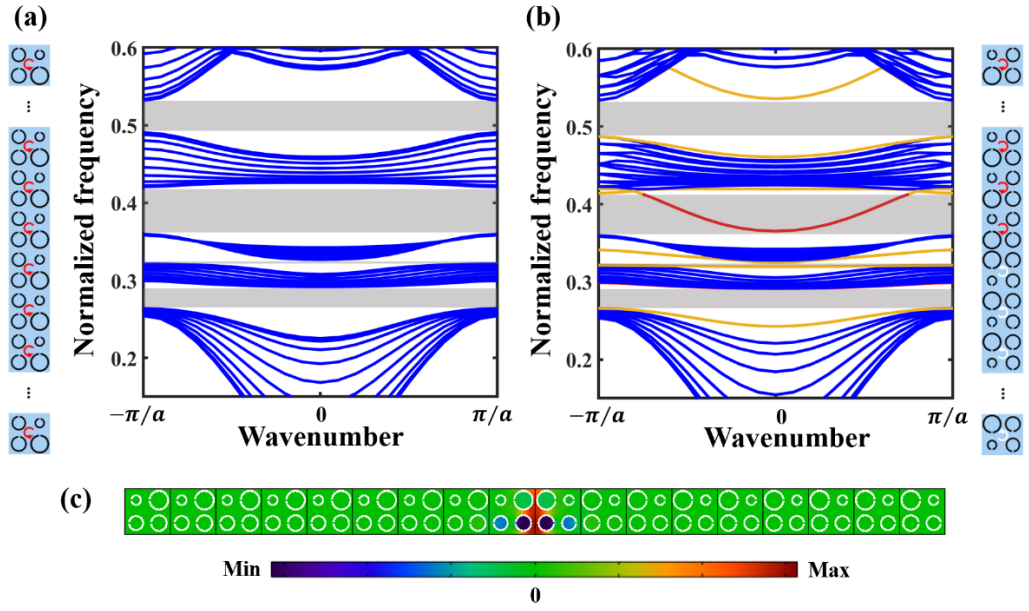

Figure 3.2 Edge states in the bandgap. Band structure of a ribbon supercell composed of **(a)** HR unit cells with resonators arranged in only clockwise order, and of (**b)** HR unit cells arranged in opposite order forming an interface, where additional confined states are found, as highlighted in red and yellow. Periodic boundary conditions are applied. **(c)** The eigen pressure field corresponding to an eigenmode marked in red in (b).

Due to local nature of the HR resonances, the edge states do not bridge the bands which helps in the confinement of sound. The edge states may then be analyzed to probe the dispersion and propagation of the confined sound. We will discuss next, the edge mode highlighted in red, in **Fig. 3.2(b),** which may be construed to be related to maximal confinement, from the large mid-gap ratio [92]. The confinement of sound related to this edge mode is shown through the corresponding pressure field at the bottom: **Fig. 3.2(c)**.

We have observed, through extensive computational simulations, the sensitivity of the confinement to the orientation of the individual HR units within the unit cell.

3.3 Local Confinement and Robustness

For instance, consider a situation where the necks of the HR units are each re-orientated in different directions, so as to face the adjacent HR, as indicated at the top *inset* to **Fig. 3.3(a).** The edge states associated with the related interface of the modified unit cell is indicated in **Fig. 3.3(a),** and the related pressure distribution is shown in the bottom *inset* to **Fig. 3.3(a)**. The necks' orientation won't change the individual resonance frequencies and the band gaps, but influences the cooperative coupling of the HRs and the edge states. From a plot of the phase of the related eigen pressure fields in **Fig. 3.3(b)**, it was observed that there was an induced phase rotation in the unit cell. It agrees with our previous discussion that the phase rotation direction in the unit cell with half a lattice constant shift has opposite phase rotation direction. The 2π phase rotation implies a rotational sound energy flux within the unit cell, results in the improved confinement at the interface, compared to the unit cell orientation in **Fig. 3.2(b)/3.2(c)**. The degree of confinement, related to acoustic energy density, is monitored in the direction perpendicular to the interface. A distance (L_c) over which there is a decrease of the pressure amplitude by 3 dB was taken to be the measure of the confinement. At $k = 0.1\frac{\pi}{a}$ (or $\lambda = 20a$), for example, for the interface in **Fig. 3.2(c),** the L_c was recorded as ~ 0.219 a (or 0.011λ), while for the interfaces depicted in **Fig. 3.3(a)/(b),** a 26% increase in confinement through a decreased L_c of ~ 0.162 a (or 0.008 λ) was indicated.

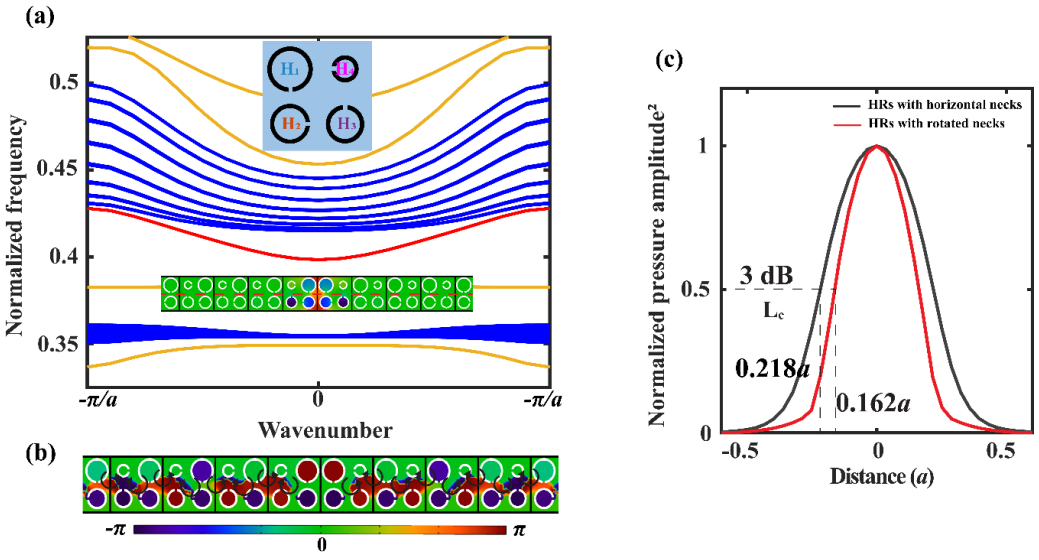

Figure 3.3 Tuning of the confinement of the acoustic energy at the interface. (a) Band structure of the HR ribbon supercell, where the necks of the HR units are each re-orientated, so as to face the adjacent HR (*top inset*). The *bottom inset* is the eigen pressure field corresponding the *edge state* (in red). **(b)** Phase plot of the eigen pressure field of the edge state mode. **(c)** The normalized pressure p^2 vs. the distance perpendicular to the interface (along the dashed line in the inset in (a)), comparing the confinement for an interface configuration, with the HRs in the unit cell all oriented (i) similarly – as in Fig. 2(c), or (ii) differently – as in the inset to (a), for the wavenumber k = $0.1\frac{\pi}{a}$.

We characterize the confinement of sound through an acoustic impedance (Z_{ac}) model, where sound follows a path of minimal impedance. The ratio of the related pressure field to the ensuing local sound velocity (v_S): $Z_{ac} = \frac{p}{v_s}$. The related acoustic pressure field for an HR unit cell related interfacial wave guide, excited by a point sound source ($p = p_0 e^{i2\pi ft}$) on the left – indicated by the * with normalized frequency of 0.3848 (wavenumber of $0.44\frac{\pi}{a}$, or 0.115 m^{-1}) is plotted in **Fig. 3.4(a)**, with the corresponding amplitudes of the pressure (p) and velocity (v) in **Fig. 3.4(b).** In contrast to the rapid decay of the confined sound modes in the perpendicular direction, as in **Fig. 3.3(c)**, the p and v_s are relatively unattenuated along the propagation direction. Standing wave-like profiles, for the p and v_s, through the path of propagation were indicated and subsequently

deconvolved so as to yield traveling wave traces. The standing waves arise from the boundaries (since scattering boundary conditions are used for the simulations) as well as from the periodic and multiple local scattering of the energy from the individual HR units at the interface, rationalizing the sound confinement. The spatial fast Fourier transform (FFT) of the pressure profile in Fig. 4 (c), indicates peaks at wavenumbers of $0\pm \Delta k$, $\pm 2 \pm \Delta k$, $\pm 4 \pm \Delta k$, $\pm 6 \pm \Delta k$… of $\frac{\pi}{a}$, where Δk is the Bloch wave number related to the lattice periodicity, and integer wavenumbers 0, ± 2, ± 4, …are from the modulation of the unit cell. Specific acoustic impedance of the interface may be estimated through simplifying the local multiple scattering phenomenon to a pair of counter-propagating traveling waves.

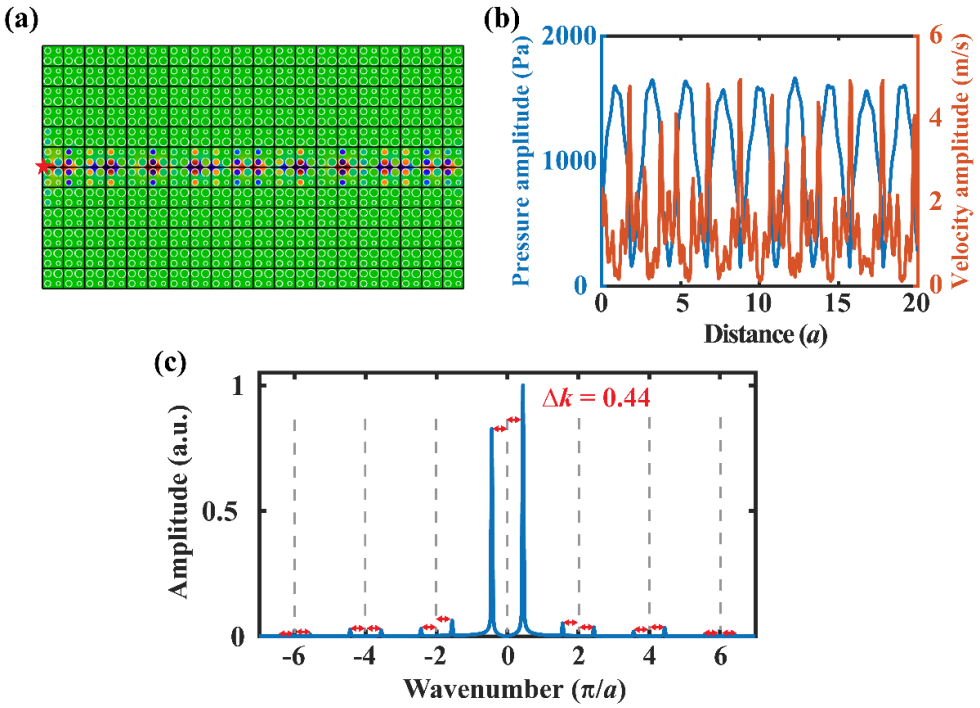

Figure 3.4 Standing-wave behavior of the HR waveguide. (a) Acoustic pressure field at the interface of two metamaterials, constituted from oppositely arranged HR unit cells. **(b)** The magnitude of pressure and velocity along the propagating interface (red dashed line). **(c)** Spatial FFT of the pressure profile along the interface.

We comment further on the essential non-band bridging character of the edge states with the implication of reduced scattering and relative insensitivity to disorder in frequency and spatial arrangement. Such perturbative disorder was introduced in the unit cells at the interface in the ribbon supercell in Fig. 2(b), as shown in **Fig. 3.5**. Frequency disorder was introduced through enlarging (/reducing) the HR cavity radius, thus decreasing (/increasing) the f. Spatial disorder was simulated by displacing the HRs from their original location. While the center column – corresponding to **Fig. 3.5(b)** indicates the type of disorder, the left column: **Fig. 3.5(a)** shows the modifications to the band structure, and the right column: **Fig. 3.5(c)** depicts the resulting acoustic pressure. The sound source is situated at the bottom. The top, middle, and bottom insets of **Fig. 3.5(b)** illustrate the cases of reduced frequencies, increased frequencies, and spatially displaced resonators: $H_1$and H_2, at the interface. It was seen that fabrication irregularities may be tolerated in the proposed design. From **Fig. 3.5(a)**, it may be observed that both frequency and spatial disorders tend to push the edge states up or down into the bulk bands. The edge state, and the corresponding energy flow, is robust if the disorder is not so much as to merge the edge band with the bulk bands. **Fig. 3.5(c)** shows a driven-mode simulation of sound propagation through a HR unit cell constituted waveguide that includes all three types of disorders in **Fig. 3.5(b)**.

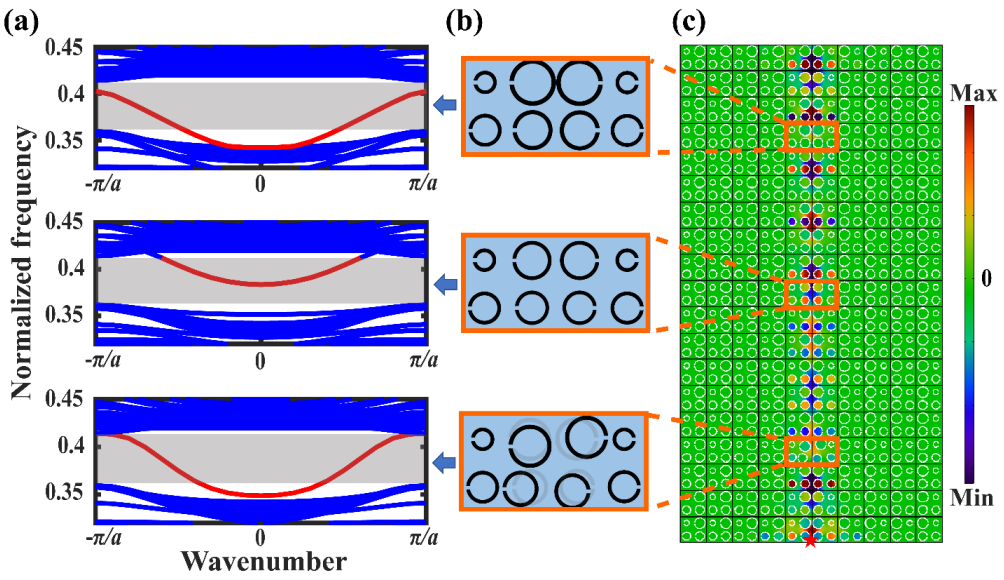

Figure 3.5 Robustness of the HR waveguide. (a) Band structure of the ribbon supercell in Fig. 2 (b) with frequency or location disorder at the interface. The corresponding disorders at the interface is shown in **(b)**. Here, Top: interface disorder with reduced frequencies, where the radius of the cavities related to H_1, H_2 are increased by ~ 10% to $\frac{2.4}{12}a$, $\frac{2}{12}a$, respectively. Middle: interface disorder with increased frequencies, where the radius of H_1, H_2 are decreased by ~ 10% to $\frac{2}{12}a$, $\frac{1.7}{12}a$, respectively. Bottom: interface disorder with displaced H_1 and H_2. **(c)** The sound pressure corresponding to the indicated frequency and location disorder in (b), along the direction of wave propagation. A point sound source ($p = p_0 e^{i2\pi ft}$ (*) is situated at the bottom.

The propagation of sound in **Fig. 3.4(a)** is over the straight-line path, correspondent to the interface of adjacently placed HR units. Generally, non-collinear sound propagation has been challenging to implement, given that there seems to be no ideal arrangement of the unit cells at the turn regions. At the ends of any line, a localized state is expected which would be either reflected back or dissipated. Alternately, from the viewpoint of impedance matching, the acoustic energy would be not (/totally) reflected if the impedance at the end is matched (/infinitely large) with various degrees of reflection for intermediate cases. We observed that the reflection and transmission could be tailored through HR unit cell configurational changes, *e.g.*, through re-tuning of the frequencies of the resonators at the tuning point, taking advantage of the robustness of the interface modes, discussed

previously. For instance, **Fig. 3.6(a)** indicates an arrangement where almost total stoppage/reflection was seen when the edge mode, propagating over the interface, encounters a 90^{o} sharp turn. An inevitable disorder occurs in the highlighted corner region with detailed arrangement shown in the *inset*, even though the rest of the interface is intact and ordered. The transmission is calculated to be ~ 0.002. Alternately, a change in the individual HR radius (which tunes the resonator frequency) can be made where considerable transmission of the sound energy around a corner is accomplished: **Fig. 3.6(b).** The resonance frequencies of the H_1, H_2 and H_3 in the highlighted corner HR unit cell are modified to smaller values, *i.e.*, $f_{0.5}$, $f_{1.5}$ and $f_{2.5}$ ($H_{0.5}$, $H_{1.5}$ and $H_{2.5}$), inducing decreased-frequency disorder to the horizontal interface, and an increased-frequency disorder to the vertical interface in the 90^{o} turn. A dramatic increase in wave transmission was then observed. Consequently, acoustic wave confinement around a closed path is now possible, as shown in **Fig. 3.6(c).**

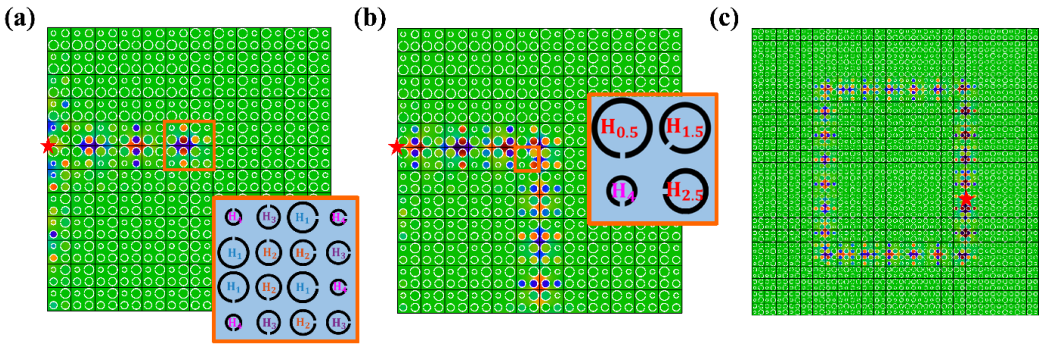

Figure 3.6 Acoustic closed circuit. (a) A 90^{o} abrupt turn (see closeup of the corner in the *inset*) in the propagation path with significant energy reflection. **(b)** A rearrangement of the corner unit cell by modifying the resonant frequency of the corner HRs (see *inset*), yields smoother turns. **(c)** Acoustic energy confinement in a closed circuit with corner arrangement adapted from **(a)**.

However, it is not clear as to what *exactly* the corner configuration ought to be for the continued motion of the sound current. From a consideration of the transmitted power,

in terms of the acoustic intensity $I = pv_s$, *before* and *after* the turn, it was noted that while the p is diminished to $0.81p$, the v_s is reduces to $0.69v_s$, which give the total transmission of ~ 56% – an increase of ~ 300 compared to the transmission of **Fig. 3.4(d**). Perhaps, the magnitude of the transmission may be used as an approximate measure of the suitability of a corner geometric configuration. Future study should focus on the further improvement of the transmission through computational search and related optimization of the corner geometry of the individual HRs.

Moreover, while we have indicated acoustic confinement robust to possible disorders induced by fabrication, in reality, losses are inevitable and need to be taken into consideration. We considered the viscous and thermal boundary-layer induced losses due to acoustic energy dissipation though the narrow necks of the HRs [93–95], and found that the acoustic wave is well confined, *i.e.*, a 3 dB loss is sustained for propagation over 450 unit cells/100 wavelength.

3.4 Conclusions

We have designed a subwavelength acoustic waveguide based on HRs that has great confinement and is robust over lattice disorders. Taking the advantage of robustness of the waveguide, we are able to make sound turn sharp corners. The proposed scheme of HR configuration-based sound confinement can be extended to three-dimensions, where acoustic confinement would now be over an area. While the direction of propagation is based on the orientation of the sound source, the proposed scheme does not allow for unidirectional energy transport. Indeed, given the absence of a magnetic field, Dirac-like points, or nonlinearity in the structure, the propagation of the acoustic waves is yet

bidirectional. However, the presence of the HRs in a unit induces a local binding which when added together over several units may be construed as the confinement of sound. Our formulations also allow for an alternate viewpoint of the specific acoustic impedance in terms of the ratio of the driving pressure of acoustic wave propagation to the local acoustic velocity. A closed-path acoustic circuit suggests the possibility of confining sound waves to a very small region, even to a point.

This chapter is based on *Confining and channeling sound through coupled resonators* by Y. Zhou, P. R. Bandaru, and D. F. Sievenpiper, J. Appl. Phys. **129**, 095103 (2021). The dissertation author was the primary author of this material.

Chapter 4

Unidirectional Surface Acoustic Waveguide based on a Defect Line in a Triangular Lattice

4.1 Introduction

Surface acoustic waves (SAWs) have been appealing for applications ranging from precise on-chip manipulation of particles and fluids in acoustofluidics [96–105], to probing and controlling elementary excitations in condensed matter [106–111]. In all such applications, low loss SAW guiding is desired. While waveguides [112] are utilized for confinement and control of SAW propagation, beam steering [113] due to anisotropy of the piezoelectric substrate, and lateral diffraction of SAWs cause energy dissipation, degrading the performance. SAW filters are also key components for wireless devices [114,115]. As modern multi-band systems continue to shrink in size, it is becoming increasingly important to miniaturize such SAW components without sacrificing performance. A design scheme to steer the acoustic waves while suppressing backscattering would be of significant benefit.

A promising method to create unidirectional and backscatter-immune SAW waveguides may be through non-reciprocal devices, which are based on a broken time-reversal symmetry (TRS) and can exhibit one-way transmission of propagating waves. For

instance, the intrinsic TRS breaking in ferromagnetic materials may lead to non-reciprocal SAW propagation [116–118], due to the different absorption in the $+k$ and $-k$ directions. However, the absorption difference is usually small, and the use of magnetic materials in devices is usually undesirable. Another way to achieve acoustic non-reciprocity is to use nonlinear effects [119–122], but the manipulation of propagation direction remains challenging in these nonlinear systems. Topological insulators (TIs) based upon the quantum Hall effect [3,36] has been extended to bosons by introducing external rotational forces for many photonic [6,37,123–126] and mechanical/acoustic systems [7,11,44,46,127–130] to build non-reciprocal waveguides. However, the realization of non-reciprocal topologically protected modes in the technologically relevant case of SAW has thus far proved elusive.

Alternately, while TIs based on lattice symmetry breaking are reciprocal and protected by TRS, the related principles still allow for robust and unidirectional wave guiding. For example, tuning the inter- and intra- cell coupling while maintaining C_{6v} symmetry in honeycomb lattices [14,41,49], or breaking the z-directional mirror symmetry in bianisotropic materials [15,39,131], can introduce pseudospins that mimic the quantum spin Hall effect [50–52,132], yielding spin selective unidirectional passage. Unidirectional valley degree of freedom based TI (VTI) waveguides may also be constructed by breaking inversion symmetry in honeycomb lattices [133]. We aim to extend related ideas to on-chip phononic devices [17,134,135]. However, due to the lattice symmetry requirement, most of the existing on-chip designs have utilized suspended structures for bulk acoustic wave or Lamb waves, and an easy corresponding extension for SAWs is still lacking.

In this chapter, we report a scalable, non-suspended, fully integrated, reciprocal, and unidirectional on-chip SAW waveguide fabricated on a lithium niobate ($LiNbO_3$) platform. In our implementation, the unidirectional SAW waveguide is created by a defect boundary in a triangular phononic lattice. We demonstrate that while the triangular lattice has a vanishing Berry curvature, the intrinsic embedded phase vortices give rise to unidirectional wave transport. We prove that, compared to VTIs, our simpler waveguide structures show much better lateral confinement without sacrificing the directionality. The confined, robust, and unidirectional SAW routing phenomenon has been verified through experiments, which demonstrate that our design overcomes the limitation of beam steering in the substrate. The propagating SAW is capable of making sharp turns along the defect-line waveguide (DLW) with low reflection loss. By incorporating the proposed waveguides, there is now a possibility of wave propagation in any chosen direction, which can benefit many on-chip SAW applications.

4.2 Unidirectional SAW Waveguide in a Triangular Lattice with Zero Berry Curvature

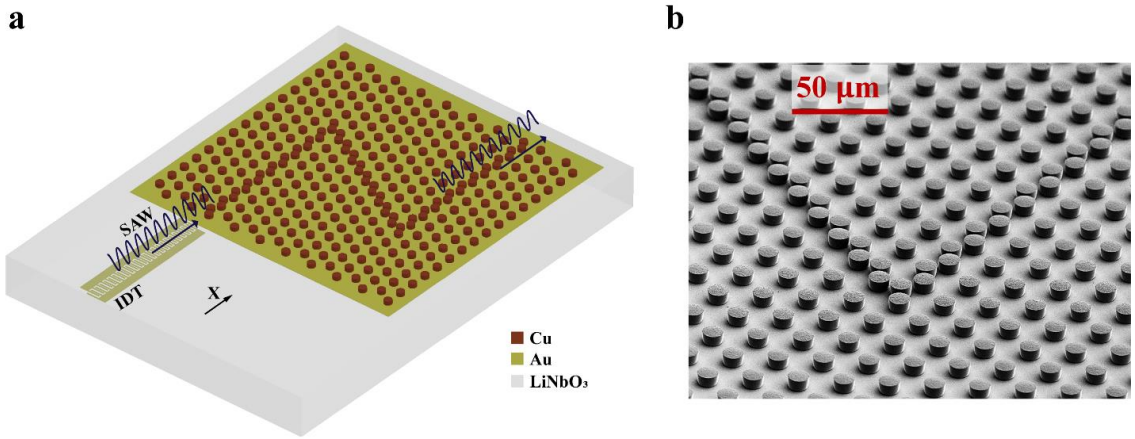

Figure 4.1 The DLW for SAW. (a) Schematic of the proposed SAW DLW composed of phononic crystal of copper pillars arranged in a triangular lattice on a 127.68° Y-rotated X-propagating $LiNbO_3$ wafer. The incident SAW in the X direction is provided by a broadband chirped IDT. **(b)** SEM image with a zoomed-in view of the fabricated SAW waveguide. The Cu pillars are 11.5 µm in diameter and 6.2 µm in height, with lattice constant a=24 µm, grew on a 400 nm Au seed layer on top of a 500 µm $LiNbO_3$ wafer.

The proposed SAW waveguide is formed by a defect line in a triangular array of copper pillars on 127.68° Y-rotated X-propagating $LiNbO_3$ wafer, as shown in **Fig. 4.1(a)**. The entrance and exit ports of the waveguide are aligned with the X direction of the $LiNbO_3$ wafer. The lattice of identical copper pillars introduces periodic modulation for SAWs, inducing a related dispersion and band structure (with bands and bandgaps). **Fig. 4.1(b)** shows a scanning electron microscopy (SEM) image of the fabricated SAW waveguide, where the copper pillars were grown onto the $LiNbO_3$ substrate through electrochemical deposition (see **Methods**). To study the SAW propagation, a broadband interdigital transducer (IDT) with a narrow aperture (see **Methods**) is fabricated on the same wafer and excites SAWs in the X direction from the entrance port.

It has previously been observed that a Dirac degeneracy for SAW at the *K* point occurs in a honeycomb lattice consisting of metallic pillars on $LiNbO_3$ [136] (also shown in **Fig. 4.2 (a)** and **(d)**). Through differentiating one pillar from the other in the unit cell by

shrinking the diameter of one of the pillars in the honeycomb lattice, say pillar B, as shown in **Fig. 4.2(b),** the structure may be equated to a SAW VTI [137]. The C_{6v} symmetry of the lattice is reduced to C_{3v}, which lifts the Dirac degeneracy at K and forms a SAW bandgap, as shown in **Fig. 4.2(e)**. Consequently, topologically protected valley edge states for SAWs are expected to be found in the bandgap formed. Further shrinking the pillar B diameter to zero, the number of copper pillars in the unit cell reduces from two to one, and the honeycomb is transformed into a triangular lattice [21], as shown in **Fig. 4.2(c)**. Since the SAW modes are supported by the mechanical resonances of the copper pillars (see subsection 4.8.1), reducing the number of pillars by half reduces the number of SAW modes by half. As shown in **Fig. 4.2(f)**, a larger SAW bandgap then forms from 73.08 MHz to 88.13 MHz.

We observed an intrinsic phase rotation for the out-of-plane displacement u_z in the unit cell of the triangular lattice, where, in contrast to the valley TI, its Berry curvature vanishes. The phase distribution map of u_z at the K point of the Brillouin zone for the bands highlighted in red in **Fig. 4.2 (d), (e) and (f)** for the honeycomb lattice, the valley SAW TI, and triangular lattice are shown in **Fig. 4.2 (g), (h) and (i)**, respectively. It may be observed that the phase shows greater uniformity close to the pillars. In the case of the valley SAW TI, **Fig. 4.2(h)**, the relative position of the pillars leads to two vortices with opposing directions from a 2π phase rotation: one showing a counterclockwise vortex at the center of three pillars arranged in upwards triangles, and one showing a clockwise vortex at the center of three pillars arranged in downward triangles. These phase vortices indicate the presence of circular-polarized orbital angular momentum (OAM) and indicate a chiral property for u_z throughout the bulk of the valley TI lattice [54,138]. The OAM

waves of opposite signs suggest unidirectional interfacial modes would be supported when the directionality is reinforced rather than opposed at a boundary or interface. The phase plot in **Fig. 4.2(i)** shows that the triangular lattice with only one pillar may still be mapped to an intrinsic OAM as in a topologically nontrivial valley TI, implying unidirectional confined edge modes would still be supported in the bandgap. However, despite the similarity, the triangular lattice maintains a C_{6v} point group symmetry, while the lattice symmetry in a valley structure is reduced to C_{3v}. For the valley TI, inversion symmetry results in $\pm\pi$ Berry phase accumulation around K or K', as shown in **Fig. 4.2(j)**. By contrast, with no TRS breaking or inversion symmetry breaking, the Berry curvature vanishes everywhere in the Brillouin zone for the triangular lattice (See subsection 4.8.2). This is illustrated in **Fig. 4.2(k)**, where the Berry curvature is shown to be zero [139] around K, in clear contrast to the case of the valley structure.

The spatial arrangement of the phase vortices suggests a gauge dependance on the existence of edge modes along the border. This can be likened to the topological crystalline insulator phases found in Kagome crystals [31–33], where the underlying symmetry is determined by the choice of unit cell. We can imagine the limit of a "breathing" Kagome unit cell as equivalent to a triangular lattice, with each lattice cite partially overlapping with the neighboring cells [32,140]. Unlike Kagome crystals, however, the physical realization given here maintains the C_{6v} rotational symmetry for suitable choices in unit cell. Despite this, it can be seen (see subsection 4.8.3 and 4.8.4) that for the unit cell definitions that result in C_{3v} edges along finite boundaries (as are studied here) the edge modes can be described by a nontrivial symmetry indicator [34] that describes the effect of the phase vortex. The existence of unidirectional modes is therefore a direct consequence of the real

space behavior of the finite crystal along certain boundaries, rather than the reciprocal space influence of valley-based effects. The symmetry indicator provides a direct measure of these real space effects, as is visually represented in the phase vortices seen in **Fig. 4.2(i)**.

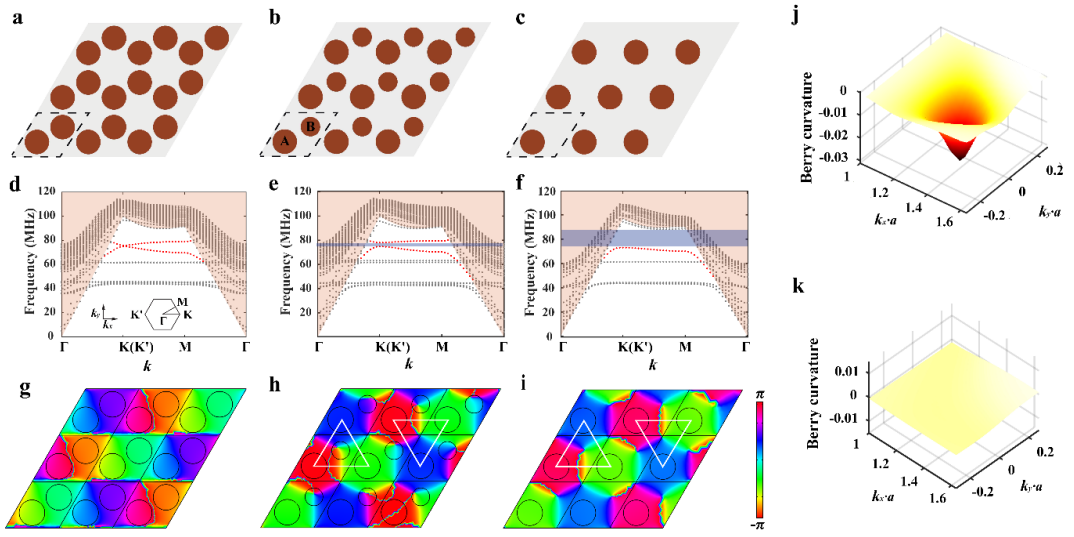

Figure 4.2 Phase vortices in triangular lattices aiding SAW confinement. (a) Honeycomb lattice, **(b)** VTI with $r_B = 0.8r_A$ and **(c)** a triangular lattice of Cu pillars of 11.5 μm diameter and 6.2 μm height on 500 μm $LiNbO_3$ substrate. Calculated band dispersions along Γ-K (K′)-M-Γ direction for **(d)** the honeycomb lattice, **(e)** the VTI, and **f** the triangular lattice. Bandgaps for SAWs due to symmetry breaking are shaded in blue. Bulk acoustic wave bands are shaded in orange. We focus on bands highlighted in red dashed lines this paper. Simulated phase maps for the **(g)** honeycomb lattice, **(h)** VTI and **(i)** the triangular lattice at K. Phase plots for the VTI and the triangular lattice shows two vortices: one at the center of the downward triangles, and one at the center of the upward triangles. The upward triangles Δ and downward triangles ∇ indicate opposite phase vortices. **(j)** Berry curvature for the triangular lattice around K $(\frac{4}{3}\frac{\pi}{a}, 0)$. The Berry curvature is zero thoroughout the BZ with no accumulation around K, which shows a clear contrast to **k** that of the VTI.

4.3 Unidirectional SAW Edge States

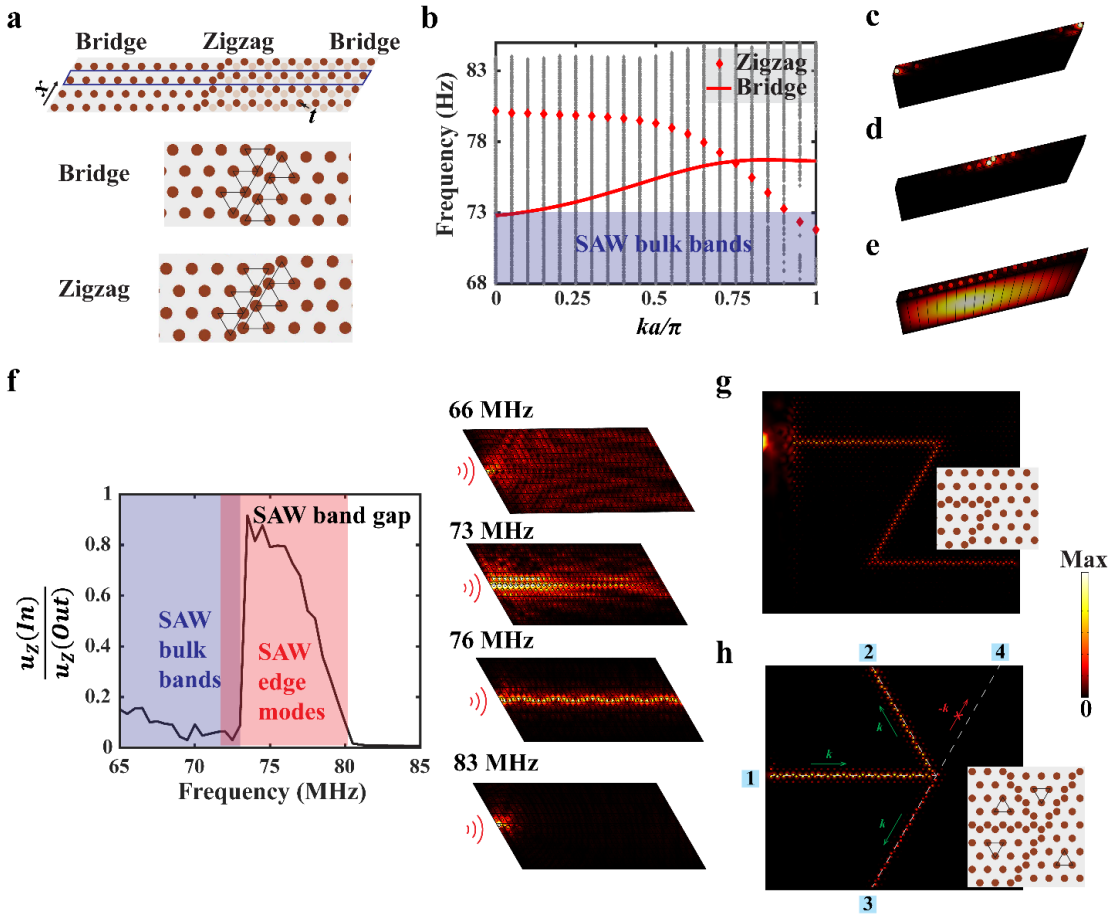

Figure 4.3 Unidirectional SAW modes at the DLW. (a) (top) A DLW created by shifting one half domain of the triangular phononic crystal of $\vec{t} = \frac{\sqrt{3}}{3}a$ in the direction perpendicular to the waveguide. The light red color shows the positions of the pillars before the shift. A ribbon super cell is highlighted in blue, with a zigzag defect line in the middle and bridge defect line at the edges (as periodic boundary condition is applied in *x* direction. **(bottom)** The bridge defect line and zigzag defect line in the triangular lattice. The upward triangles Δ and downward triangles ∇ indicate opposite phase vortices. **(b)** Band dispersions for the ribbon super cell. **(c)** Eigen-displacement u_z for the edge mode confined at the bridge defect line. **(d)** Eigen-displacement u_z for the edge mode confined at the zigzag defect line. **(e)** Eigen-displacement u_z for the bulk acoustic modes in the SAW bandgap. **(f) (left)** u_z amplitude at the exit port of a straight zigzag DLW of $64a$ length normalized by u_z amplitude at the entrance port from 65 MHz to 85 MHz. **(right)** u_z field plots for the straight zigzag DLW at 66 MHz (within SAW bulk bands), 73 MHz (edge mode within SAW bulk bands), 76 MHz (edge mode within SAW bandgap) and 83 MHz (within SAW bandgap). **(g)** Simulated u_z field for a Z-shaped zigzag DLW with an excitation of 76 MHz. **(h)** A "magic T" junction for the zigzag DLW. The "magic T" divide the domain into 4 parts with 60°, 60°, 60°and 180° angles at the junction. The four sub-domains are denoted by the Δ and ∇ respectively. The excitation is at 76 MHz at port 1.

We first prove, through numerical simulations, the existence of unidirectional SAW edge states, despite zero Berry curvature. We construct a DLW in the lattice where the phase on its two sides shows opposite vortices with enhanced direction of the energy flow at the defect line (see **bottom** figure in **Fig. 4.3(a)**). Here, a waveguide was created by shifting the right half domain of the triangular lattice $t = \frac{1}{\sqrt{3}}a$ in the direction perpendicular to the zigzag defect line, as illustrated in the top figure of **Fig. 4.3(a)**. It can be observed that the domain on the left of the waveguide is truncated such that the pillars are arranged in downward triangles along the boundary, while along the right side of the waveguide the pillars are arranged in upward triangles. The phase vortices are opposite on the two sides, which leads to energy flux reinforced in one direction, giving rise to unidirectional SAW transport at the defect line.

To find guided modes along the interface, we considered the band dispersion of a ribbon supercell with a zigzag defect line in the middle and a bridge defect line on the edges, as highlighted in the top figure of **Fig. 4.3(a)**. Periodic boundary conditions are applied in both the x direction and the direction along the waveguide, and the calculated band diagram is plotted in **Fig. 4.3(b)**. The zigzag and bridge bands fall mostly into the SAW bandgap of the triangular lattice, with their corresponding eigen-displacement (u_z) amplitude fields shown in **Fig. 4.3(c)** and **Fig. 4.3(d)**, indicating the existence of the edge states at both the zigzag defect line and the bridge defect line. The edge mode associated to the zigzag defect line spans a wider frequency range (71.8 MHz to 80.18 MHz) compared to the edge mode confined at the bridge defect line (72.8 MHz to 76.65 MHz). Some bulk acoustic wave modes were observed in the SAW bandgap, as shown by the grey dots in the band structure. These modes decay rapidly into the bulk and do not couple to

the SAW modes; therefore, they can be safely ignored. **Fig. 4.3(e)** shows the u_z of one of the bulk modes and related bulk wave behavior. Since these modes propagate into the bulk at a higher velocity, we expect them to have minor/negligible coupling with our SAW edge modes. **Fig. 4.3(f)** shows the u_z amplitude at the exit port of a straight zigzag DLW of 64a length normalized by the u_z at the entrance port. It can be observed that the SAW waveguide has high transmission from 73.08 MHz to 80.18 MHz, related to the edge mode. For frequencies below 73.08 MHz (within the SAW bulk bands), SAWs radiate throughout the whole surface, while for frequencies above 80.18 MHz the bandgap prohibits SAW propagation, leading to low transmission. In **Fig. 4.3(g),** a zigzag DLW with two 120-degree sharp turns was excited at 76 MHz, demonstrating robust SAW waveguiding with little reflection. To verify the unidirectionality, we simulated a "magic T" junction as shown in **Fig. 4.3(h)**, constituted from four DLWs that separate the domain into four parts. When sending a wave into port 1, the excited SAW will propagate in the direction in which the wave sees the upward triangles on its left and the downward triangles on its right. As shown in **Fig. 4.3(h)**, the SAW excited at port 1 couples to port 2 and 3 but not port 4, as the waveguide connected to port 4 only supports SAW in the opposite propagation direction. The triangles, corresponding to the phase vortices, uniquely determine the direction of propagation, unlike ordinary defect modes. Consequently, it has been clearly indicated that edge states at the DLW are unidirectional.

4.4 Confinement and Robustness of the SAW DLW

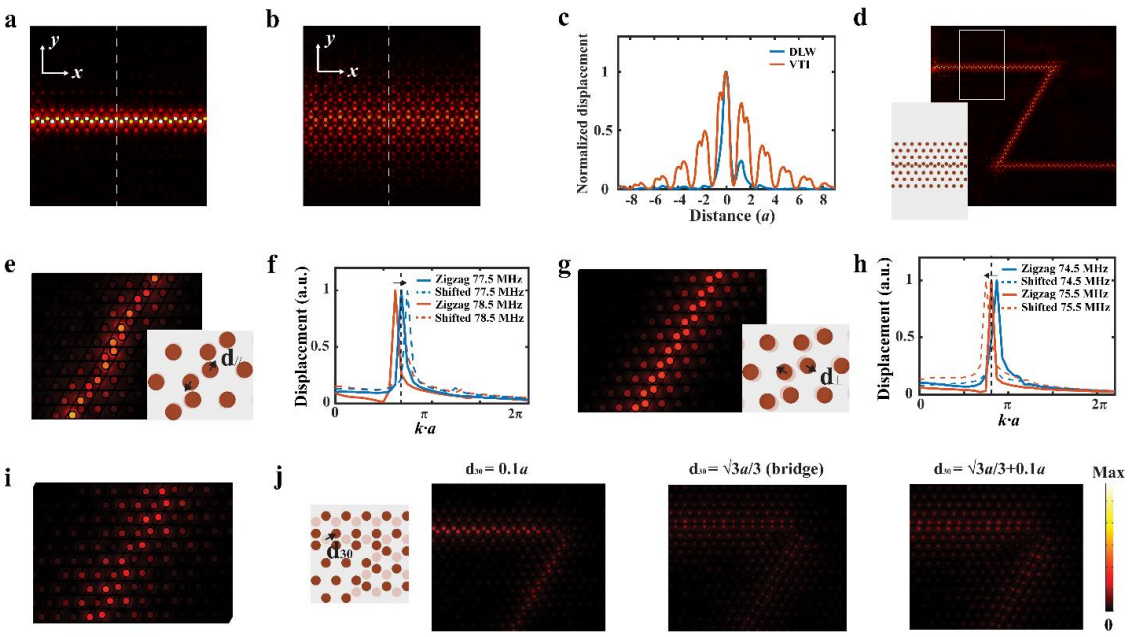

Figure 4.4 Confinement and robustness of the DLW. (a) The proposed zigzag DLW excited at 76 MHz, with greater confinement. **(b)** the VTI with $r_B = 0.8r_A$ excited at 76 MHz, shows less confinement. **(c)** Normalized displacement distribution in *y* direction (the direction perpendicular to SAW propagation *x*) for the zigzag DLW compared to that of the VTI. **(d)** Z-shape zigzag DLW with only 3 rows of pillars on both sides. The inset shows a zoomed-in view. (**e)** A zigzag DLW with a shift $d_{\parallel} = 0.0425a$ along the waveguide excited at 76 MHz. **(f)** Spatial FFT for u_z along the shifted waveguide in **e** compared to that of a zigzag DLW at excited 77.5 MHz and 78.5 MHz. The SAW that travels at 77.5 MHz along the zigzag DLW is of the same wavevector as the SAW travels along the shifted waveguide at 78.5 MHz, indicating that the edge modes move to higher frequencies. **(g)** A zigzag DLW with a shift $d_{\perp} = 0.05a$ perpendicular to the waveguide excited at 76 MHz. **(h)** Spatial FFT for u_z along the shifted waveguide in **(g)** compared to that of a zigzag DLW at 74.5 MHz and 75.5 MHz. The SAW that travels at 75.5 MHz is of the same wavevector as the SAW travels along the shifted waveguide at 74.5 MHz, indicating that the edge modes move to lower frequencies towards the bulk SAW bands. **i** A zigzag DLW with a shift $d_{\perp} = 0.15a$ perpendicular to the waveguide excited at 74.5 MHz. **k** Bent zigzag DLWs with a shift $d_{30} = 0.1a$, $\frac{\sqrt{3}}{3}a$ (bridge DLW) and $(\frac{\sqrt{3}}{3} + 0.1)a$ in the direction of 30° towards the waveguide excited at 76MHz, from left to right, respectively.

We compare the confinement of the proposed DLW with a VTI. The displacement fields at 76 MHz are shown in **Fig. 4.4 (a)** and **(b)** for our DLW in contrast to a VTI (**Fig. 4.2(b))**, respectively, with the displacement perpendicular to the waveguide plotted in **Fig. 4.4(c)**. The DLW shows a much faster decay along the in-plane orthogonal direction *y*,

with 3 dB decay in 0.264a, and 20 dB decay in 0.533a. On the other hand, the displacement for the VTI spreads out 5 times more, with 3 dB decay in 1.324a, and 20 dB decay in 3.140a. The capability of confining SAW in a narrow region allows us to construct a DLW with fewer unit cells in the orthogonal direction. **Fig. 4.4(d)** demonstrates that a Z-shape zigzag DLW containing only three unit cells on either side of the interface still guides the SAW as expected.

The waveguides we discussed above are constructed by shifting the pillars to form a perfect zigzag or bridge grain boundary defect line in a triangular lattice. We explored further the configuration of the defect line and how it affects the confinement of the SAW edge states. **Fig. 4.4(e)** shows a waveguide with the left and right domains of the zigzag interface both shifted in the direction parallel to the interface by $d_{\parallel} = 0.0425a$, while **Fig. 4.4(g)** illustrates a waveguide with the left and right domains of the zigzag interface both shifted away from the interface by $d_{\perp} = 0.05a$. It can be observed that the waveguides still support SAW propagation and indicate the robustness of the related edge modes. However, from the spatial FFT for the two cases, as shown in **Fig. 4.4(f)** and **Fig. 4.4(h)**, respectively, the edge mode is shifted to higher or lower frequencies. **Fig. 4.4(i)** shows the case with perpendicular shifting of $d_{\perp} = 0.15a$, where the SAW is still guided through the interface, but is less confined to the waveguide. This is because shifting the two domains away from each other will reduce the coupling of the phase vortices at the interface and push the edge modes more towards the SAW bulk bands, leading to a less confined interfacial mode. **Fig. 4.4(j)** shows 120-degree bent DLWs with half of the domain shifted d_{30} in the direction 30^{o} to the zigzag interface. The field plots in **Fig. 4.4(j)** are for the cases when $d_{30} = 0.1a$, $\frac{\sqrt{3}}{3}a$ and $(\frac{\sqrt{3}}{3} + 0.1)a$, respectively. Similarly, as the shifting

distance d_{30} increases, the SAW also becomes less confined. Note that when $d_{30} = \frac{\sqrt{3}}{3}a$, the waveguide resolves to a perfect bridge interface. As suggested by **Fig. 4.3(b)**, the edge mode of a bridge interface is closer to the SAW bulk band, with slower propagation velocity compared to that of a zigzag interface, resulting in reduced confinement.

4.5 Experimental Observation of the SAW Waveguiding

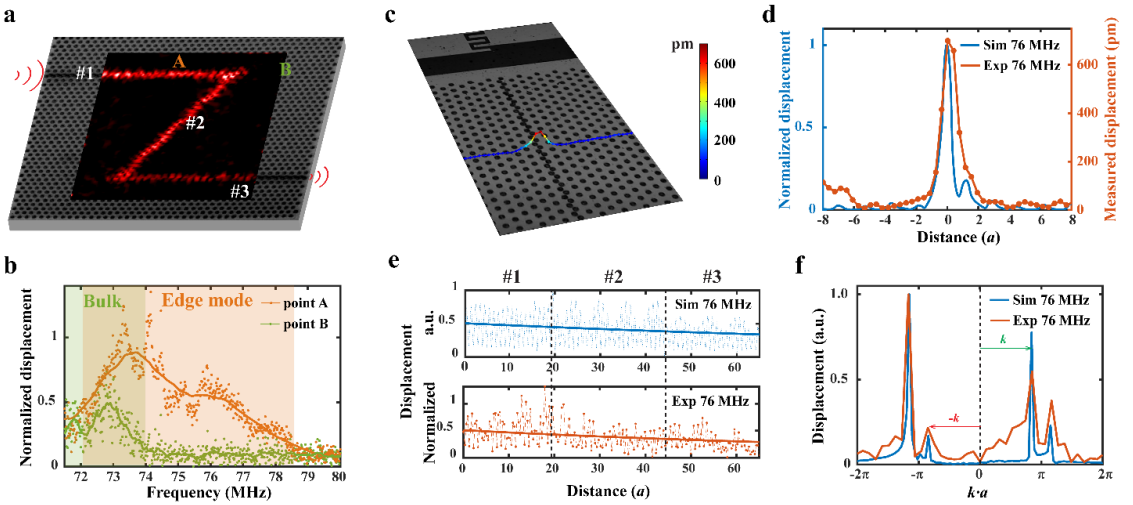

Figure 4.5 Experimental demonstration of highly confined unidirectional SAW in a DLW. (a) Measured u_z field for a Z-shaped SAW DLW. The Z shaped waveguide consists of three segments with $26a$ length for each segment, and two 120° sharp turns. The SAW was excited by a broadband IDT with bandwidth in the range of 35 MHz to 90 MHz. The u_z is imaged by the LDV over a 752.15 μm by 612.80 μm rectangular region. The u_z field shown is at 76 MHz. **(b)** Comparison of u_z for point A on the waveguide and point B away (illustrated in **(a)**) from the waveguide over the frequency range of 71.5 to 80 MHz, respectively. Measured data is plotted in dots, with the moving average shown as a solid line. **(c)** Confinement of the SAW at 76 MHz. **(d)** u_z along the direction perpendicular to the propagation direction at 76 MHz for the simulation and the experiment, respectively. **(e) (top)** Simulated u_z along the waveguide at 76 MHz (dashed line) and fitted exponential decay (solid line). (**bottom**) Measured u_z along the three segments of the waveguide (illustrated in **a**) at 76 MHz (dashed line) and fitted exponential decay (solid line). The u_z in **b** and **(e)** are normalized by the distance between the IDT and the entrance port of the waveguide. **(f)** Spatial FFT at 76 MHz comparing the simulation with experiment.

Tightly confined SAW guiding along the proposed DLW, in close accord with the computational simulations of **Figs. 4.3 and 4.4**, was experimentally demonstrated in our

device, illustrated in **Fig. 4.5**. The out-of-plane displacement field u_z was measured by a laser Doppler vibrometer (LDV, UHF-120, Polytec). To eliminate possible spurious mode interference from bulk acoustic waves, the back side of the $LiNbO_3$ was roughened. We designed a chirped IDT with a wide bandwidth from 35 MHz to 90 MHz (see **Methods**) to excite the SAW and observed unidirectional edge states propagating through a Z-shaped interface with two 120-degree sharp turns. **Fig. 4.5(a)** depicts the measured out-of-plane SAW displacement field u_z at 76 MHz where a clear surface wave confinement and transport along the DLW is shown. To determine the bandwidth of the edge mode, we compared two points on the device: point **A** on the waveguide and point **B** in the bulk of the triangular crystal, as shown in **Fig. 4.5(a)**, and their u_z vs. frequency, as shown in **Fig. 4.5(b)**. Here, the u_z was normalized by the displacement directly in front of the source IDT. It can be clearly seen that away from the waveguide (point **B**) the u_z goes to nearly zero after 74 MHz, which indicates a SAW bandgap for the triangular lattice above 74 MHz. On the other hand, the displacement profile of point A on the waveguide shows a clear bandwidth up to 78.5 MHz, which proves that our edge mode exists in the bulk band of the SAW from 74 MHz to 78.5 MHz. We have also observed guided SAW below the bulk band from 72 MHz to 74 MHz (see subsection 4.8.5), as confirmed through **Fig. 4.3(a)**. However, these modes coexist with bulk SAW modes in the background and are less confined. At higher frequencies we note a reduced bandwidth than in simulation, owing to the band edges resulting in flat dispersion, thereby increasing their attenuation, and complicating direct observation. To show the confinement of the edge mode in the SAW bandgap, we measured the u_z in the direction perpendicular to the waveguide, as shown in **Fig. 4.5(c)**. **Fig. 4.5(d)** shows that the measured u_z agrees closely with

simulation at 76 MHz, and a 3dB decay within $0.509a$ is observed, implying that the mode is highly confined to the interface.

A decay in the displacement amplitude along the waveguide was observed in both the simulation and the measurement (see subsection 4.8.6). The measured u_z amplitude for the three segments of the Z-shaped waveguide at 76 MHz is shown in the bottom figure of **Fig. 4.5(e)**, with the simulation result shown in the top figure of **Fig. 4.5(e)**. Assuming a very small reflection at each sharp turn (as justified by the discussion in the next paragraph) and fit the decay of the u_z to be of the form of an exponential decay $Ae^{-\alpha d}$, where *A* is the amplitude, α is the decay coefficient, and *d* is the distance the SAW travels along the waveguide, we find $\alpha_{sim} = 0.00620/a$, and $\alpha_{exp} = 0.00862/a$, with the fitted exponential curves plotted in solid lines in **Fig. 4.5(e)**. This indicates 3dB loss at a distance of ~56a from the entrance port in the simulation, in comparison to ~40a in the measurement.

We quantitively studied the reflection of the SAW and demonstrated there is indeed little reflection at the 120-degree sharp turns. We took the spatial FFT of the u_z along the first segment of the waveguide before the first sharp turn and looked at the wavevectors, as shown in **Fig. 4.5(f)**. The wavenumber components in **Fig. 4.5(f)** show a finite value for the negative wavenumber $-k$ within the first BZ (-π to π) for both the simulation and the experimental results, indicating there is a small reflection at the 120-degree bends. A higher order component for the same wavevector outside of the first BZ is also observed. We took the average ratio of the displacement component for the k and the $-k$: $r = \frac{u_{z,-k}}{u_{z,k}}$ in the 1st and 2nd BZ as the reflection coefficient of the SAW and obtained $r_{sim} = 0.224$ for the simulation, and $r_{exp} = 0.385$ for the measurement. We consider the 3 segments of the Z-

shaped waveguide of same acoustic impedance R, so that the SAW energy flux can be expressed as $|u_z|^2/R$. Assuming all the SAW are either reflected or transmitted at the bend, the transmission for the Z-shaped waveguide can be estimated as $t = \sqrt{1-r^2}$, which is t_{sim}= 0.975 for the simulation, and t_{exp}= 0.923, for the measurement. The experimental result indicates that less than 8% of the SAW is reflected in the direction opposite to the incident direction by the two 120-degree bends, proving the directionality of the waveguide. The discrepancies between the simulation and measurement are due to inevitable damping in the sample (e.g., the electroplated copper pillars) and fabrication errors, which are difficult to be precisely simulated.

4.6 Discussion

We have developed a fully integrated on-chip topological SAW unidirectional waveguide, based on defect-line configurations, in a triangular phononic lattice constituted from metallic pillars. Different from spin or valley topological structures, the phononic lattice is trivial with regard to the Berry curvature. Instead, the directionality is maintained by the phase vortex distribution in real space. With half of the total number of pillars needed compared to a VTI ($r_B = 0.8r_A$), the proposed SAW DLW shows better confinement by 5 times in the lateral direction. The confined SAW reduces the number of unit cells needed to construct the waveguide, making it possible to fit many such SAW waveguides on a small chip. Our experiments, in close agreement with simulation results, show successful SAW confinement and routing with small reflection around sharp bends along the propagation path. Our experiments lay the foundation for SAW direction tuning. To enable SAW routing along arbitrary directions, we anticipate the recently found optimal

cut of $LiNbO_3$ substrate [141] can be used in place of the industry-standard 127.68° Y-rotated X-propagating $LiNbO_3$ used in this study. It has been indicated that the proposed DLW is robust in different variations, with the zigzag interface having the widest bandwidth and greatest confinement. Altering the defect boundary shifts the propagation frequency higher or lower and can be potentially used to split frequency components into different directions based on a small difference in the frequency. These results demonstrate the value of this system for further scientific investigations and device development, such as precision removal of cells locally from culture surface [142], multistage cell sorting, high pressure SAW pumping [143] and acoustic streaming [97], would be brought forth through application of our design.

4.7 Methods

4.7.1 Sample Preparation

We fabricated chirped interdigital transducers (IDTs) on 500 μm thick, double-side polished 127.68° Y-rotated X-propagating $LiNbO_3$ (LN, Precision Micro-Optics Inc., Burlington, MA, USA) for surface acoustic wave generation and propagation. Finger widths and finger gaps varying from 26 μm to 11 μm were selected for an operating frequency of 40-90 MHz (from $f = v/\lambda$) to define each IDT, comprised of twenty-five simple finger pairs and linearly distributed gap widths. Standard UV photolithography (using AZ 1512 photoresist and AZ 300MIF developer, MicroChem, Westborough, MA, USA) was used alongside sputter deposition (Denton 18, Denton Vacuum, NJ, USA) and lift-off processes to fabricate the 10 nm Cr / 400 nm Au IDTs and seed layer upon the LN substrate [144,145] . The second layer structure with a thickness of ~15 μm for pillar

growth was fabricated via standard UV laser-written photolithography with alignment to the first layer of the IDT structure (using AZ 12XT-20PL-10 photoresist and AZ 300MIF developer, MicroChem, Westborough, MA, USA) (MLA 150, Heidelberg Instruments, Heidelberg, Germany). A dicing saw (Disco Automatic Dicing Saw 3220, Disco, Tokyo, Japan) was used to cut the entire wafer into small size SAW device chips. Then 6.2 μm Cu (copper) was electrochemically deposited on the exposed Au seed layer in an electrolyte environment. The second layer of the photoresist pattern was latter removed by acetone.

4.7.2 Experimental Measurement

A sinusoidal electric field with input voltage of 0.1 V and sweeping frequency from 35-95 MHz was applied to the IDT to excite a broadband input signal into the entrance port of the SAW waveguide using a signal generator (WF1967 multifunction generator, NF Corporation, Yokohama, Japan) and amplifier (ZHL-1-2W-S+, Mini-Circuits, Brooklyn, NY, USA). The actual voltage, current, and power across the device were measured using a digital storage oscilloscope (InfiniiVision 2000 X-Series, Keysight Technologies, Santa Rosa, CA). The source IDT is of the aperture of $1.44a$ (overlapping width) and is $5.2a$ away from the entrance port of the waveguide. To eliminate reflections at the boundaries of the device, a SAW absorber (Dragon Skin 10 Medium, Smooth-On, Inc., Macungie, PA, USA) is placed around the edge of the sample. The backside of the $LiNbO_3$ wafer is roughened to absorb possible reflection of the bulk acoustic wave at the bottom of the wafer. The out-of-plane displacement magnitude and phase fields are captured by a laser Doppler vibrometer (LDV, UHF–120, Polytec, Waldbronn, Germany). The data presented is the average after 10 measurements from the LDV.

4.7.3 Numerical Simulation

The eigen-mode and the driven-mode simulations were implemented using the commercial software COMSOL Multiphysics with the Acoustic (Acoustic-Solid Interaction) and Electrostatics modules, based on the finite element method. Floquet periodic boundaries were assigned for unit cell and supercell band diagram calculations, while the low-reflection boundary was imposed on the outer boundaries for the frequency domain driven-mode studies. A fixed boundary is always applied at the bottom of the $LiNbO_3$ substrate. On the band diagrams for the unit cells, the SAW modes can be distinguished under the sound cone, which is formed by the slowest bulk mode dispersion. In the driven mode simulation, we excite the SAW by applying a sinusoidal edge load or a point load on the substrate. For the material properties, we used the z-cut $LiNbO_3$ parameters with a rotated coordinate system to get the properties for the 127.68^o -degree Y/X-cut $LiNbO_3$ wafers. The elastic parameters of the Cu pillars used in the calculations are density $\rho_{Cu} = 8960\,\mathrm{kg\,m^{-3}}$, Young's modulus $E_{Ni} = 70$ GPa and Poisson's ratio $\nu_{Cu}=0.34$. Note that the Young's modulus is smaller than the conventional Young's modulus for Cu, due to our specific plating process. It was also found in the literature that Young's modulus can be sensitive to plating conditions [146].

For the Berry curvature calculation [30], the complex out-of-plane displacement with magnitude and phase information in the real-space domain is exported from COMSOL simulations for each wavevector for the integration.

4.8 Supplementary Information

4.8.1 SAW Supported by Resonant Modes of Pillars

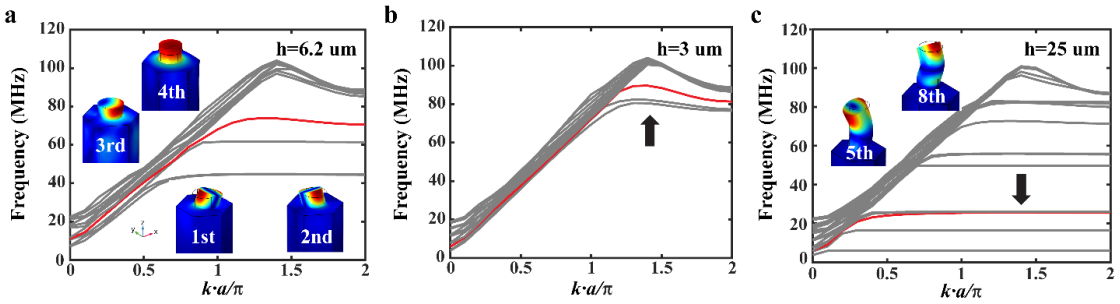

Figure 4.6 Band diagram for unit cells with different pillar heights. (a) pillar with h=6.2 um. The inset shows the eigen modes of the 4 lowest SAW bands at K point. **(b)** pillar with h=3 um, and **(c)** pillar with h=25 um. The insets show the eigen modes corresponds to 5th and 8th bands.

From the inset of **Fig. 4.6(a)** we can see that the eigen modes of these SAW bands correspond to bending, expansion (pure in-plane motion) and extrusion/compression (pure out-of-plane motion) of the copper pillar. The 1st and 2nd SAW bands correspond to 1st order bending of the pillars in x/y direction. The 3rd band is for pure xy-plane expansion, as also discussed and demonstrated by previous sections. The 4th band represents a pure out-of-plane extrusion/compression, which is also the mode of interest in this paper. When the pillar becomes shorter, these resonances are lifted to a higher frequency, pushing the SAW bands into the bulk bands, as shown by **Fig. 4.6(b)**. In the case of h=3um, there is no complete SAW band gap. Longer pillar on the hand would has lower resonant frequencies, such that more SAW bands would appear, as shown in **Fig. 4.6(c)**. Higher order resonant modes such as 2nd order bending and 3rd order banding modes appears in the SAW modes for h=25um, as indicated by the inset. However, the out-of-plane mode of interest is now overlapping with other SAW modes, making it hard to observe the SAW edge states.

4.8.2 Vanishing of Berry Curvature

In **Fig. 4.2** we show a numerical calculation of the Berry curvature for the SAW unit cell that shows a zero Berry curvature. Here we prove that this is a requirement of the system based purely upon symmetry [147].

For the z-directed displacement field Bloch modes $|u_z\rangle$ in the Brillouin zone, we can define the Berry connection

$$\boldsymbol{A} = -i\langle u_z|\partial_k|u_z\rangle, \tag{4.1}$$

and Berry curvature

$$F(\boldsymbol{k}) = \nabla_k \times \boldsymbol{A}. \tag{4.2}$$

Our system maintains the bosonic time reversal symmetry operator $\mathcal{T}: \boldsymbol{k} \rightarrow -\boldsymbol{k}$. Therefore, the curvature $F(\boldsymbol{k})$ is required to be an odd function of $\boldsymbol{k}$,

$$F(-\boldsymbol{k}) = -F(\boldsymbol{k}). \tag{4.3}$$

Note that this holds for $\mathcal{T}$ obeying the relation $\mathcal{T}^2 = +1$, so the bosonic nature does not change the requirement. Likewise, in the presence of spatial inversion symmetry $\mathcal{I}: \boldsymbol{r} \rightarrow -\boldsymbol{r}, \boldsymbol{k} \rightarrow -\boldsymbol{k}$ (in our system this is enforced by the C_{6v} symmetry), the curvature is required to be an even function of $\boldsymbol{k}$,

$$F(-\boldsymbol{k}) = F(\boldsymbol{k}). \tag{4.4}$$

Combining these two conditions from both $\mathcal{T}$ and $\mathcal{I}$, we find that the curvature must be both even and odd for all $\boldsymbol{k}$, which is true only for $F(\boldsymbol{k}) = 0$. So, in our system the curvature is required to be zero everywhere, provided it maintains time reversal and spatial inversion symmetry. Note, however, that the above proof is valid only for isolated bands, where the form of the Berry connection $\boldsymbol{A}$ takes the form shown. If there are degeneracies present, the equation must be modified to the non-Abelian formulation, which implies that

at locations of degeneracy the Berry curvature may be non-zero but will average to zero numerically [139]. If the fully non-Abelian formulation is taken, however, the curvature will again be seen to be identically zero.

4.8.3 Symmetry Indicator Analysis of the Phononic Modes

The existence of the defect line mode can be seen visually from the behavior of the phase vortices: when the lattice is terminated on a finite edge with phase vortices rotating in the same direction on either side of the interface, a unidirectional mode can appear. However, such behavior can be further understood by the application of symmetry indicators [34].Here we first briefly cover the theory behind such methods and provide a simplified description of how they can be computed from simulated results, then show the result for our case of the SAW structure presented in the previous sections.

Symmetry indicators provide a means of analyzing the topological behavior of periodic systems given the relevant rotational symmetry of the base unit cell. For a system with unit cell possessing C_n rotational symmetry the symmetry indicator is defined by the set of numbers $\chi^{(n)}$ that count the number of rotation eigenvalues the system has at high symmetry points, minus those at the Γ point. For the full details on which values are to be chosen, and the reasoning for the various forms, we direct the reader to reference papers [34,148]. The specific forms for $\chi^{(n)}$ in a spin-1 system can be given as

$$\chi^{(6)} = \left(\left[M_1^{(2)}\right], \left[K_1^{(3)}\right]\right), \tag{4.5}$$

$$\chi^{(4)} = \left(\left[K_1^{(2)}\right], \left[M_1^{(4)}\right], \left[M_2^{(4)}\right]\right), \tag{4.6}$$

$$\chi^{(3)} = \left(\left[K_1^{(3)}\right], \left[K_2^{(3)}\right]\right), \tag{4.7}$$

$$\text{and } \chi^{(2)} = \left(\left[X_1^{(2)}\right], \left[Y_1^{(2)}\right], \left[M_1^{(2)}\right]\right). \tag{4.8}$$

Where $\left[\Pi_p^{(n)}\right] \equiv \#\Pi_p^{(n)} - \#\Gamma_p^{(n)}$ and $\#\Pi_p^{(n)}$ is the number of energy bands below a given bandgap with rotation eigenvalue $\Pi_p^{(n)} = e^{2\pi i(p-1)/n}, for\ p = 1,2, \ldots n.$

Computationally, for an arbitrary periodic system the approach can be broken down into the following steps [Liu 2021]:

1. Simulate the phase profile of the unit cell at the relevant high symmetry points of the Brillouin zone (e.g., Γ, K, M, X, etc.).
2. Multiply the spatially variant phase profile by the scalar values of the eigenvalues of the relevant rotation operators (e.g., C_6, C_3, etc.), receiving one altered phase profile from each.
3. Determine which eigenvalue gives the same result as that found by simply rotating the original phase profile by the same rotation. This determines the eigenvalue corresponding to that rotation operator applied to the unit cell.
4. Using the formulas for the desired symmetry indicators given above, sum all such eigenvalues to determine the topological invariant for the system.

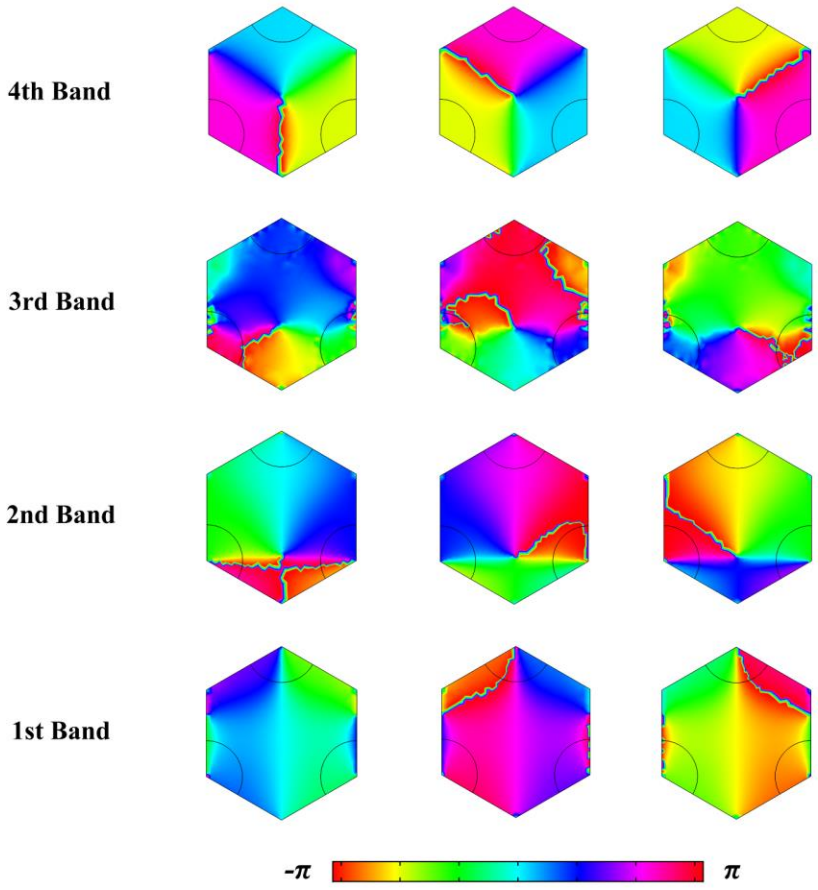

Figure 4.7 Phase plots at K for the eigen modes for the first four bands. Unit cell choice and resulting simulated z-directed phase profiles for the SAW structure, used in the symmetry indicator analysis. The first column are the unaltered phase profiles, the second are those with the first nontrivial eigenvalue applied, and the third are for the second nontrivial eigenvalue applied. Note that the displacement magnitude for the third band is substantially lower, indicating it is likely not a pure z-directed mode and can be ignored.

The choice of which to calculate is set by the unit cell definition, as this sets the behavior at a finite edge. In our SAW system, the unit cell can be chosen to be a single pillar in the center of a hexagonal unit cell, resulting in C_6 rotational symmetry. Such a choice then requires $\chi^{(6)}$, which calculate to be $\chi^{(6)} = (0,0)$ for our system and given bandgap. However, when the unit cell definition is shifted to the one shown in **Fig. 4.7**, with 3 partial corners, the cell becomes C_3, therefore requiring $\chi^{(3)}$. The phase profiles of our structure for the K point for this definition of unit cell are shown in **Fig. 4.7**. The first

two bands are degenerate and consequently have distorted phase vortices at lower-symmetry points (see Supplementary Sec. 4). Likewise, the 3rd band is not a pure z-directed SAW mode (see Supplementary Sec. 4), and so does not influence the calculation here. However, the 4th mode, which is the one below our operating bandgap, displays the expected phase vortex-behavior shown in the previous sections. From the plots, we can see that the C_3 rotation eigenvalue is $e^{2\pi i(2/3)}$, which (when we subtract the eigenvalues at Γ, which are all unity here) results in $\chi^{(3)} = (-1,0)$. If we rotate the unit cell by C_2 (thereby turning from a downward-pointing triangle to an upward-pointing triangle) and repeat this analysis, we find $\chi^{(3)} = (-1,+1)$.

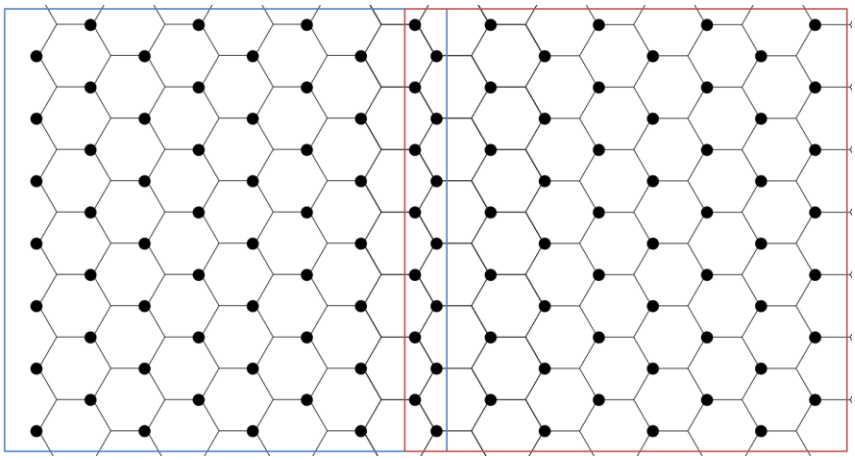

Figure 4.8 Zigzag defect line in a triangular lattice. Illustration of the splitting of the unit cells into 2 C_3 unit cells on either side of the finite interface. The blue and red rectangles show the two sides, with the overlapping region containing the interface of the otherwise infinite lattice.

The above analysis shows that the shifted version of the unit cell possesses a non-trivial topological behavior, though one protected here by the rotational symmetry of the system as well as the finite behavior. We stress here that the Berry curvature is still identically zero, as it is a gauge invariant quantity and is therefore unaffected by the spatial translation of the unit cell. The resulting shifted unit cell merely alters the behavior at finite

edges, which is not captured by the pure Berry curvature description. The existence of the edge mode in this case can be understood by the flipping of the signs of $\chi^{(3)}$ on either side of the interface, which, when tiled with a uniform hexagonal lattice causes the two C_2-related unit cells to appear (see **Fig. 4.8**).

4.8.4 Irreps of Phononic Modes

For the symmetry indicator calculations above, certain features of the z-directed phase distribution appeared to disobey the requirements of the various eigenvalues. Namely, the 1st -3rd modes do not appear to transform as C_3. Here we show via direct calculation the origin of this and show how they do not alter the conclusion using a group theoretic analysis of the modes themselves.

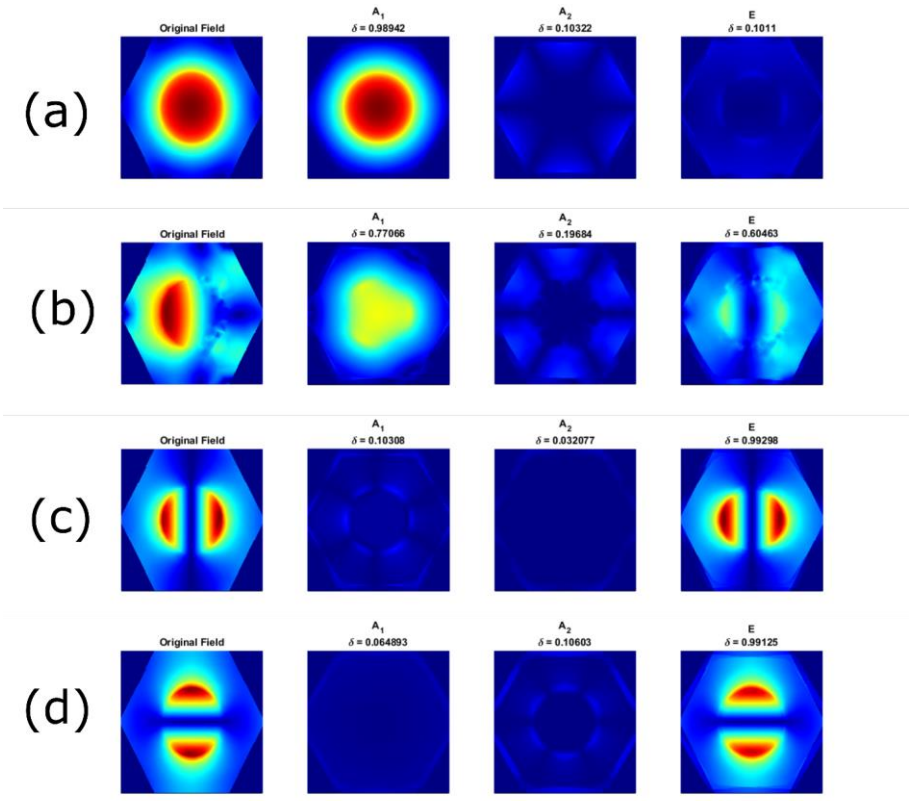

Figure 4.9 Projected eigenmodes of the first 4 bands of the SAW device onto the irreps of K. (a)-(d) are for the 1st-4th modes, respectively.

In **Fig. 4.9**, we show the results of applying the character projection technique [Hergert 2018] onto the complex z-directed displacement fields for the first 4 bands at the K point. This allows us to classify each mode into the irreducible representations (irreps) of the relevant little group, which for the K point is C_{3v}. Each field shows the projected fields on each irrep, where the correct irrep for each can be visually checked by comparison to the unaltered field. By construction, each projected field will be orthogonal to each other, in the sense that each discretized field point will be approximately zero when the irrep of the field does not match that of the projector used. If they do match, the resulting projected fields will be approximately the same (with small differences occurring at the edges due to numerical artifacts). In addition, to better quantify this we also show the computed Frobenius norm of the field (denoted δ), which will be approximately unity for the correct irrep, and approximately zero for all others.

From this, we can immediately see that the first two modes are degenerate, which is not clear from the band structure. Likewise, we see that the 3rd band is not uniquely characterized by any of the three irreps, signifying that the mode is not a pure z-directed eigenmode. This is further corroborated by the field magnitude, which is itself ~3 orders of magnitude smaller than the others. We can thus ignore this mode from the resulting calculations, as it does not factor into the 2D symmetry indicator analysis.

4.8.5 Field Scans at Different Frequencies

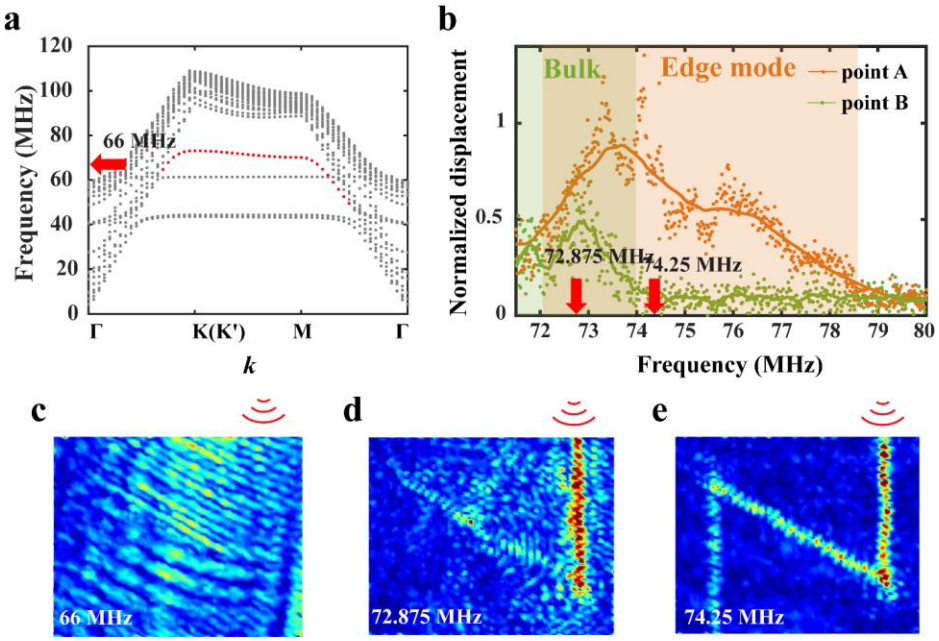

Figure 4.10 Measured u_z fields at different frequencies. (a) unit cell band diagram (Fig. 2f). **(b)** Displacement vs. frequency for a point on the waveguide (point A) and a point away from the waveguide (point B) (**Fig. 4.5(b)**). **(c)** Measured u_z at 66 MHz. **(d)** Measured u_z at 72.875 MHz. **(e)** Measured u_z at 74.25 MHz. These 3 frequencies are marked in a and b by red arrows.

The measured u_z fields for frequencies correspond SAW bulk band, eigen mode within SAW bulk band, and eigenmode in SAW bandgap are plotted in **Fig. 4.10 (c), (d)** and **(e)**. respectively. For an excitation with a frequency in SAW bulk bands, SAW would propagate everywhere on the surface of the structure, as shown in **Fig. 4.10(c)**. When the frequency corresponds to the edge mode falls in the SAW bandgap, only the SAW edge mode along the waveguide will be excited, as shown in **Fig. 4.10(e)**. However, there is an overlap between the frequency range of the SAW bulk bands and SAW edge states, as shown by **Fig. 4.10(b)** (**Fig. 4.5(b)** in the section 4.5). In this frequency range, the SAW edge states would be excited together with bulk SAW, as indicated by **Fig. 4.10(d)**.

4.8.6 Comparison between Confinement and Loss between Defect-line Waveguide and Valley TIs

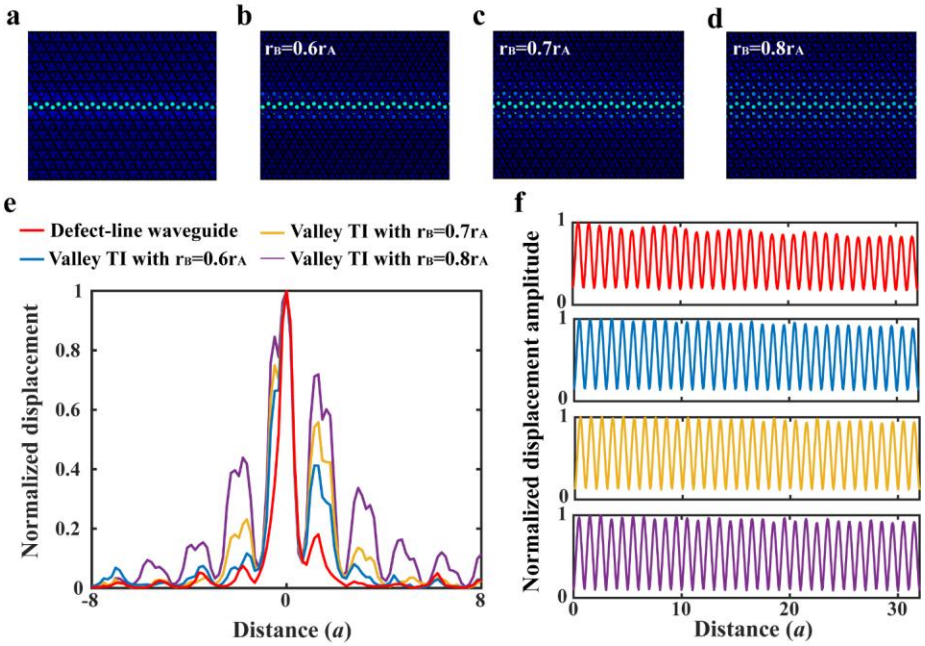

Figure 4.11 Confinement and decay for proposed defect-line waveguide and Valley TIs. (a) u_z for defect-line waveguide. **(b)** u_z for Valley TI with $r_B = 0.6r_A$. **(c)** u_z for Valley TI with $r_B = 0.7r_A$. **(d)** u_z for Valley TI with $r_B = 0.8r_A$. **(e)** u_z in the direction perpendicular to the direction of propagation. f. u_z along the direction of propagation.

The confinement and loss of the proposed waveguide and the valley TIs are illustrated in **Fig. 4.11**. Our proposed waveguide shows a better confinement compared to the valley TIs, as shown in **Fig. 4.11(e)**, but is more lossy along the waveguide compared to the valley TIs, as shown in **Fig. 4.11(f)**. We also noticed that the more contrast between the pillars in the Valley TI, the more confined the SAW is, but the more lossy it becomes.

This chapter is based on *On-chip unidirectional waveguiding for surface acoustic waves along a defect line in a triangular lattice* by Y. Zhou, N. Zhang, D. J. Bisharat, R.

J. Davis, Z. Zhang, J. Friend, P. R Bandaru and D. F Sievenpiper, *Under Submission*. The dissertation author was the primary author of this material.

Chapter 5

Helical Phononic Modes Induced by a Screw Dislocation

5.1 Introduction

Previous chapters have been focusing on 2D implementations of phononic topological waveguides, which also naturally brings up the question on how to build a topological waveguide in a 3D structure. The focus of this chapter will be on creating a 1D topological waveguide in a 3D phononic crystal.

Defects are common within all forms of solid-state matter, and only recently has it been shown that some have technologically beneficial qualities. The most promising of these are those with topological features, which enforce the existence of modes that are immune to a wide range of scattering phenomena. Fermionic 3D topological insulators have been shown to have 1D edge states within screw discontinuities, which are supported by a weak topological index and a Burgers vector [23], or by partial dislocations at fault lines [149]. Researchers have often used engineered photonic or phononic structures to probe such defects, with recent efforts in acoustics demonstrating robust edge states from Weyl crystals in coupled resonators. However, in all such cases, the initial starting point is always a topological material, 2D or 3D, and 1D edge states are induced within the bandgap via an interplay of the defect and the preexisting topology. Here we show that such modes

can exist in a 3D phononic crystal without spin-orbit coupling that is initially trivial, where robust 1D edge states are induced purely by a screw dislocation. Our results reveal that unidirectional edge states can exist via structural helicity, without the requirements of other systems.

Many attempts have been made in realizing topological phases in 3D phononic structures. For example, topologically protected 2D surface states associated to Weyl points (3D counterpart of Dirac point) are proposed and experimentally demonstrated in phononic Weyl crystals [150–154]. Higher order phononic topological insulators have also been proposed, where 0D topological corner states are realized [155]. However, realizing 1D topological modes [156] in such systems is still challenging.

Topological defects [23–26,157–159], on the other hand, are shown to be associated with one-dimensional fermionic excitations in a topological insulator. This idea has been applied to construct 1D topological waveguide in 3D photonic and phononic systems as well. However, existing designs are all based on creating a defect line in a 3D topological insulator, resulting in complicated 3D structures.

We have showed in Chapter 4 that a simple 2D topological unidirectional waveguide can be built by shifting part of a triangular phononic lattice to form a defect line. Similar phenomena are also found in 2D photonic crystals. Can analogous phenomena occur in a 3D phononic crystal, if we are able to create a 3D shift in it? This question will be answered by the sections follow.

5.2 Helical Phononic Modes in a hcp Lattice

We start with a 3D phononic crystal with a large band gap – a hexagonal close packed (hcp) crystal made with solid steel balls embedded in epoxy background material. Previous research has shown that 3D phononic band gap can be formed in such structure, which is also evidenced by our bandgap simulation in Fig. 5.1.

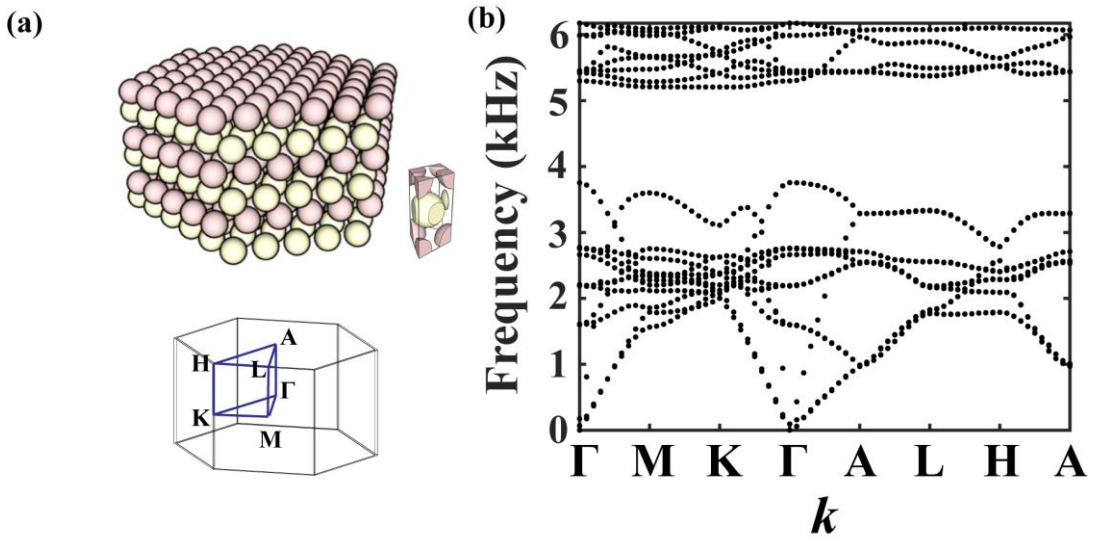

Figure 5.1 Hcp phononic crystal with a large band gap. (a) Hcp phononic crystal made with steel metal balls in an epoxy background. The two colors indicate the AB stacking of the hcp crystal. (b) A 3D band gap in the hcp crystal.

Then we introduce a screw dislocation with burger's vector $b = c$ to the hcp lattice, where c being the lattice constant in the z direction, as shown by **Fig. 5.2(a),** and calculate the band diagram for the supercell, as shown by **Fig. 5.2(b)**. A pair of linear dispersion with opposite group velocities are observed in the band diagram. And their eigen displacement fields in **Fig. 5.2(c)** clearly shows a rotational behavior with opposite chirality. Other modes in the band gap corresponds to artificial boundary or corner states that caused by boundary condition settings in the eigenmode simulation and are not important in our discussion here.

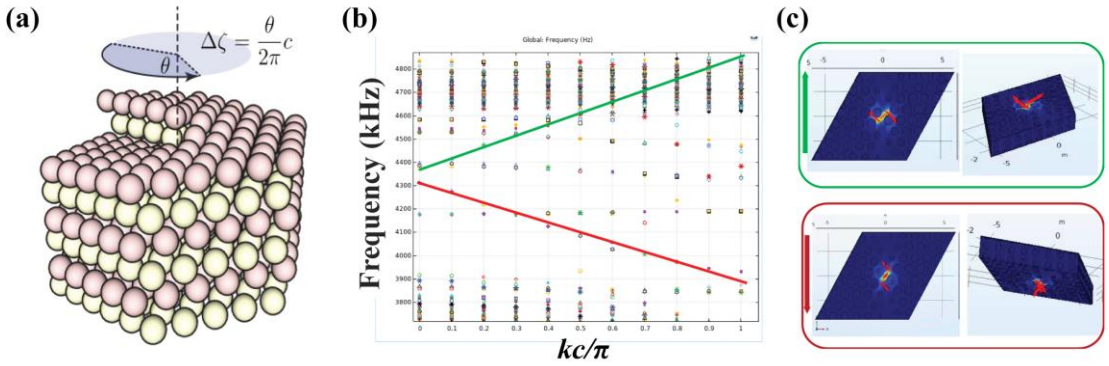

Figure 5.2 Helical phononic modes induced by the screw dislocation. (a) Hcp phononic crystal made with a screw dislocation. (b) Counter-propagating helical modes in the phononic band gap. (c) Eigen displacement fields corresponds to the helical modes.

5.3 Directionality of the Helical Modes

To prove the directionality of the modes we found in Section 5.2, we constructed a waveguide with two screw dislocations of opposite helicity connected to each other, as shown in **Fig. 5.3(a)**. A point source with a frequency within the band gap is used to excite the wave at the bottom of the waveguide, and a perfect matching layer is attached to the top to eliminate reflection. The displacement along the dislocation waveguide is plotted in **Fig. 5.3(b)**. Comparing the x and y displacement in the first screw, a 90-degree phase difference is observed, a clear suggestion that the displacement field at the dislocation is rotating along the waveguide. Also, we can see that little of the phononic wave in the first screw passes into the second screw with opposite helicity, which indicate that wave with one kind of helicity would keep its helicity while propagating: an indication of one-way propagation.

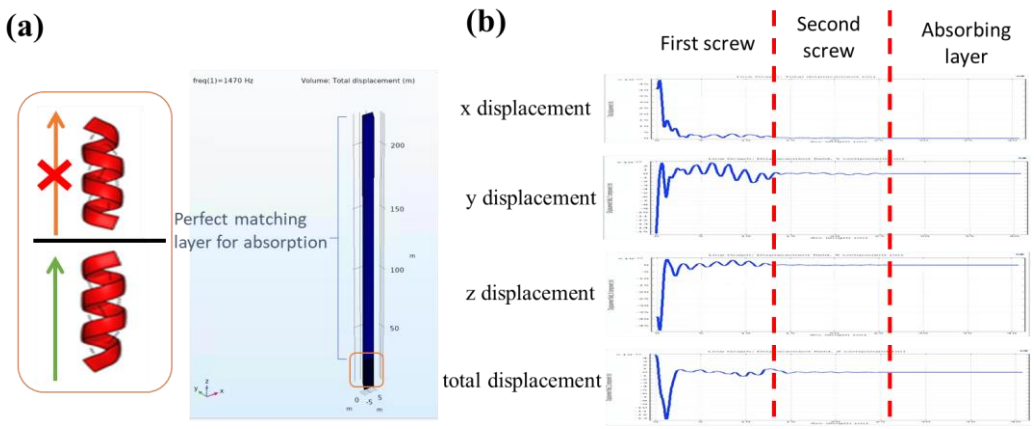

Figure 5.3 Unidirectional helical phononic modes. (a) Waveguide with two screw dislocations with opposite helicity connected. (b) Displacement along the waveguide in (a).

The HCP crystal structure used as the starting material can be modeled via a general spinless Hamiltonian H with time-reversal symmetry following the symmetries of the space group (e.g., #194; point group D_{6h}). We note that for the phononic crystal studied here, such a Hamiltonian must necessarily fall into the AI Cartan class [160], as the time-reversal operator T has the property T^2 = +1. From the topological defect classification [161], we can naively conclude that our system must not possess any 1D edge modes induced by defects. Hence, it is clear that our system goes beyond such a classification (which only considers time-reversal, particle-hole, and chiral symmetries), and instead the crystal structure itself becomes relevant [162]. Therefore, different from the 1D modes mentioned in the introduction, the unidirectional modes we observed here is from a pure trivial 3D crystal.

5.4 Measurement Results

We prepared samples of both a fully trivial HCP crystal and one with the same screw dislocation studied in simulation. The background structures were 3D printed by the material called Tango Black Plus layer by layer, and the solid carbon steel metal balls were popped into the printed matrix to assemble the samples.

The measurement of the pressure field displacement amplitude shown in **Fig. 5.4** was performed using an automated translation stage (modified 3D printer). The excitation was a directional speaker, which was placed at the center of the sample for all measurements. The receiver used was a microphone which was inserted into a metal tube 2 cm long to improve spatial resolution. An averaging of 16 samples was used for each datapoint, and a lock-in amplifier was used, with an internally generated sine wave as the input to the speaker. To reduce external noise sources, all measurements were performed inside an anechoic chamber. For the spatial scans shown in **Fig. 5. 4(c)** and **(d)**, the 2D stage moved the microphone 0.5 cm above the top surface of the sample. The measurement was repeated under the same conditions for the nontrivial sample (**Fig. 5.4(c)**) and the trivial bulk (**Fig. 5.4(d))**. The measurement setup is shown in **Fig. 5.4(a)**.

For the transmission spectra of the nontrivial sample shown in **Fig. 5.4(b)** (in red), we placed the same measurement setup with the microphone at the geometric center of the sample, at the vertex of the screw dislocation and took an average of 16 samples for each frequency. We repeated this with the microphone placed at the corner of the nontrivial sample, and again with the trivial bulk sample with the microphone at the geometric center. All results were then normalized by the measured free-space transmission (with microphone directly connected to the speaker), and each peak is then normalized to their respective maxima.

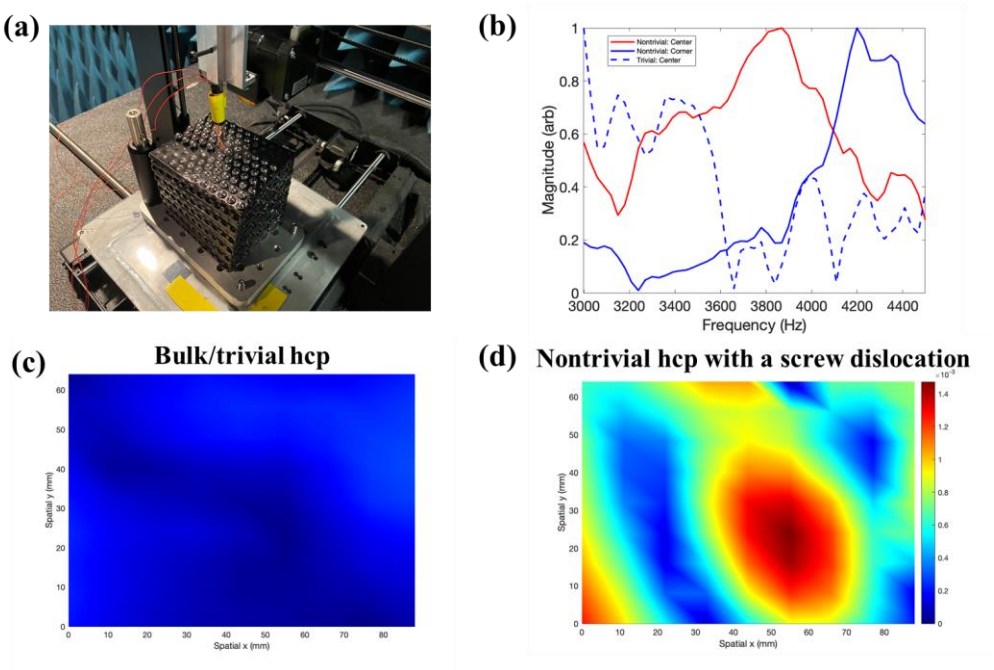

Figure 5.4 Measurement of the screw-dislocation waveguide. (a) Measurement setup. (b) Displacement amplitude vs. frequency at the center of the nontrivial sample compared to that at the center of the trivial sample and that at the corner at the nontrivial sample. (c) and (d) are the field scan on the top of the trivial and nontrivial samples at frequencies in the bandgap, respectively.

From **Fig. 5.4 (b)**, **(c)** and **(d)** we see that nontrivial sample shows a mode confined at the screw dislocation where the trivial clearly shows a bandgap. The measurement results align well with simulation results in Sections 5.2 and 5.3.

5.5 Conclusions

This chapter presents a 1D topological waveguide in a 3D phononic crystal, induced by a screw dislocation. Even though the 3D phononic crystal studied here is a simple conventional hcp crystal rather than a complicated 3D topological insulator, we still proved from numerical simulations the directionality of the modes confined at the screw dislocation. Our measurement results further verify the existence of these modes. This

waveguide can be potentially used for vibration damping and unidirectional sound propagation for privacy protection.

This chapter is based on *Helical phononic modes induced by a screw dislocation* by Y. Zhou, R. Davis, L. Chen, E. Wen, P. R. Bandaru and D. F. Sievenpiper, *In preparation*. The dissertation author was the primary author of this material.

Chapter 6

Discussion

6.1 Summary

This thesis presents an investigation into topological waveguides, in 2D and 3D phononic structures, from both theoretical and experimental perspectives. Our modeling, computations and experiments have deep scientific implications for the rapidly expanding field of topological materials, which has extended from electronic to phononic systems.

A 2D theoretical model is studied in Chapter 2, where a topological waveguide is built in a spring-mass phononic system. This work provides many physical insights, related to topological interactions and pointed from the point of view of a mass-spring system. The idea is analogous to the quantum spin Hall effect in electronic system. Since phonons are spin-1, the pseudospins in are introduced by hybridizing phonons at the same energy level, which is achieved by the zone-folding technique. To open a non-trivial energy band gap and form topological edge states, we tune the lattice symmetry varying the inter- and intra-cell couplings while maintaining the C_6 symmetry of the unit cell. Topological edge states propagate unidirectionally are found in such systems, that can turn sharp corners. However, the robustness of these modes towards lattice defects is debatable, as they are induced by tuning the lattice symmetry in the system.

To construct a robust 2D waveguide, in Chapter 3 we introduce frequency resonators – Helmholtz resonators to the phononic system. The waveguide constructed is

robust over frequency and location disorders in the lattice and shows great confinement. It shows potential of confining phononic wave into very small region.

Based on the theoretical studies on topological physics and phononic waveguiding in the previous two chapters, we build and measure a real 2D topological waveguide in Chapter 4, for surface acoustic waves. The waveguide built is a defect line in a triangular phononic lattice, which different from conventional 2D topological waveguides, has zero Berry curvature and is characterized by the symmetry indicator instead. This design is simple and effective and inspires our work on the defect-line unidirectional waveguide in 3D phononic crystal, which is discussed in Chapter 5.

Chapter 5 presents a unidirectional waveguide in a 3D crystal, using a similar idea to Chapter 4, by creating a defect line – a screw dislocation to the crystal. The existence have the modes are proved by both simulations and experiments, suggesting a novel way of guiding phonons unidirectionally in 3D structures.

6.2 Potential Future Work

The potential future work will be discussed in two aspects: further studies on topological physics in phononics, and potential applications of the topological phononic waveguides.

We discuss in Chapter 2 a model on 2D phononic topological insulator, and in Chapter 3 a phononic waveguide built by resonators. Combining these two models may leads to robust and unidirectional phononic waveguides, which is worth being investigated. The theory behind the 3D defect-line topological waveguide in Chapter 5 also need to be studied further. The 2D defect-line waveguide in Chapter 4 is demonstrated by the

symmetry indicator, and we are expecting to characterize the 3D case in a similar manner. The existence of such defect-line waveguides also motivates us to look for more topological phases in phononic lattices.

For potential applications, the extension to acoustic aspects and conductive heat flow, using our developed methods and designs would be very attractive. For example, the 2D unidirectional waveguides can be adopted for surface acoustic wave applications, where highly directional and confined acoustic energy propagation is needed. Since heat conduction can also be modeled as phonon movements, the 3D unidirectional waveguide can also be further explored in for building 3D thermal diodes.

Bibliography

[1] F. D. M. Haldane, *Model for a Quantum Hall Effect without Landau Levels: Condensed-Matter Realization of the "Parity Anomaly,"* Phys. Rev. Lett. **61**, 2015 (1988).

[2] D. J. Thouless, M. Kohmoto, M. P. Nightingale, and M. den Nijs, *Quantized Hall Conductance in a Two-Dimensional Periodic Potential*, Phys. Rev. Lett. **49**, 405 (1982).

[3] M. Z. Hasan and C. L. Kane, *Colloquium : Topological Insulators*, Rev. Mod. Phys. **82**, 3045 (2010).

[4] J. E. Moore, *The Birth of Topological Insulators*, Nature **464**, 194 (2010).

[5] L. Lu, J. D. Joannopoulos, and M. Soljačić, *Topological Photonics*, Nat. Photonics **8**, 821 (2014).

[6] T. Ozawa, H. M. Price, A. Amo, N. Goldman, M. Hafezi, L. Lu, M. C. Rechtsman, D. Schuster, J. Simon, O. Zilberberg, and I. Carusotto, *Topological Photonics*, Rev. Mod. Phys. **91**, 015006 (2019).

[7] G. Ma, M. Xiao, and C. T. Chan, *Topological Phases in Acoustic and Mechanical Systems*, Nat. Rev. Phys. **1**, 281 (2019).

[8] X. Zhang, M. Xiao, Y. Cheng, M. H. Lu, and J. Christensen, *Topological Sound*, Commun. Phys. **1**, 1 (2018).

[9] S. D. Huber, *Topological Mechanics*, Nat. Phys. **12**, 621 (2016).

[10] Y. Liu, X. Chen, and Y. Xu, *Topological Phononics: From Fundamental Models to Real Materials*, Adv. Funct. Mater. **30**, (2020).

[11] L. M. Nash, D. Kleckner, A. Read, V. Vitelli, A. M. Turner, and W. T. M. Irvine, *Topological Mechanics of Gyroscopic Metamaterials*, Proc. Natl. Acad. Sci. **112**, 14495 (2015).

[12] P. Wang, L. Lu, and K. Bertoldi, *Topological Phononic Crystals with One-Way Elastic Edge Waves*, Phys. Rev. Lett. **115**, 104302 (2015).

[13] Z. Zhang, Q. Wei, Y. Cheng, T. Zhang, D. Wu, and X. Liu, *Topological Creation of Acoustic Pseudospin Multipoles in a Flow-Free Symmetry-Broken Metamaterial Lattice*, Phys. Rev. Lett. **118**, 084303 (2017).

[14] Y. Zhou, P. R. Bandaru, and D. F. Sievenpiper, *Quantum-Spin-Hall Topological Insulator in a Spring-Mass System*, New J. Phys. **20**, 123011 (2018).

[15] S. H. Mousavi, A. B. Khanikaev, and Z. Wang, *Topologically Protected Elastic Waves in Phononic Metamaterials*, Nat. Commun. **6**, 8682 (2015).

[16] R. K. Pal and M. Ruzzene, *Edge Waves in Plates with Resonators: An Elastic Analogue of the Quantum Valley Hall Effect*, New J. Phys. **19**, 025001 (2017).

[17] M. Yan, J. Lu, F. Li, W. Deng, X. Huang, J. Ma, and Z. Liu, *On-Chip Valley Topological Materials for Elastic Wave Manipulation*, Nat. Mater. **17**, 993 (2018).

[18] J. Lu, C. Qiu, M. Ke, and Z. Liu, *Valley Vortex States in Sonic Crystals*, Phys. Rev. Lett. **116**, 093901 (2016).

[19] J. Lu, C. Qiu, W. Deng, X. Huang, F. Li, F. Zhang, S. Chen, and Z. Liu, *Valley Topological Phases in Bilayer Sonic Crystals*, Phys. Rev. Lett. **120**, 116802 (2018).

[20] J. Lu, C. Qiu, L. Ye, X. Fan, M. Ke, F. Zhang, and Z. Liu, *Observation of Topological Valley Transport of Sound in Sonic Crystals*, Nat. Phys. **13**, 369 (2017).

[21] D. J. Bisharat and D. F. Sievenpiper, *Robust Valley Polarized States beyond Topology*, Res. Sq. 1 (2021).

[22] Y. Zhou, N. Zhang, D. J. Bisharat, R. J. Davis, Z. Zhang, J. Friend, P. R. Bandaru, and D. F. Sievenpiper, *On-Chip Unidirectional Waveguiding for Surface Acoustic Waves along a Defect Line in a Triangular Lattice*, (2021).

[23] Y. Ran, Y. Zhang, and A. Vishwanath, *One-Dimensional Topologically Protected Modes in Topological Insulators with Lattice Dislocations*, Nat. Phys. **5**, 298 (2009).

[24] L. Ye, C. Qiu, M. Xiao, T. Li, J. Du, M. Ke, and Z. Liu, *Topological Dislocation Modes in Three-Dimensional Acoustic Topological Insulators*, 1 (2021).

[25] H. Xue, D. Jia, Y. Ge, Y. J. Guan, Q. Wang, S. Q. Yuan, H. X. Sun, Y. D. Chong, and B. Zhang, *Observation of Dislocation-Induced Topological Modes in a Three-Dimensional Acoustic Topological Insulator*, Phys. Rev. Lett. **127**, 214301 (2021).

[26] Q. Wang, Y. Ge, H. xiang Sun, H. Xue, D. Jia, Y. jun Guan, S. qi Yuan, B. Zhang, and Y. D. Chong, *Vortex States in an Acoustic Weyl Crystal with a Topological Lattice Defect*, Nat. Commun. **12**, 1 (2021).

[27] S. Pancharatnam, *Generalized Theory of Interference and Its Applications*, Proc. Indian Acad. Sci. - Sect. A **44**, 398 (1956).

[28] B. Simon, *Holonomy, the Quantum Adiabatic Theorem, and Berry's Phase*, Phys.

Rev. Lett. **51**, 2167 (1983).

[29] M. V. BERRY, *Quantal Phase Factors Accompanying Adiabatic Changes*, Proc. R. Soc. London. A. Math. Phys. Sci. **392**, 45 (1984).

[30] D. Bisharat, R. Davis, Y. Zhou, P. Bandaru, and D. Sievenpiper, *Photonic Topological Insulators: A Beginner's Introduction [Electromagnetic Perspectives]*, IEEE Antennas Propag. Mag. **63**, 112 (2021).

[31] H.-M. Guo and M. Franz, *Topological Insulator on the Kagome Lattice*, Phys. Rev. B **80**, 113102 (2009).

[32] M. Li, D. Zhirihin, M. Gorlach, X. Ni, D. Filonov, A. Slobozhanyuk, A. Alù, and A. B. Khanikaev, *Higher-Order Topological States in Photonic Kagome Crystals with Long-Range Interactions*, Nat. Photonics **14**, 89 (2020).

[33] H. Xue, Y. Yang, F. Gao, Y. Chong, and B. Zhang, *Acoustic Higher-Order Topological Insulator on a Kagome Lattice*, Nat. Mater. **18**, 108 (2019).

[34] W. A. Benalcazar, T. Li, and T. L. Hughes, *Quantization of Fractional Corner Charge in C_n-Symmetric Higher-Order Topological Crystalline Insulators*, Phys. Rev. B **99**, 245151 (2019).

[35] M. Z. Hasan and C. L. Kane, *Colloquium: Topological Insulators*, Rev. Mod. Phys. **82**, 3045 (2010).

[36] X.-L. Qi and S.-C. Zhang, *Topological Insulators and Superconductors*, Rev. Mod. Phys. **83**, 1057 (2011).

[37] Z. Wang, Y. D. Chong, J. D. Joannopoulos, and M. Soljačić, *Reflection-Free One-Way Edge Modes in a Gyromagnetic Photonic Crystal*, Phys. Rev. Lett. **100**, 013905 (2008).

[38] A. B. Khanikaev, S. Hossein Mousavi, W.-K. Tse, M. Kargarian, A. H. MacDonald, and G. Shvets, *Photonic Topological Insulators*, Nat. Mater. **12**, 233 (2013).

[39] T. Ma, A. B. Khanikaev, S. H. Mousavi, and G. Shvets, *Guiding Electromagnetic Waves around Sharp Corners: Topologically Protected Photonic Transport in Metawaveguides*, Phys. Rev. Lett. **114**, 127401 (2015).

[40] T. Ma and G. Shvets, *All-Si Valley-Hall Photonic Topological Insulator*, New J. Phys. **18**, (2016).

[41] L.-H. Wu and X. Hu, *Scheme for Achieving a Topological Photonic Crystal by Using Dielectric Material*, Phys. Rev. Lett. **114**, 223901 (2015).

[42] T. Ma and G. Shvets, *Scattering-Free Edge States between Heterogeneous Photonic*

Topological Insulators, Phys. Rev. B **95**, 1 (2017).

[43] R. Fleury, A. B. Khanikaev, and A. Alù, *Floquet Topological Insulators for Sound*, Nat. Commun. **7**, 1 (2016).

[44] Z. Yang, F. Gao, X. Shi, X. Lin, Z. Gao, Y. Chong, and B. Zhang, *Topological Acoustics*, Phys. Rev. Lett. **114**, 114301 (2015).

[45] B. Z. Xia, T. T. Liu, G. L. Huang, H. Q. Dai, J. R. Jiao, X. G. Zang, D. J. Yu, S. J. Zheng, and J. Liu, *Topological Phononic Insulator with Robust Pseudospin-Dependent Transport*, Phys. Rev. B **96**, 1 (2017).

[46] A. B. Khanikaev, R. Fleury, S. H. Mousavi, and A. Alù, *Topologically Robust Sound Propagation in an Angular-Momentum-Biased Graphene-like Resonator Lattice*, Nat. Commun. **6**, 1 (2015).

[47] Y. Deng, H. Ge, Y. Tian, M. Lu, and Y. Jing, *Observation of Zone Folding Induced Acoustic Topological Insulators and the Role of Spin-Mixing Defects*, Phys. Rev. B **96**, 184305 (2017).

[48] C. Brendel, V. Peano, O. Painter, and F. Marquardt, *Snowflake Phononic Topological Insulator at the Nanoscale*, Phys. Rev. B **97**, 1 (2018).

[49] C. He, X. Ni, H. Ge, X.-C. Sun, Y.-B. Chen, M.-H. Lu, X.-P. Liu, and Y.-F. Chen, *Acoustic Topological Insulator and Robust One-Way Sound Transport*, Nat. Phys. **12**, 1124 (2016).

[50] C. L. Kane and E. J. Mele, *Quantum Spin Hall Effect in Graphene*, Phys. Rev. Lett. **95**, 1 (2005).

[51] B. A. Bernevig and S.-C. Zhang, *Quantum Spin Hall Effect*, **106802**, 1 (2005).

[52] M. Konig, S. Wiedmann, C. Brune, A. Roth, H. Buhmann, L. W. Molenkamp, X.-L. Qi, and S.-C. Zhang, *Quantum Spin Hall Insulator State in HgTe Quantum Wells*, Science (80-.). **318**, 766 (2007).

[53] A. Rycerz, J. Tworzydło, and C. W. J. Beenakker, *Valley Filter and Valley Valve in Graphene*, Nat. Phys. **3**, 172 (2007).

[54] D. Xiao, W. Yao, and Q. Niu, *Valley-Contrasting Physics in Graphene: Magnetic Moment and Topological Transport*, Phys. Rev. Lett. **99**, 1 (2007).

[55] Y. Kim, K. Choi, J. Ihm, and H. Jin, *Topological Domain Walls and Quantum Valley Hall Effects in Silicene*, Phys. Rev. B - Condens. Matter Mater. Phys. **89**, 1 (2014).

[56] Y. T. Wang, P. G. Luan, and S. Zhang, *Coriolis Force Induced Topological Order*

for Classical Mechanical Vibrations, New J. Phys. **17**, 0 (2015).

[57] T. Kariyado and Y. Hatsugai, *Manipulation of Dirac Cones in Mechanical Graphene*, Sci. Rep. **5**, 18107 (2016).

[58] R. Süsstrunk and S. D. Huber, *Observation of Phononic Helical Edge States in a Mechanical Topological Insulator*, Science (80-.). **349**, 47 (2015).

[59] L.-Y. Zheng, G. Theocharis, V. Tournat, and V. Gusev, *Quasitopological Rotational Waves in Mechanical Granular Graphene*, Phys. Rev. B **97**, 060101 (2018).

[60] M. S. Dresselhaus, G. Dresselhaus, and A. Jorio, *Applications of Group Theory to the Physics of Solids*, 1st ed (Springer, New York, 2008).

[61] L.-H. Wu and X. Hu, *Scheme for Achieving a Topological Photonic Crystal by Using Dielectric Material*, Phys. Rev. Lett. **114**, 223901 (2015).

[62] N. F. Johnson and P. M. Hui, *K.p Theory of Photonic Band Structures in Periodic Dielectrics*, J. Phys. Condens. Matter **5**, L355 (1993).

[63] P. Wang, L. Lu, and K. Bertoldi, *Topological Phononic Crystals with One−Way Elastic Edge Waves*, Phys. Rev. Lett. **115**, 104302 (2015).

[64] T. Fukui, Y. Hatsugai, and H. Suzuki, *Chern Numbers in Discretized Brillouin Zone: Efficient Method of Computing (Spin) Hall Conductances*, J. Phys. Soc. Japan **74**, 1674 (2005).

[65] A. A. Maznev, A. G. Every, and O. B. Wright, *Reciprocity in Reflection and Transmission: What Is a 'Phonon Diode'?*, Wave Motion **50**, 776 (2013).

[66] C. Brendel, V. Peano, O. J. Painter, and F. Marquardt, *Pseudomagnetic Fields for Sound at the Nanoscale*, Proc. Natl. Acad. Sci. **114**, E3390 (2017).

[67] M. Miniaci, R. K. Pal, B. Morvan, and M. Ruzzene, *Experimental Observation of Topologically Protected Helical Edge Modes in Patterned Elastic Plates*, Phys. Rev. X **8**, 031074 (2018).

[68] Z. Zhang, Y. Tian, Y. Wang, S. Gao, Y. Cheng, X. Liu, and J. Christensen, *Directional Acoustic Antennas Based on Valley-Hall Topological Insulators*, Adv. Mater. **30**, 1 (2018).

[69] B. Orazbayev and R. Fleury, *Quantitative Robustness Analysis of Topological Edge Modes in C6 and Valley-Hall Metamaterial Waveguides*, Nanophotonics **8**, 1433 (2019).

[70] S. Guenneau, A. Movchan, G. Pétursson, and S. Anantha Ramakrishna, *Acoustic Metamaterials for Sound Focusing and Confinement*, New J. Phys. **9**, 399 (2007).

[71] M. Trigo, A. Bruchhausen, A. Fainstein, B. Jusserand, and V. Thierry-Mieg, *Confinement of Acoustical Vibrations in a Semiconductor Planar Phonon Cavity*, Phys. Rev. Lett. **89**, (2002).

[72] D. Leykam and S. Flach, *Perspective: Photonic Flatbands*, APL Photonics **3**, 070901 (2018).

[73] X. Hu, C. T. Chan, and J. Zi, *Two-Dimensional Sonic Crystals with Helmholtz Resonators*, Phys. Rev. E **71**, 055601 (2005).

[74] A. Khelif, P. A. Deymier, B. Djafari-Rouhani, J. O. Vasseur, and L. Dobrzynski, *Two-Dimensional Phononic Crystal with Tunable Narrow Pass Band: Application to a Waveguide with Selective Frequency*, J. Appl. Phys. **94**, 1308 (2003).

[75] J.-B. Li, Y. Wang, and C. Zhang, *Tuning of Acoustic Bandgaps in Phononic Crystals With Helmholtz Resonators*, J. Vib. Acoust. **135**, 031015 (2013).

[76] Z. G. Wang, S. H. Lee, C. K. Kim, C. M. Park, K. Nahm, and S. A. Nikitov, *Acoustic Wave Propagation in One-Dimensional Phononic Crystals Containing Helmholtz Resonators*, J. Appl. Phys. **103**, 064907 (2008).

[77] X. Wang and C.-M. Mak, *Wave Propagation in a Duct with a Periodic Helmholtz Resonators Array*, J. Acoust. Soc. Am. **131**, 1172 (2012).

[78] D. Zhao, M. Xiao, C. W. Ling, C. T. Chan, and K. H. Fung, *Topological Interface Modes in Local Resonant Acoustic Systems*, Phys. Rev. B **98**, 014110 (2018).

[79] T. Lee and H. Iizuka, *Bragg Scattering Based Acoustic Topological Transition Controlled by Local Resonance*, Phys. Rev. B **99**, 064305 (2019).

[80] S. Yves, R. Fleury, F. Lemoult, M. Fink, and G. Lerosey, *Topological Acoustic Polaritons: Robust Sound Manipulation at the Subwavelength Scale*, New J. Phys. **19**, 075003 (2017).

[81] H. Jiang, M. Chen, Y. Liu, T. Yang, W. Xu, Y. Liu, M. Zhang, and Y. Wang, *Acoustic Valley Edge States in a Graphene-like System with Sub-Wavelength Resonator*, J. Acoust. Soc. Am. **146**, 736 (2019).

[82] L. Y. Zheng, V. Achilleos, Z. G. Chen, O. Richoux, G. Theocharis, Y. Wu, J. Mei, S. Felix, V. Tournat, and V. Pagneux, *Acoustic Graphene Network Loaded with Helmholtz Resonators: A First-Principle Modeling, Dirac Cones, Edge and Interface Waves*, New J. Phys. **22**, (2020).

[83] S. Yves, R. Fleury, T. Berthelot, M. Fink, F. Lemoult, and G. Lerosey, *Crystalline Metamaterials for Topological Properties at Subwavelength Scales*, Nat. Commun.

8, 16023 (2017).

[84] R. Al Jahdali and Y. Wu, *Coupled Resonators for Sound Trapping and Absorption*, Sci. Rep. **8**, 13855 (2018).

[85] N. Kaina, F. Lemoult, M. Fink, and G. Lerosey, *Negative Refractive Index and Acoustic Superlens from Multiple Scattering in Single Negative Metamaterials*, Nature **525**, 77 (2015).

[86] C.-L. Ding and X.-P. Zhao, *Multi-Band and Broadband Acoustic Metamaterial with Resonant Structures*, J. Phys. D. Appl. Phys. **44**, 215402 (2011).

[87] C. Ding, Y. Dong, K. Song, S. Zhai, Y. Wang, and X. Zhao, *Mutual Inductance and Coupling Effects in Acoustic Resonant Unit Cells*, Materials (Basel). **12**, 1558 (2019).

[88] R. L. Panton and J. M. Miller, *Resonant Frequencies of Cylindrical Helmholtz Resonators*, J. Acoust. Soc. Am. **57**, 1533 (1975).

[89] R. C. Chanaud, *Effects Of Geometry On The Resonance Frequency Of Helmholtz Resonators*, J. Sound Vib. **178**, 337 (1994).

[90] B. Orazbayev, N. Kaina, and R. Fleury, *Chiral Waveguides for Robust Waveguiding at the Deep Subwavelength Scale*, Phys. Rev. Appl. **10**, 054069 (2018).

[91] D. Vanderbilt, *Berry Phases in Electronic Structure Theory* (Cambridge University Press, 2018).

[92] S. Johnson and J. J.D., *Photonic Crystals: The Road from Theory to Practice* (Kluwer Academic, Boston, 2002).

[93] M. R. Stinson, *The Propagation of Plane Sound Waves in Narrow and Wide Circular Tubes, and Generalization to Uniform Tubes of Arbitrary Cross-sectional Shape*, J. Acoust. Soc. Am. **89**, 550 (1991).

[94] H. Tijdeman, *On the Propagation of Sound Waves in Cylindrical Tubes*, J. Sound Vib. **39**, 1 (1975).

[95] N. Jiménez, W. Huang, V. Romero-García, V. Pagneux, and J.-P. Groby, *Ultra-Thin Metamaterial for Perfect and Quasi-Omnidirectional Sound Absorption*, Appl. Phys. Lett. **109**, 121902 (2016).

[96] J. Friend and L. Y. Yeo, *Microscale Acoustofluidics: Microfluidics Driven via Acoustics and Ultrasonics*, Rev. Mod. Phys. **83**, 647 (2011).

[97] N. Zhang, A. Horesh, O. Manor, and J. Friend, *Powerful Acoustogeometric*

Streaming from Dynamic Geometric Nonlinearity, Phys. Rev. Lett. **126**, 164502 (2021).

[98] N. Zhang, A. Horesh, and J. Friend, *Manipulation and Mixing of 200 Femtoliter Droplets in Nanofluidic Channels Using MHz-Order Surface Acoustic Waves*, Adv. Sci. **8**, 1 (2021).

[99] W. Connacher, J. Orosco, and J. Friend, *Droplet Ejection at Controlled Angles via Acoustofluidic Jetting*, Phys. Rev. Lett. **125**, 184504 (2020).

[100] R. H. Liu, J. Yang, M. Z. Pindera, M. Athavale, and P. Grodzinski, *Bubble-Induced Acoustic Micromixing*, Lab Chip **2**, 151 (2002).

[101] Y. Zhang, C. Devendran, C. Lupton, A. De Marco, and A. Neild, *Versatile Platform for Performing Protocols on a Chip Utilizing Surface Acoustic Wave (SAW) Driven Mixing*, Lab Chip **19**, 262 (2019).

[102] Y. Gu, C. Chen, Z. Mao, H. Bachman, R. Becker, J. Rufo, Z. Wang, P. Zhang, J. Mai, S. Yang, J. Zhang, S. Zhao, Y. Ouyang, D. T. W. Wong, Y. Sadovsky, and T. J. Huang, *Acoustofluidic Centrifuge for Nanoparticle Enrichment and Separation*, Sci. Adv. **7**, 1 (2021).

[103] A. Ozcelik, J. Rufo, F. Guo, Y. Gu, P. Li, J. Lata, and T. J. Huang, *Acoustic Tweezers for the Life Sciences*, Nat. Methods **15**, 1021 (2018).

[104] B. Kang, J. Shin, H. J. Park, C. Rhyou, D. Kang, S. J. Lee, Y. sup Yoon, S. W. Cho, and H. Lee, *High-Resolution Acoustophoretic 3D Cell Patterning to Construct Functional Collateral Cylindroids for Ischemia Therapy*, Nat. Commun. **9**, (2018).

[105] J. P. Lata, F. Guo, J. Guo, P. H. Huang, J. Yang, and T. J. Huang, *Surface Acoustic Waves Grant Superior Spatial Control of Cells Embedded in Hydrogel Fibers*, Adv. Mater. **28**, 8632 (2016).

[106] K. J. Satzinger, Y. P. Zhong, H.-S. Chang, G. A. Peairs, A. Bienfait, M.-H. Chou, A. Y. Cleland, C. R. Conner, É. Dumur, J. Grebel, I. Gutierrez, B. H. November, R. G. Povey, S. J. Whiteley, D. D. Awschalom, D. I. Schuster, and A. N. Cleland, *Quantum Control of Surface Acoustic-Wave Phonons*, Nature **563**, 661 (2018).

[107] Y. Chu, P. Kharel, W. H. Renninger, L. D. Burkhart, L. Frunzio, P. T. Rakich, and R. J. Schoelkopf, *Quantum Acoustics with Superconducting Qubits*, Science (80-.). **358**, 199 (2017).

[108] R. Manenti, M. J. Peterer, A. Nersisyan, E. B. Magnusson, A. Patterson, and P. J. Leek, *Surface Acoustic Wave Resonators in the Quantum Regime*, Phys. Rev. B **93**, 041411 (2016).

[109] C. H. W. Barnes, J. M. Shilton, and A. M. Robinson, *Quantum Computation Using Electrons Trapped by Surface Acoustic Waves*, Phys. Rev. B **62**, 8410 (2000).

[110] S. Hermelin, S. Takada, M. Yamamoto, S. Tarucha, A. D. Wieck, L. Saminadayar, C. Bäuerle, and T. Meunier, *Electrons Surfing on a Sound Wave as a Platform for Quantum Optics with Flying Electrons*, Nature **477**, 435 (2011).

[111] R. P. G. McNeil, M. Kataoka, C. J. B. Ford, C. H. W. Barnes, D. Anderson, G. A. C. Jones, I. Farrer, and D. A. Ritchie, *On-Demand Single-Electron Transfer between Distant Quantum Dots*, Nature **477**, 439 (2011).

[112] J. MEI and J. FRIEND, *A Review: Controlling the Propagation of Surface Acoustic Waves via Waveguides for Potential Use in Acoustofluidics*, Mech. Eng. Rev. **7**, 19 (2020).

[113] A. J. Slobodnik and E. D. Conway, *The Effect of Beam Steering on the Design of Microwave Acoustic Surface Wave Devices*, in *G-MTT 1970 International Microwave Symposium*, Vol. 13 (IEEE, 1970), pp. 314–318.

[114] A. Hagelauer, G. Fattinger, C. C. W. Ruppel, M. Ueda, K. Hashimoto, and A. Tag, *Microwave Acoustic Wave Devices: Recent Advances on Architectures, Modeling, Materials, and Packaging*, IEEE Trans. Microw. Theory Tech. **66**, 4548 (2018).

[115] P. Delsing, A. N. Cleland, M. J. A. Schuetz, J. Knörzer, G. Giedke, J. I. Cirac, K. Srinivasan, M. Wu, K. C. Balram, C. Bäuerle, T. Meunier, C. J. B. Ford, P. V. Santos, E. Cerda-Méndez, H. Wang, H. J. Krenner, E. D. S. Nysten, M. Weiß, G. R. Nash, L. Thevenard, C. Gourdon, P. Rovillain, M. Marangolo, J.-Y. Duquesne, G. Fischerauer, W. Ruile, A. Reiner, B. Paschke, D. Denysenko, D. Volkmer, A. Wixforth, H. Bruus, M. Wiklund, J. Reboud, J. M. Cooper, Y. Fu, M. S. Brugger, F. Rehfeldt, and C. Westerhausen, *The 2019 Surface Acoustic Waves Roadmap*, J. Phys. D. Appl. Phys. **52**, 353001 (2019).

[116] T. Nomura, X. X. Zhang, S. Zherlitsyn, J. Wosnitza, Y. Tokura, N. Nagaosa, and S. Seki, *Phonon Magnetochiral Effect*, Phys. Rev. Lett. **122**, 145901 (2019).

[117] R. Sasaki, Y. Nii, Y. Iguchi, and Y. Onose, *Nonreciprocal Propagation of Surface Acoustic Wave in Ni/LiNbO3*, Phys. Rev. B **95**, 1 (2017).

[118] R. Verba, I. Lisenkov, I. Krivorotov, V. Tiberkevich, and A. Slavin, *Nonreciprocal Surface Acoustic Waves in Multilayers with Magnetoelastic and Interfacial Dzyaloshinskii-Moriya Interactions*, Phys. Rev. Appl. **9**, 64014 (2018).

[119] B. Liang, B. Yuan, and J. C. Cheng, *Acoustic Diode: Rectification of Acoustic Energy Flux in One-Dimensional Systems*, Phys. Rev. Lett. **103**, 1 (2009).

[120] B. Liang, X. S. Guo, J. Tu, D. Zhang, and J. C. Cheng, *An Acoustic Rectifier*, Nat.

Mater. **9**, 989 (2010).

[121] N. Boechler, G. Theocharis, and C. Daraio, *Bifurcation-Based Acoustic Switching and Rectification*, Nat. Mater. **10**, 665 (2011).

[122] L. Shao, W. Mao, S. Maity, N. Sinclair, Y. Hu, L. Yang, and M. Lončar, *Non-Reciprocal Transmission of Microwave Acoustic Waves in Nonlinear Parity–Time Symmetric Resonators*, Nat. Electron. **3**, 267 (2020).

[123] L. Lu, J. D. Joannopoulos, and M. Soljačić, *Topological Photonics*, Nat. Photonics **8**, 821 (2014).

[124] F. D. M. Haldane and S. Raghu, *Possible Realization of Directional Optical Waveguides in Photonic Crystals with Broken Time-Reversal Symmetry*, Phys. Rev. Lett. **100**, 013904 (2008).

[125] S. Raghu and F. D. M. Haldane, *Analogs of Quantum-Hall-Effect Edge States in Photonic Crystals*, Phys. Rev. A **78**, 033834 (2008).

[126] B. Bahari, L. Hsu, S. H. Pan, D. Preece, A. Ndao, A. El Amili, Y. Fainman, and B. Kanté, *Photonic Quantum Hall Effect and Multiplexed Light Sources of Large Orbital Angular Momenta*, Nat. Phys. 4 (2021).

[127] S. D. Huber, *Topological Mechanics*, Nat. Phys. **12**, 621 (2016).

[128] Y. Ding, Y. Peng, Y. Zhu, X. Fan, J. Yang, B. Liang, X. Zhu, X. Wan, and J. Cheng, *Experimental Demonstration of Acoustic Chern Insulators*, Phys. Rev. Lett. **122**, 014302 (2019).

[129] P. Wang, L. Lu, and K. Bertoldi, *Topological Phononic Crystals with One-Way Elastic Edge Waves*, Phys. Rev. Lett. **115**, 104302 (2015).

[130] R. Fleury, D. L. Sounas, C. F. Sieck, M. R. Haberman, and A. Alu, *Sound Isolation and Giant Linear Nonreciprocity in a Compact Acoustic Circulator*, Science (80-.). **343**, 516 (2014).

[131] D. J. Bisharat and D. F. Sievenpiper, *Electromagnetic-Dual Metasurfaces for Topological States along a 1D Interface*, Laser Photonics Rev. **13**, 1 (2019).

[132] C. L. Kane and E. J. Mele, *Z2 Topological Order and the Quantum Spin Hall Effect*, Phys. Rev. Lett. **95**, 3 (2005).

[133] Z. Tian, C. Shen, J. Li, E. Reit, H. Bachman, J. E. S. Socolar, S. A. Cummer, and T. Jun Huang, *Dispersion Tuning and Route Reconfiguration of Acoustic Waves in Valley Topological Phononic Crystals*, Nat. Commun. **11**, 762 (2020).

[134] J. Cha, K. W. Kim, and C. Daraio, *Experimental Realization of On-Chip Topological*

Nanoelectromechanical Metamaterials, Nature **564**, 229 (2018).

[135] J. Ma, X. Xi, and X. Sun, *Experimental Demonstration of Dual-Band Nano-Electromechanical Valley-Hall Topological Metamaterials*, Adv. Mater. **33**, 1 (2021).

[136] S.-Y. Yu, X.-C. Sun, X. Ni, Q. Wang, X.-J. Yan, C. He, X.-P. Liu, L. Feng, M.-H. Lu, and Y.-F. Chen, *Surface Phononic Graphene*, Nat. Mater. **15**, 1243 (2016).

[137] Z. Wang, F.-K. Liu, S.-Y. Yu, S.-L. Yan, M.-H. Lu, Y. Jing, and Y.-F. Chen, *Guiding Robust Valley-Dependent Edge States by Surface Acoustic Waves*, J. Appl. Phys. **125**, 044502 (2019).

[138] X.-T. He, E.-T. Liang, J.-J. Yuan, H.-Y. Qiu, X.-D. Chen, F.-L. Zhao, and J.-W. Dong, *A Silicon-on-Insulator Slab for Topological Valley Transport*, Nat. Commun. **10**, 872 (2019).

[139] F. Liu and K. Wakabayashi, *Novel Topological Phase with a Zero Berry Curvature*, Phys. Rev. Lett. **118**, 076803 (2017).

[140] H.-X. Wang, L. Liang, B. Jiang, J. Hu, X. Lu, and J.-H. Jiang, *Higher-Order Topological Phases in Tunable C 3 Symmetric Photonic Crystals* , Photonics Res. **9**, 1854 (2021).

[141] N. Zhang, J. Mei, T. Gopesh, and J. Friend, *Optimized, Omnidirectional Surface Acoustic Wave Source: 152° Y-Rotated Cut of Lithium Niobate for Acoustofluidics*, IEEE Trans. Ultrason. Ferroelectr. Freq. Control **67**, 2176 (2020).

[142] T. Inui, J. Mei, C. Imashiro, Y. Kurashina, J. Friend, and K. Takemura, *Focused Surface Acoustic Wave Locally Removes Cells from Culture Surface*, Lab Chip **21**, 1299 (2021).

[143] S. M. Langelier, L. Y. Yeo, and J. Friend, *UV Epoxy Bonding for Enhanced SAW Transmission and Microscale Acoustofluidic Integration*, Lab Chip **12**, 2970 (2012).

[144] J. Mei, N. Zhang, and J. Friend, *Fabrication of Surface Acoustic Wave Devices on Lithium Niobate*, J. Vis. Exp. **2020**, 1 (2020).

[145] W. Connacher, N. Zhang, A. Huang, J. Mei, S. Zhang, T. Gopesh, and J. Friend, *Micro/Nano Acoustofluidics: Materials, Phenomena, Design, Devices, and Applications*, Lab Chip **18**, 1952 (2018).

[146] J. LUO, *Young's Modulus of Electroplated Ni Thin Film for MEMS Applications*, Mater. Lett. **58**, 2306 (2004).

[147] F. D. M. Haldane, *Berry Curvature on the Fermi Surface: Anomalous Hall Effect as*

a Topological Fermi-Liquid Property, Phys. Rev. Lett. **93**, 1 (2004).

[148] T. Li, P. Zhu, W. A. Benalcazar, and T. L. Hughes, *Fractional Disclination Charge in Two-Dimensional Cn -Symmetric Topological Crystalline Insulators*, Phys. Rev. B **101**, 115115 (2020).

[149] R. Queiroz, I. C. Fulga, N. Avraham, H. Beidenkopf, and J. Cano, *Partial Lattice Defects in Higher-Order Topological Insulators*, Phys. Rev. Lett. **123**, 266802 (2019).

[150] M. Xiao, W. J. Chen, W. Y. He, and C. T. Chan, *Synthetic Gauge Flux and Weyl Points in Acoustic Systems*, Nat. Phys. **11**, 920 (2015).

[151] H. Ge, X. Ni, Y. Tian, S. K. Gupta, M. H. Lu, X. Lin, W. D. Huang, C. T. Chan, and Y. F. Chen, *Experimental Observation of Acoustic Weyl Points and Topological Surface States*, Phys. Rev. Appl. **10**, 1 (2018).

[152] H. He, C. Qiu, L. Ye, X. Cai, X. Fan, M. Ke, F. Zhang, and Z. Liu, *Topological Negative Refraction of Surface Acoustic Waves in a Weyl Phononic Crystal*, Nature **560**, 61 (2018).

[153] V. Peri, M. Serra-Garcia, R. Ilan, and S. D. Huber, *Axial-Field-Induced Chiral Channels in an Acoustic Weyl System*, Nat. Phys. **15**, 357 (2019).

[154] H. He, C. Qiu, X. Cai, M. Xiao, M. Ke, F. Zhang, and Z. Liu, *Observation of Quadratic Weyl Points and Double-Helicoid Arcs*, Nat. Commun. **11**, 1 (2020).

[155] H. Xue, Y. Yang, G. Liu, F. Gao, Y. Chong, and B. Zhang, *Realization of an Acoustic Third-Order Topological Insulator*, Phys. Rev. Lett. **122**, 244301 (2019).

[156] F. Schindler, Z. Wang, M. G. Vergniory, A. M. Cook, A. Murani, S. Sengupta, A. Y. Kasumov, R. Deblock, S. Jeon, I. Drozdov, H. Bouchiat, S. Guéron, A. Yazdani, B. A. Bernevig, and T. Neupert, *Higher-Order Topology in Bismuth*, Nat. Phys. **14**, 918 (2018).

[157] L. Lu, H. Gao, and Z. Wang, *Topological One-Way Fiber of Second Chern Number*, Nat. Commun. **9**, 1 (2018).

[158] Q. Lin, X. Q. Sun, M. Xiao, S. C. Zhang, and S. Fan, *A Three-Dimensional Photonic Topological Insulator Using a Two-Dimensional Ring Resonator Lattice with a Synthetic Frequency Dimension*, Sci. Adv. **4**, 1 (2018).

[159] E. Lustig, L. Maczewsky, T. Biesenthal, Z. Yang, Y. Plotnik, A. Szameit, and M. Segev, *Experimentally Realizing Photonic Topological Edge States in 3D*, Opt. InfoBase Conf. Pap. **Part F182-**, 3 (2020).

[160] C.-K. Chiu, J. C. Y. Teo, A. P. Schnyder, and S. Ryu, *Classification of Topological Quantum Matter with Symmetries*, Rev. Mod. Phys. **88**, 035005 (2016).

[161] J. C. Y. Teo and C. L. Kane, *Topological Defects and Gapless Modes in Insulators and Superconductors*, Phys. Rev. B **82**, 115120 (2010).

[162] Y. Ando and L. Fu, *Topological Crystalline Insulators and Topological Superconductors: From Concepts to Materials*, Annu. Rev. Condens. Matter Phys. **6**, 361 (2015).